October 2023
Research Report: UCPRC-RR-2023-01

Drying Shrinkage Response of Full-Scale Thin Concrete Overlay on Asphalt Sections

Authors:
Angel Mateos, John Harvey, Fabian Paniagua, Julio Paniagua, and Rongzong Wu

Partnered Pavement Research Center (PPRC) Strategic Plan Element (SPE) 4.83 (DRISI Task 3768): Concrete Coefficient of Thermal Expansion Moisture Dependency and Tensile Creep

PREPARED FOR:

California Department of Transportation
Division of Research, Innovation, and System Information
Office of Materials and Infrastructure

PREPARED BY:

University of California
Pavement Research Center
UC Davis, UC Berkeley

TECHNICAL REPORT DOCUMENTATION PAGE

1. REPORT NUMBER UCPRC-RR-2023-01	2. GOVERNMENT ASSOCIATION NUMBER	3. RECIPIENT'S CATALOG NUMBER
4. TITLE AND SUBTITLE Drying Shrinkage Response of Full-Scale Thin Concrete Overlay on Asphalt Sections		5. REPORT PUBLICATION DATE October 2023
		6. PERFORMING ORGANIZATION CODE
7. AUTHOR(S) Angel Mateos (ORCID 0000-0002-3614-2858) John Harvey (ORCID 0000-0002-8924-6212) Fabian Paniagua (ORCID 0000-0002-2385-4899) Julio Paniagua (ORCID 0000-0003-4062-5454) Rongzong Wu (ORCID 0000-0001-7364-7583)		8. PERFORMING ORGANIZATION REPORT NO. UCPRC-RR-2023-01 UCD-ITS-RR-23-71
9. PERFORMING ORGANIZATION NAME AND ADDRESS University of California Pavement Research Center Department of Civil and Environmental Engineering, UC Davis 1 Shields Avenue Davis, CA 95616		10. WORK UNIT NUMBER
		11. CONTRACT OR GRANT NUMBER
12. SPONSORING AGENCY AND ADDRESS California Department of Transportation Division of Research, Innovation, and System Information P.O. Box 942873 Sacramento, CA 94273-0001		13. TYPE OF REPORT AND PERIOD COVERED Research Report September 2020 to September 2021
		14. SPONSORING AGENCY CODE 3768

15. SUPPLEMENTAL NOTES
doi:10.7922/G2FQ9TZG

16. ABSTRACT

Moisture-related shrinkage is regarded as one of the phenomena that has the largest impacts on the performance of jointed plain concrete pavements. Still, most mechanistic-empirical design methods oversimplify or ignore predictions of moisture-related shrinkage and its effects on concrete pavements. This study evaluates how moisture-related shrinkage accumulates in concrete pavements and the structural response of the concrete pavement slabs to the shrinkage action. The experimental data come from six thin concrete overlay of asphalt pavements that were instrumented with sensors to measure the structural and hygrothermal response of the slabs due to temperature and moisture-related actions. After an analysis of the predictions made by current shrinkage models, a new shrinkage model was developed. This new model, which is based on the incremental-recursive application of the B4 shrinkage model, provided an excellent prediction of the moisture-related shrinkage measured in the field. In addition, the structural response of the concrete pavement slabs under the moisture-related shrinkage action was analyzed using the finite element method (FEM). The FEM analysis based on the standard practice for concrete pavement mechanistic-empirical modeling resulted in unrealistically high tensile stresses. However, much smaller stress values were found when the time-dependent (viscoelastic) behavior of concrete and asphalt was considered.

17. KEY WORDS	18. DISTRIBUTION STATEMENT
rigid pavement, bonded concrete overlay of asphalt (BCOA), thin whitetopping, early high-strength concrete, coefficient of thermal expansion, moisture-related shrinkage, relative humidity	No restrictions. This document is available to the public through the National Technical Information Service, Springfield, VA 22161

19. SECURITY CLASSIFICATION (of this report)	20. NUMBER OF PAGES	21. PRICE
Unclassified	109	None

UCPRC ADDITIONAL INFORMATION

1. DRAFT STAGE Final	2. VERSION NUMBER 1
3. PARTNERED PAVEMENT RESEARCH CENTER STRATEGIC PLAN ELEMENT NUMBER 4.83	4. DRISI TASK NUMBER 3768
5. CALTRANS TECHNICAL LEAD AND REVIEWER(S) David Lim	6. FHWA NUMBER CA233768

7. PROPOSALS FOR IMPLEMENTATION

The use of 6x6 ft. slabs rather than full-lane width slabs (12×12 ft.) is recommended for use with concrete overlays on asphalt pavement where the concrete overlays are 7 in. and thinner to reduce shrinkage-related stresses.

8. RELATED DOCUMENTS

Mateos, A., Harvey, T.J., Paniagua, F., Paniagua, J., and Wu, R. 2018. *Development of Improved Guidelines and Designs for Thin Whitetopping: Construction and Initial Environmental Response of Full-Scale BCOA Sections* (Research Report: UCPRC-RR-2017-02). Davis and Berkeley, CA: University of California Pavement Research Center.

Mateos, A., Harvey, J.T., Wu, R., Paniagua, F., and Paniagua, J. 2020. *Development of Improved Guidelines and Designs for Thin Whitetopping: Environmental Response of Full-Scale BCOA Sections* (Research Report: UCPRC-RR-2017-03). Davis and Berkeley, CA: University of California Pavement Research Center.

Mateos, A., Harvey, T.J., Paniagua, F., Paniagua, J., and Wu, R. 2019. *Development of Improved Guidelines and Designs for Thin Whitetopping: Summary, Conclusions, and Recommendations* (Summary Report: UCPRC-SR-2018-01). Davis and Berkeley, CA: University of California Pavement Research Center.

9. LABORATORY ACCREDITATION

The UCPRC laboratory is accredited by AASHTO resource and CCRL for the laboratory testing discussed in this report.

10. SIGNATURES

A. Mateos **FIRST AUTHOR**	J.T. Harvey **TECHNICAL REVIEW**	C. Fink **EDITOR**	J.T. Harvey **PRINCIPAL INVESTIGATOR**	D. Lim **CALTRANS TECH. LEADS**	T.J. Holland **CALTRANS CONTRACT MANAGER**

PROJECT OBJECTIVES

The objective of Partnered Pavement Research Center (PPRC) Project 4.83 is to develop a test to measure concrete CTE-moisture dependency and a framework for modeling CTE evolution in the field and the structural response of concrete pavements under thermal and moisture-related shrinkage actions, including concrete tensile creep/relaxation capacity. The research presented in this report focuses on modeling the structural response of concrete pavements under the moisture-related shrinkage action.

The research is based on the moisture-related response of six full-scale thin concrete overlay on asphalt (COA) sections that were built and monitored within the framework of PPRC Project 4.58B (2014-2017). The primary goal of that project was to develop recommendations and guidance on the use of thin COA as a rehabilitation alternative in California. Thin COA, formerly known as thin whitetopping, is a type of rehabilitation consisting of a 100 to 175 mm (0.33 to 0.58 ft.) thick portland cement concrete overlay on an existing flexible or composite pavement. This research was conducted to answer to answer the following questions:

- What moisture-related shrinkage takes place in the COA slabs?
- Do shrinkage prediction models work for rapid-strength concrete mixes?
- What is the relationship between laboratory and field shrinkage?
- What is the stress due to moisture-related shrinkage?
    - What is the role of asphalt viscoelasticity?
    - What is the role of concrete creep?
    - What is the role of concrete surface microcracking?
    - Are there any other stress relaxation mechanisms?

EXECUTIVE SUMMARY

Moisture-related shrinkage is regarded as one of the phenomena that have the largest impacts on the performance of jointed plain concrete pavements. Despite that, most mechanistic-empirical design methods oversimplify or ignore predictions of moisture-related shrinkage and its effects on concrete pavements. The objective of the research presented in this report is to evaluate how moisture-related shrinkage accumulates in concrete pavements and the structural response of the concrete overlay of asphalt (COA) slabs to the shrinkage action. This research addressed the following main questions:

- What moisture-related shrinkage takes place in the COA slabs?
- Do shrinkage prediction models work for rapid-strength concrete mixes?
- What is the relationship between laboratory and field shrinkage?
- What is the stress due to moisture-related shrinkage?

The research presented in this report is based on the structural and hygrothermal response of six COA sections that were built in February 2016 and monitored for 15 months. Those sections—referred to as "ENV sections"—were part of a larger experiment whose primary goal was to develop recommendations and guidance on the use of thin COA as a rehabilitation alternative in California.

The set of ENV sections is the result of a partial factorial design with three factors: concrete mix, concrete curing procedure, and slab size. The levels of each of these three factors are shown below:

- Concrete mix (each type of concrete has been assigned a shorthand name that is used to refer to it in this report):
    - P2: 10-hour design opening time (OT) with Type II/V portland cement and a 0.33 water/cement (w/c) ratio
    - P2-ICC: Internally cured concrete based on the P2 mix (50% sand replacement with prewetted lightweight aggregates)
    - P3: Four-hour design OT with Type III portland cement and a 0.31 w/c ratio
    - CSA: Four-hour design OT with calcium sulfoaluminate (CSA) cement and a 0.42 w/c ratio

    Note: the Caltrans flexural strength requirement for opening time of rapid-strength concrete is 2.8 MPa (400 psi).
- Concrete curing procedures:
    - Curing compound
    - Shrinkage-reducing admixture (topical use) applied before the curing compound
- Slab size (in this report, each slab size has been assigned a shorthand name that is used to refer to it):
    - 6×6: Half-lane width, 1.8×1.8 m (approximately 6×6 ft.) slabs
    - 12×12: Full-lane width, 3.6×3.6 m (approximately 12×12 ft.) slabs

The six ENV sections were instrumented to measure the response of the concrete slabs to the ambient environment and the cement hydration. The instrumentation whose data have been analyzed in this report include: (1) vibrating wire strain gauges (VWSGs) that measured concrete horizontal strain, (2) joint displacement measuring devices that measured slabs horizontal and vertical movements, (3) thermocouples embedded in the concrete at several depths, (4) relative humidity (RH) sensors embedded in the concrete, and (5) moisture content sensors embedded in the concrete. In addition to the six ENV sections, eight unrestrained shrinkage prisms were prepared in February 2016, and they were left outdoors with all surfaces uncovered near the ENV sections so they would be subjected to the same environmental conditions. Each of those prisms was instrumented with a VWSG to measure strain along its longest direction. Environmental conditions were measured by means of a weather station located nearby the sections.

The data collected with the VWSGs were analyzed with incremental models that included two components, one that accounted for moisture-related shrinkage at constant temperature and another that accounted for thermal deformations. The parameters of the models were backcalculated by fitting measured strains with the model's predictions. For the purposes of this report, the backcalculated parameters for the unrestrained shrinkage prisms were the daily values of the moisture-related shrinkage (the figure below shows the evolution of moisture-related shrinkage in the unrestrained shrinkage prisms for four and a half months following construction). In the same way, the backcalculated parameters for the COA slabs were the daily values of the *mean moisture-related shrinkage*, ε_{MEAN}, defined in this report as the average of the strains at the top and bottom of the slabs, and the daily values of the *differential drying shrinkage*, ε_{DIFF}, defined in this report as the difference between the strains at the top and bottom of the slab. In the backcalculation process, the evolution of mean and differential shrinkage versus time were determined by assuming that both mean and differential shrinkage change linearly within a day, but change from one day to the next.

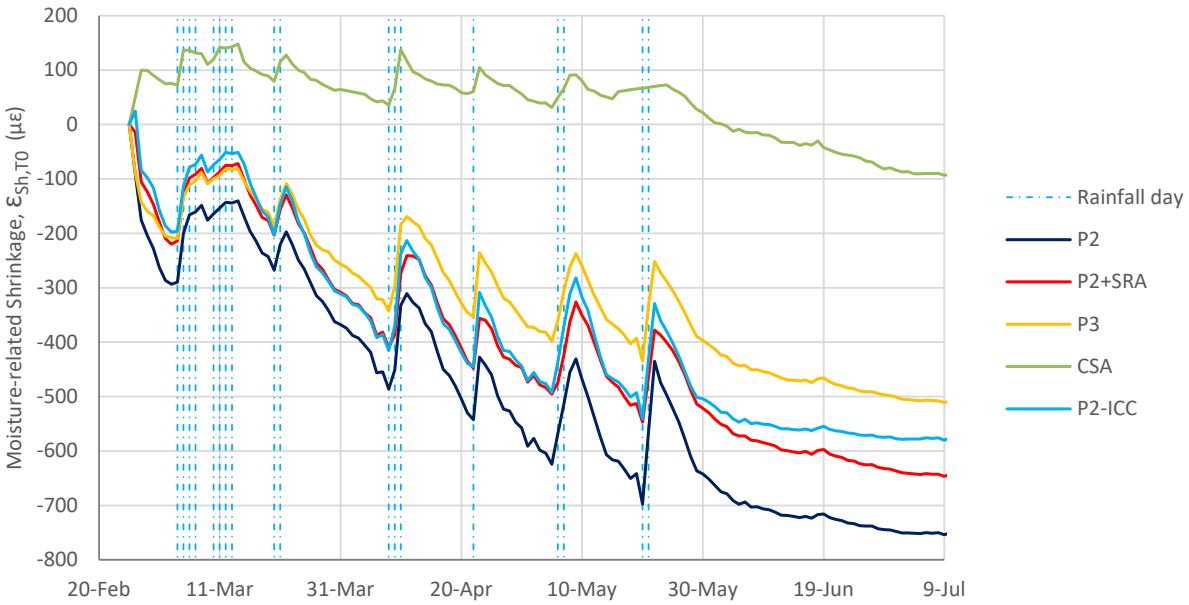

Moisture-related shrinkage backcalculated for the unrestrained shrinkage prisms.

The following conclusions of this research have been grouped to address the four main questions this research intended to answer.

What moisture-related shrinkage takes place in the COA slabs?

- Very high levels of differential shrinkage were backcalculated in all the sections with portland cement mixes treated with curing compound, with values as high as 450 to 550 με, depending on the mix.
- Around 200 to 250 με of autogenous shrinkage were backcalculated in the mixes with Type II/V (P2) and Type III (P3) portland cement and water/cement ratios of 0.33 and 0.31, respectively. No autogenous shrinkage was measured in the internally cured mix (P2-ICC) or in the mix with CSA cement.
- The total moisture-related shrinkage values at the top of the COA slabs with portland cement mixes treated with curing compound reached as high as 600 to 750 με, depending on the mix.
- Rainfall events produced an almost immediate decrease in the magnitude of the differential drying shrinkage in the COA slabs, except when the concrete was already saturated. The immediacy of the response to rainfall occurred with both the portland cement and CSA mixes.
- The evolution of mean and differential shrinkage in the COA slabs showed that drying occurred in the bottom half of the slabs during summer. This conclusion is supported by moisture content measurements near the middle of the slabs at 50 mm (2 in.) depth in the concrete. The slabs were 115 mm (4.5 in.) thick.

Do shrinkage prediction models work for rapid-strength concrete (RSC) mixes?

Shrinkage was measured in the laboratory following ASTM C157, at 50% constant air RH. Predictions made by the B3, B4, and ACI 209R-92 shrinkage models were compared with shrinkage data measured in the laboratory.

- The B3 and B4 models underestimated laboratory shrinkage considerably in the mixes with Type II/V (P2) and Type III (P3) portland cement.
- The B4 model did not improve on the predictions of the B3 model, even though the B4 model is more recent, and it is applicable to concrete mixes with admixtures, such as P2 and P3. The B4 model predictions were particularly inaccurate as far as autogenous shrinkage was concerned.
- Overall, the shrinkage predictions made by the ACI 209R-92 model were not far off from the shrinkage measured in the laboratory, even though this model was not developed for mixes with admixtures.
- None of B3, B4, and ACI 209R-92 shrinkage prediction models are applicable to mixes with CSA cement or to internally cured mix (P2-ICC).

What is the relationship between laboratory and field shrinkage?

The parameters of the B4 model were backcalculated for each of the mixes based on lab shrinkage data (instead of using model equations). Then, a new prediction model was formulated based on the B4 lab-calibrated model, the *CalME* time-hardening incremental-recursive approach, and a simplified procedure to account for shrinkage reversals due to relatively high air RH. The new model, referred to as "B4-IR" (B4 incremental-recursive), was used to predict shrinkage in the field.

- The B4-IR model's predictions almost exactly reproduced the moisture-related shrinkage measured in a set of outdoor unrestrained shrinkage prisms with portland cement (mixes P2, P3, and P2-ICC).
- The B4-IR model's predictions almost exactly reproduced the differential shrinkage measured in the COA slabs with portland cement (mixes P2, P3, and P2-ICC). Although, in this case, a slight modification of the B4 parameters was required.
- The B4-IR model failed to reproduce the shrinkage measured in the outdoor unrestrained shrinkage prisms made with CSA cement and in the COA slabs made with the same material.
- The good agreement between the B4-IR model's predictions and measured shrinkage—for the mixes with portland cement—indicates that a direct link between lab and field shrinkage can be established as soon as several factors are taken into account: (1) the age difference between the concrete in the lab and the concrete in the field when drying begins, (2) the shape and volume/surface ratio differences between the lab specimens and the field slabs/concrete members, (3) the constant temperature and air RH in the lab versus the variable conditions in the field, and (4) the monotonic drying in the lab versus the alternating drying/wetting periods in the field, due to rainfall events and changing air RH.

- In B4-IR model, the unrestrained shrinkage profile in the slabs was assumed to be constant at the surface while the depth of shrinkage penetration was assumed to change as the slab concrete dried. The B4-IR model failed to reproduce the shrinkage measured in the COA slabs when the *AASHTOWare Pavement ME Design* unrestrained shrinkage profile assumption was followed (depth of drying is constant while the unrestrained shrinkage at the slab top is the one that changes as the slab concrete dries).
- Shrinkage reversals due to rainfall events were not modeled in this study. This topic should be investigated in the future since experimental data show shrinkage in the concrete slabs cannot be predicted based on air RH exclusively.

What is the stress due to moisture-related shrinkage?

The structural response of the COA slabs to the shrinkage action was modeled with the *Abaqus FEM* software. Different modeling scenarios were considered. In two of these scenarios, the current standard practice for concrete pavement mechanistic-empirical design was followed. In that standard practice, the creep/relaxation capacity of concrete and asphalt are ignored. In the rest of the modeling scenarios, the creep/relaxation capacity of either asphalt, or concrete and asphalt, were accounted for.

- The FEM modeling following the standard mechanistic-empirical design practice for concrete pavements resulted in very high and unrealistic tensile stresses at the top of the slabs.
- The FEM model resulted in much smaller stresses at the top of the slabs when the creep/relaxation capacity of concrete and asphalt were accounted for. In particular, the stresses were compatible with the microcracking observed in one of the 12×12 sections and with the lack of microcracking in the 6×6 sections.
- Asphalt creep/relaxation reduced the stresses created by the linear component of moisture-related shrinkage. Because of this property of asphalt, the total tensile stresses were reduced by 55% in the 6×6 sections and by 40% in the 12×12 sections.
- Concrete creep/relaxation mainly reduced the stresses created by the nonlinear component of the moisture-related shrinkage.
- In addition to the creep/relaxation capacity of concrete and asphalt, surface microcracking acted as a concrete stress-release mechanism in at least one of the 12×12 sections, Section K, which included the P2-ICC mix. The surface microcracking was observed in this section approximately 15 months after construction. No discrete cracking was observed in the section, which also supported the heavy vehicle simulator testing, with loads up to 80 kN (18 kip) on a single wheel, without cracking.

TABLE OF CONTENTS

PROJECT OBJECTIVES ..... **iii**
EXECUTIVE SUMMARY ..... **iv**
LIST OF FIGURES ..... **xi**
LIST OF TABLES ..... **xiii**
LIST OF ABBREVIATIONS ..... **xv**
LIST OF TEST METHODS AND SPECIFICATIONS USED IN THE REPORT ..... **xvi**
1 INTRODUCTION **1**
1.1 Background 1
1.2 Objective 3
1.3 Research Approach 3
2 LITERATURE REVIEW **6**
2.1 Evaluation of Moisture-Related Shrinkage in the Field 6
2.2 Shrinkage Considerations in Current Concrete Pavement Mechanistic-Empirical Design Procedures 10
2.2.1 Ultimate Shrinkage 10
2.2.2 Autogenous Shrinkage 11
2.2.3 Shrinkage Profile 12
2.2.4 Shrinkage Evolution Versus Time 12
2.2.5 Concrete Creep 13
2.2.6 Shrinkage Use in Performance Models 14
2.3 Concrete Pavement Shrinkage Modeling Studies 14
2.4 Summary of Literature Review 16
3 EXPERIMENTAL DATA **18**
3.1 Concrete Overlay on Asphalt Environmental Sections 18
3.2 Instrumentation of the Concrete Overlay on Asphalt Environmental Sections 19
3.3 Instrumentation of the Unrestrained Shrinkage Prisms 24
3.4 Models for the Analysis of Strain Data 24
3.5 Laboratory Testing 28
3.5.1 Concrete Laboratory Testing 28
3.5.2 Curing of Concrete Specimens 29
3.5.3 Concrete Stiffness 29
3.5.4 Concrete Tensile Strength 30
3.5.5 Concrete Moisture-Related Shrinkage 31
3.5.6 Concrete Coefficient of Thermal Expansion 32
3.5.7 Asphalt Laboratory Testing 33
3.6 Summary of Environmental Conditions During the Experiment 35
3.7 Sign Conventions Used in This Report 37
4 QUANTIFICATION OF SHRINKAGE IN THE CONCRETE OVERLAY ON ASPHALT SLABS **38**
4.1 Preliminary Conclusions Based on Vibrating Wire Strain Gauges Data 38
4.2 Maximum Shrinkage in the Concrete Slabs 41
4.3 Depth of Drying Shrinkage in the Concrete Slabs 43
5 EVALUATION OF SHRINKAGE PREDICTION MODELS **49**
6 RELATIONSHIP BETWEEN LAB AND FIELD SHRINKAGE **51**
6.1 Overview of B4 Shrinkage Model 52
6.2 Lab Calibration of B4 Shrinkage Model 53
6.3 Field Application of B4 Shrinkage Model 55
6.3.1 Extrapolation of B4 Lab-Calibrated Parameters to Field Specimens and Slabs 55
6.3.2 Consideration of Variable Temperature and Air Relative Humidity in the Field 56
6.4 Relationship Between Lab and Field Shrinkage in the Unrestrained Shrinkage Prisms 59

6.5 Relationship Between Lab and Field Shrinkage in the Concrete on Asphalt Slabs 62
7 MODELING SLABS RESPONSE TO THE SHRINKAGE ACTION 68
7.1 Consideration of the Shrinkage Action 70
7.2 Consideration of Concrete and Asphalt Creep/Relaxation Capacity 70
7.2.1 Determination of Viscoelastic Model's Parameters in the Asphalt Mixes 71
7.2.2 Determination of Viscoelastic Model's Parameters in the Concrete Mixes 74
7.3 Finite Element Method Model 76
7.4 Modeling Results 78
8 SUMMARY, CONCLUSIONS, AND RECOMMENDATIONS 83
8.1 Summary 83
8.2 Conclusions 83
8.2.1 What Moisture-Related Shrinkage Takes Place in the Concrete Overlay on Asphalt (COA) Slabs? 83
8.2.2 Do Shrinkage Prediction Models Work for Rapid-Strength Concrete (RSC) Mixes? 84
8.2.3 What Is the Relationship Between Laboratory and Field Shrinkage? 84
8.2.4 What Is the Stress Due to Moisture-Related Shrinkage? 85
8.3 Recommendations 86
REFERENCES 87

LIST OF FIGURES

Figure 3.1: Partial factorial design behind the ENV sections. 19
Figure 3.2: Instrumentation of the ENV sections. 22
Figure 3.3: Anchoring system for vertical JDMDs. 23
Figure 3.4: Unrestrained shrinkage prisms. 24
Figure 3.5: Strain composition used to analyze VWSG data in the COA slabs. 25
Figure 3.6: Assumptions in the strain models. 27
Figure 3.7: Example of fitting with the ε_{USP} model (Prism 1, P2 mix). 28
Figure 3.8: Modulus of elasticity of the lab mixes (ASTM C469). 30
Figure 3.9: Flexural strength the lab mixes (ASTM C469). 31
Figure 3.10: Moisture-related shrinkage of the lab mixes (ASTM C157). 32
Figure 3.11: Coefficient of thermal expansion of lab mixes (AASHTO T 336). 32
Figure 3.12: Dynamic modulus of the asphalt mixes (AASHTO TP 79). 34
Figure 3.13: Black diagrams of the asphalt mixes (AASHTO TP 79). 34
Figure 3.14: Air temperature and rainfall during the analysis period. 35
Figure 3.15: Air relative humidity during the analysis period. 35
Figure 3.16: Temperature distribution over a one-year period (Feb. 26, 2016, to Feb. 26, 2017, mean all ENV sections). 36
Figure 3.17: Frequency distribution of the ELTD over a one-year period (Feb. 26, 2016, to Feb. 26, 2017, mean all ENV sections). 37
Figure 4.1: Moisture-related shrinkage in the unrestrained shrinkage prisms ($\varepsilon_{Sh,T0}$). 38
Figure 4.2: Mean moisture-related shrinkage in the COA slabs ($\varepsilon_{MEAN,Sh,T0}$). 39
Figure 4.3: Differential drying shrinkage in the COA slabs at the corners ($\varepsilon_{DIFF,Sh,T0}$). 39
Figure 4.4: Comparison between mean moisture-related shrinkage at corner and center of the slabs, Section L. 40
Figure 4.5: Moisture-related shrinkage at the top of the COA slabs (at the corners). 42
Figure 4.6: Example of the difference between unrestrained shrinkage and slab shrinkage. 43
Figure 4.7: Relative humidity measured by RHC sensors at the slab center at depth of 20 mm (0.8 in.). 44
Figure 4.8: Unrestrained drying shrinkage profile in the slabs. 45
Figure 4.9: Characteristic depth of drying (DDK). 46
Figure 4.10: Unrestrained shrinkage at the slab bottom ($\varepsilon 1$). 47
Figure 4.11: Moisture content at 50 mm (2.0 in.) depth. 48
Figure 5.1: Evaluation of shrinkage prediction models (P2 mix). 50
Figure 5.2: Evaluation of shrinkage prediction models (P3 mix). 50
Figure 6.1: Air RH correction in shrinkage prediction models (B4 model). 51
Figure 6.2: Lab-calibrated B4 shrinkage model. 54
Figure 6.3: Application of the *CalME* time-hardening approach to modeling shrinkage evolution. 57
Figure 6.4: Hypothesis for modeling concrete wetting due to air RH. 58
Figure 6.5: Evaluation of B4-IR model for the unrestrained shrinkage prisms with portland cement. 60
Figure 6.6: Evaluation of the B4-IR model for the unrestrained shrinkage prisms with CSA cement. 61
Figure 6.7: Evolution of unrestrained shrinkage profile assumed in the slabs. 62
Figure 6.8: Evaluation of the B4-IR model for the COA slabs with Type II/V portland cement. 65
Figure 7.1: Unrestrained shrinkage action used in FEM modeling. 68
Figure 7.2: Viscoelastic model used for concrete and asphalt (generalized Maxwell model). 70
Figure 7.3: Approach for determining the parameters of the asphalt viscoelastic model. 72
Figure 7.4: Fitting of experimental data with the generalized Maxwell model (dynamic shear modulus). 72
Figure 7.5: Fitting of experimental data with the generalized Maxwell model (phase angle of shear modulus). 73
Figure 7.6: Approach for determining the parameters of the concrete viscoelastic model. 75

Figure 7.7: *Abaqus* software simulation of a longitudinal creep test (mix P2). 76
Figure 7.8: *Abaqus* modeling of 6×6 COA section for Scenario 1. 77
Figure 7.9: *Abaqus* modeling of 12×12 COA section for Scenario 1. 78
Figure 7.10: Results of *Abaqus* modeling of Section L (6×6, mix P2). 79
Figure 7.11: Results of *Abaqus* modeling of Section J (12×12, mix P2). 79
Figure 7.12: Results of *Abaqus* modeling of Section K (12×12, mix P2-ICC). 80
Figure 7.13: Comparison between the slab bending ($\varepsilon_{DIFF,Sh}$) and vertical displacement of slab corners. 82

LIST OF TABLES

Table 4.1: Maximum Field Shrinkage (με) 42
Table 6.1: Lab-Calibrated Parameters of the B4 Shrinkage Model 54
Table 6.2: Extrapolation of B4 Lab Parameters to Field Conditions 56
Table 6.3: B4 Model Parameters Used in COA Slab Modeling 64
Table 7.1: Shrinkage Action at Slab Top 68

DISCLAIMER

This document is disseminated in the interest of information exchange. The contents of this report reflect the views of the authors who are responsible for the facts and accuracy of the data presented herein. The contents do not necessarily reflect the official views or policies of the State of California or the Federal Highway Administration. This publication does not constitute a standard, specification, or regulation. This report does not constitute an endorsement by the Department of any product described herein.

For individuals with sensory disabilities, this document is available in alternate formats. For information, call (916) 654-8899, TTY 711, or write to California Department of Transportation, Division of Research, Innovation and System Information, MS-83, P.O. Box 942873, Sacramento, CA 94273-0001.

ACKNOWLEDGMENTS

A number of people and institutions provided input and support for the research presented in this report. The construction of the thin concrete overlay on asphalt (COA) test sections was supported by the California concrete pavement industry, under the coordination of the Southwest Concrete Pavement Association (SWCPA). The SWCPA—and particularly Charles Stuart, executive director, and Bruce Carter, consultant—also provided continuous support for the design and execution of the full-scale experiment. The technical contribution made by Teichert Materials—particularly by Pete Conlin, Moises Caballero, and Chris Fuchs—and by CTS Cement—particularly by Vince Perez and Art Bigelow—are acknowledged and greatly appreciated. The contributions of the University of Pittsburgh, a subcontractor of this research project, is also acknowledged—in particular the valuable contributions of Julie Vandenbossche and John DeSantis. Special thanks for their valuable input are due to several experts: John Bolander (UC Davis), Tom Van Dam (NCE), and Jason Weiss (Oregon State University). The technical review by Caltrans, led by David Lim and Deepak Maskey of the Office of Concrete Pavement, and oversight by Joe Holland of the Division of Research, Innovation and System Information are appreciated. The help of the staff and students at the UCPRC with construction and testing of sections and with the laboratory testing is also acknowledged.

LIST OF ABBREVIATIONS

AASHTO	American Association of State Highway and Transportation Officials
ACI	American Concrete Institute
AMPT	Asphalt Mixture Performance Tester
COA	Concrete overlay of asphalt
CSA	Calcium sulfoaluminate
CTE	Coefficient of thermal expansion
EBITD	Equivalent built-in temperature difference
ELTD	Equivalent linear temperature difference
FEM	Finite element method
FST	Field setting time
FWD	Falling weight deflectometer
HMA	Hot mix asphalt
HVS	Heavy vehicle simulator
IR	Incremental recursive
JDMD	Joint displacement measuring device
JPCP	Jointed plain concrete pavement
LTE	Load transfer efficiency
LVDT	Linear variable displacement transducer
MC	Moisture content
MEPDG	Mechanistic-Empirical Pavement Design Guide
OT	Opening time
PPRC	Partnered Pavement Research Center
QA/QC	Quality assurance/quality control
RH	Relative humidity
RSC	Rapid-strength concrete
SRA	Shrinkage-reducing admixture
UCPRC	University of California Pavement Research Center
VWSG	Vibrating wire strain gauge

LIST OF TEST METHODS AND SPECIFICATIONS USED IN THE REPORT

ASTM C157/C157M-08 (2014)	Standard Test Method for Length Change of Hardened Hydraulic-Cement Mortar and Concrete
ASTM C192/C192M-14	Standard Practice for Making and Curing Concrete Test Specimens in the Laboratory (Historical Standard)
ASTM C469/C469M-14	Standard Test Method for Static Modulus of Elasticity and Poisson's Ratio of Concrete in Compression
AASHTO TP 79-15 (2016)	Standard Method of Test for Determining the Dynamic Modulus and Flow Number for Asphalt Mixtures Using the Asphalt Mixture Performance Tester (AMPT)

SI* (MODERN METRIC) CONVERSION FACTORS				
APPROXIMATE CONVERSIONS TO SI UNITS				
Symbol	**When You Know**	**Multiply By**	**To Find**	**Symbol**
LENGTH				
in.	inches	25.40	millimeters	mm
ft.	feet	0.3048	meters	m
yd.	yards	0.9144	meters	m
mi.	miles	1.609	kilometers	km
AREA				
in^2	square inches	645.2	square millimeters	mm^2
ft^2	square feet	0.09290	square meters	m^2
yd^2	square yards	0.8361	square meters	m^2
ac.	acres	0.4047	hectares	ha
mi^2	square miles	2.590	square kilometers	km^2
VOLUME				
fl. oz.	fluid ounces	29.57	milliliters	mL
gal.	gallons	3.785	liters	L
ft^3	cubic feet	0.02832	cubic meters	m^3
yd^3	cubic yards	0.7646	cubic meters	m^3
MASS				
oz.	ounces	28.35	grams	g
lb.	pounds	0.4536	kilograms	kg
T	short tons (2000 pounds)	0.9072	metric tons	t
TEMPERATURE (exact degrees)				
°F	Fahrenheit	(F-32)/1.8	Celsius	°C
FORCE and PRESSURE or STRESS				
lbf	pound-force	4.448	newtons	N
lbf/in^2	pound-force per square inch	6.895	kilopascals	kPa
APPROXIMATE CONVERSIONS FROM SI UNITS				
Symbol	**When You Know**	**Multiply By**	**To Find**	**Symbol**
LENGTH				
mm	millimeters	0.03937	inches	in.
m	meters	3.281	feet	ft.
m	meters	1.094	yards	yd.
km	kilometers	0.6214	miles	mi.
AREA				
mm^2	square millimeters	0.001550	square inches	in^2
m^2	square meters	10.76	square feet	ft^2
m^2	square meters	1.196	square yards	yd^2
ha	hectares	2.471	acres	ac.
km^2	square kilometers	0.3861	square miles	mi^2
VOLUME				
mL	milliliters	0.03381	fluid ounces	fl. oz.
L	liters	0.2642	gallons	gal.
m^3	cubic meters	35.31	cubic feet	ft^3
m^3	cubic meters	1.308	cubic yards	yd^3
MASS				
g	grams	0.03527	ounces	oz.
kg	kilograms	2.205	pounds	lb.
t	metric tons	1.102	short tons (2000 pounds)	T
TEMPERATURE (exact degrees)				
°C	Celsius	1.8C + 32	Fahrenheit	°F
FORCE and PRESSURE or STRESS				
N	newtons	0.2248	pound-force	lbf
kPa	kilopascals	0.1450	pound-force per square inch	lbf/in^2

*SI is the abbreviation for the International System of Units. Appropriate rounding should be made to comply with Section 4 of ASTM E380. (Revised April 2021)

1 INTRODUCTION

1.1 Background

In this report, moisture-related shrinkage is defined as the deformation that concrete undergoes due to changes in the degree of saturation and/or the surface tension of the water present within the pores of the concrete. These changes may take place in the concrete because of temperature changes, external drying (drying shrinkage), and/or self-desiccation (autogenous shrinkage). The self-desiccation is the internal desiccation that occurs in concrete mixes with a low water/cement ratio because of cement hydration water demand and the net volume reduction resulting from the cement hydration reaction.

Moisture-related shrinkage is regarded as one of the phenomena that has the largest impact on the performance of jointed plain concrete pavements (JPCP) *(1)*. This type of shrinkage can produce considerable upward slab warping and the consequent loss of support at the edges and corners of the slab. It may also produce considerable slab contraction and consequent joint opening. Because of both loss of support and joint opening, the tensile stress created at the top of the slabs by the traffic loads increases and the load transfer efficiency (LTE) across the joints decreases. LTE is critical to faulting evolution over the life of the pavement. Moisture-related shrinkage alone may result in considerable tensile stresses at the top of the concrete slabs, which is due in part to the nonlinear nature of the moisture-related shrinkage deformation (nonlinear versus depth) and the restriction to upward slab bending resulting from the weight of the slab and the slab's interaction with the underlying base. The combination of traffic and moisture-related shrinkage may be critical to corner cracking, transverse top-down cracking, and longitudinal top-down cracking. The relevance of JPCP longitudinal cracking in California and in other western US states is believed to be due the combination of moisture-related shrinkage, curling from temperature gradients, and traffic actions *(2)*.

Moisture-related shrinkage is also regarded as one of the more important phenomena determining the early-age performance of JPCP for several reasons: the relatively low strength of the early-age concrete; the relatively high rate of moisture-related shrinkage during the concrete's early age; and the inability of concrete slabs to bend or contract until transverse joints are deployed *(3)*.

The importance of moisture-related shrinkage is supported by the preliminary conclusions obtained in the Caltrans Partnered Pavement Research Center (PPRC) Project 4.58B "Development of Improved Guidelines and Designs for Thin Whitetopping." Up to 800 με of moisture-related shrinkage was measured in a set of unrestrained shrinkage prisms located outdoors, and up to 550 με of differential drying shrinkage (top versus bottom of the slab) was measured in the full-scale concrete overlay on asphalt (COA) sections that were built and monitored for

PPRC Project 4.58B *(4)*. Based on current mechanistic-empirical (ME) modeling practice for concrete pavements, those shrinkage levels would result in tensile stresses that far exceed the flexural strength of the concrete. Still, none of the slabs cracked under the environmental actions, which included moisture-related shrinkage as well as thermal actions.

Current ME design procedures oversimplify the prediction of moisture-related shrinkage. Shrinkage is typically predicted by using models that have been calibrated using laboratory data, such as CEB MC90-99 *(5)*, ACI 209R-92 *(6)*, or B3 *(7)*. A combination of the last two models is currently implemented in the *AASHTOWare Pavement ME Design* software *(8)*. These models were calibrated using shrinkage data collected in the laboratory under constant temperature and air relative humidity (RH), but they have not been validated under field conditions. In the field, concrete temperature and air relative humidity fluctuate, and rainfall also plays a key role that current prediction models do not consider. (Note: The role of rainfall in determining the moisture-related shrinkage of the slabs was discussed in the earlier PPRC Project 4.58B research report *[4]*.)

Current shrinkage prediction models also have two other drawbacks. First, they have been conceived for uniaxial shrinkage, which is the main deformation mode in the prisms where laboratory shrinkage is typically evaluated. As a result, the models do not account for bending, the main deformation mode in JPCP and COA slabs. Second, the models have not been calibrated for mixes with admixtures, which are characteristic of most of the rapid-strength concrete (RSC) mixes that will potentially be used in concrete overlay construction in California. A new version of the B3 shrinkage model (named B4) considers the use of different admixtures in the concrete *(9)*, although its applicability to the RSC mixes used in JPCP pavement construction in the United States has not been verified.

Current ME design procedures also oversimplify the modeling of slab response to moisture-related shrinkage. The nonlinear component of this action is frequently ignored, and the *AASHTOWare Pavement ME Design (1)* is probably the most representative example. The time-dependence of the asphalt base stiffness is systematically ignored in the COA design procedures, so the same stiffness is used for the asphalt under both rapid traffic loads and slow moisture-related shrinkage actions. Because of the viscoelastic nature of asphalt, its stiffness may change by two orders of magnitude (i.e., by a factor of 100) between the two loading scenarios. Fortunately, asphalt will typically behave like a soft material in terms of restricting a slab's moisture-related shrinkage deformation. Concrete stiffness is also oversimplified in current ME design procedures as its creep/relaxation capacity is ignored.

There is enough evidence to conclude that there is a major difference in the impact that moisture-related shrinkage has on the performance of concrete pavements and the way shrinkage is predicted and modeled in current ME procedures.

1.2 Objective

The objective of this research is to evaluate how moisture-related shrinkage accumulates in concrete pavements and to determine the structural response of the COA slabs to the shrinkage action. This research addresses the following main questions:

- What moisture-related shrinkage takes place in the concrete overlay on asphalt (COA) slabs?
- Do shrinkage prediction models work for rapid-strength concrete (RSC) mixes?
- What is the relationship between laboratory and field shrinkage?
- What is the stress due to moisture-related shrinkage?
    - What is the role of asphalt viscoelasticity?
    - What is the role of concrete creep?
    - What is the role of concrete surface microcracking?
    - Are there any other stress relaxation mechanisms?

1.3 Research Approach

Fifteen COA sections were built at the University of California Pavement Research Center (UCPRC) facility in Davis, California, on February 23 and 25, 2016 *(10)*. Their construction was part of Caltrans PPRC Project 4.58B, whose primary goal is to develop recommendations and guidance on the use of thin COA as a rehabilitation alternative for California. Six of the fifteen sections were instrumented with a total of 245 sensors to measure the response of the concrete slabs to environmental actions and cement hydration. In this report, these six sections are referred to as "ENV sections." These ENV sections included two slab sizes (full-lane width and half-lane width), two curing procedures (with a curing compound and with a shrinkage-reducing admixture), and four types of concrete mixes (three with portland cements, Type II/V and Type III, and one with calcium sulfoaluminate cement). Chapter 3 of this report includes a brief description of the ENV sections and their instrumentation.

In addition to the COA sections, eight unrestrained shrinkage prisms were fabricated during construction of the overlay on February 25, 2016, using the same mixes and the same curing procedures. After the overlay construction, the prisms were left outdoors near the test track to subject both the COA sections and the prisms to the same environmental conditions. These prisms were later used to measure the unrestrained expansion-

contraction of the different concrete mixes since the prisms were not bonded to any support. These prisms and their instrumentation are described in Chapter 3 of this report.

The strain measured in the unrestrained shrinkage prisms was used to backcalculate the moisture-related shrinkage of the concrete. In the backcalculations, this shrinkage was assumed to change linearly during each day and it was allowed to change from day to day. This approach made it possible to determine the evolution of moisture-related shrinkage versus time. A similar approach was followed for analyzing the measured strain in the ENV sections. For these sections, the strain measured in the slabs was used to backcalculate the mean moisture-related shrinkage (average of the top and bottom of the slab) and the differential drying shrinkage (difference between the top and bottom of the slab).[1] The time period analyzed starts at the construction of the overlays in February 2016 and extends to May 31, 2017. Using the evolution of both components of slab shrinkage provided the information needed to answer the first question in Section 1.2: *What moisture-related shrinkage takes place in the COA slabs?* These findings are presented in Chapter 4.

Moisture-related shrinkage was also measured in the laboratory following ASTM C157 (23°C [73°F] and 50% air RH). The shrinkage measured in each of the four mixes was compared with predictions made by the ACI 209R-92, B3, and B4 models. This comparison allowed an answer to be formulated for the second question in Section 1.2: *Do shrinkage prediction models work for rapid-strength concrete (RSC) mixes?* These findings are presented in Chapter 5.

However, extrapolating laboratory test results to field conditions remains the main challenge for the following reasons: both the concrete temperature and the RH of the air fluctuate under field conditions; the rewetting of concrete after rainfall events distorts the time evolution of moisture-related shrinkage considerably; and shrinkage in prisms is typically measured in the laboratory as uniaxial strain and so the extrapolation to predict slab bending due to differential shrinkage (top compared to bottom) is not straightforward. Addressing this challenge drove the work to answer the third question in Section 1.2: *What is the relationship between laboratory and field shrinkage?* This question is particularly relevant for current shrinkage prediction models (CEB, ACI, B3, B4) since they were calibrated under laboratory conditions (with constant temperature and air RH). To answer this question, model B4 was recalibrated using the shrinkage measured in the laboratory for each of the four mixes used in the COA test track. The model results were then extrapolated to field conditions using the time-hardening incremental-recursive approach used in *CalME (11),* the ME design software for asphalt pavements of the California Department of

[1] Note that the term "moisture-related" is used for the mean shrinkage since it includes both autogenous and drying shrinkage, while the term "drying" is used for the differential shrinkage since it is caused by drying (external drying) gradients versus depth.

Transportation (Caltrans). The time-hardening approach is used in *CalME* to extrapolate asphalt fatigue damage in laboratory tests, under constant loading and temperature conditions, to field conditions where both temperature and loading fluctuate. These findings are presented in Chapter 6.

This research addressed the last question from Section 1.2: *What is the stress due to moisture-related shrinkage?* The main challenge in answering this question is that concrete stress was not measured in the slabs (i.e., there was no actual measure of concrete stress). In fact, the only experimental evidence of actual stress in the concrete was the presence of environment-related surface microcracking in one of the sections. Tensile stresses likely reached the tensile strength of the concrete in that section, but this did not occur in any of the other sections. Only having an upper bound of actual tensile stress is not an ideal experimental scenario, and it was definitely not enough to fully answer the question above. However, it was enough to prove the existence of a series of stress-release mechanisms. Some of these mechanisms were identified and modeled with the finite element method (FEM). One of these mechanisms is asphalt viscoelasticity, which was characterized in the laboratory using frequency sweep complex modulus testing at different temperatures. Concrete creep is another stress-release mechanism that was considered. No testing was conducted to characterize concrete creep, so instead a creep prediction model was used. The research also considered the role of surface microcracking as a stress-release mechanism in the concrete, but its effect was not modeled. These findings are discussed in Chapter 7.

2 LITERATURE REVIEW

2.1 Evaluation of Moisture-Related Shrinkage in the Field

One of the earliest estimations of the curling-warping[2] level in concrete pavements was conducted in Florida and published in 1987 *(12)*. Armaghani et al. showed that a positive (top larger than bottom) temperature gradient of 5°C (9°F) was required to flatten out a pavement slab. This finding was attributed to shrinkage differentials through the depth of the slab. A number of experimental studies have been conducted since 1987 where the curling-warping level in concrete slabs was evaluated by following different procedures that can be classified into four major groups:

(1) *Profile-based methods.* The longitudinal and/or the transverse profiles of the slabs are measured with a profiler. A mechanistic model is then used to determine the hygrothermal[3] action that would explain the profiles measured in the slabs. The mechanistic model is typically based on either Westergaard equations or the finite element method (FEM). The hygrothermal action is typically quantified in terms of an equivalent linear temperature difference (ELTD) or a similar parameter. This approach requires the mechanistic definition of the pavement structure.

(2) *Structural response-based methods.* The structural response of the slabs is measured under a known load. Typically, corner deflection under the falling weight deflectometer (FWD) is measured since this response variable is highly dependent on the slab curling-warping level. A mechanistic model is then used to estimate the structural response. The curling-warping level of the slabs can be backcalculated by matching measured and modeled responses. The curling-warping level is typically quantified in terms of an ELTD or a similar parameter. This approach also requires the mechanistic definition of the pavement structure. An alternative method within this group is measuring the daily evolution of corner or edge displacements (i.e., the evolution due to changes in temperature gradients in the slab). Again, slab curling-warping level is backcalculated by matching measured and modeled responses.

(3) *Direct measurement of curling-warping strain.* The curling-warping level can be quantified in terms of the differential strain through the thickness of the slab—that is, the difference between top and bottom of the slab strains. These strains can be measured by using strain gauges, typically the vibrating wire type. This approach is probably the most accurate for measuring curling-warping levels, but it requires instrumenting the slabs and monitoring the response.

(4) *Calibration of mechanistic-empirical design procedures.* This approach is based on the high sensitivity that JPCP transverse top-down cracking presents versus the slab curling-warping level. In this approach,

[2] The term "curling" is typically used in the concrete pavements literature as a synonym for bending under temperature gradients. The term "warping" is typically used as a synonym for the bending caused by drying shrinkage.

[3] The term "hygrothermal strain" was used by Bazant and Baweja to refer to the sum of thermal and moisture-related strains *(7)*.

a permanent (built-in) curing-warping level is introduced in the mechanistic model. Then, the built-in curing-warping is backcalculated during the calibration of the ME procedure. This is the approach used in the *AASHTOWare Pavement ME Design (8)*.

One of the most comprehensive experimental research projects to quantify the curling-warping level in in-service concrete pavements, Inertial Profile Data for Pavement Performance Analysis, was sponsored by the Federal Highway Administration (FHWA) *(13)*. In that project, 38 JPCP sections across the United States were monitored during a 15-month evaluation period. The mean (mean during the evaluation period) curvature of the slabs was determined based on that data together with daily and seasonal variations. The mean curvature of the slabs was not always upward: approximately 25% of the sections experienced downward mean curvature and another 25% were essentially flat on average *(14)*. Slab curvature was quantified in this study in terms of the pseudostrain gradient, which is the strain gradient required to bend a flat slab into the shape measured with the profiler. This gradient reflects temperature gradients plus differential drying shrinkage. Calculated mean pseudostrain gradients ranged from approximately -2.5 με/mm (-64 με/in., upward) to +1.5 με/mm (+38 με/in., downward).

A similar study was conducted with the concrete pavement sections in the Long-Term Pavement Performance Specific Pavement Study site 2 in Arizona *(15)*. This study showed that 17 of 19 JPCP sections were bent upward after 16 years in service. The two sections that were bent downward were built with high-strength concrete. In addition, almost all the sections (12 of 13) built with normal-strength concrete experienced upward warping between the first profile evaluation, around four months after construction, and the last evaluation, 16 years later. The warping level of almost all the sections (five of six) built with high-strength concrete, on the other hand, changed in the opposite direction (downward) after the first evaluation.

Another similar study was conducted on the MnROAD full-scale test road *(16)*. In this study, transverse profiles were measured on 11 JPCP sections. The curvature of the slabs was quantified as the ELTD that would match the profile measured in the slabs. *ISLAB2000* finite element software was used to calculate the slabs' deformation, and the model parameters were estimated based on FWD backcalculation and laboratory test results in the MnROAD database. Concrete temperature was recorded during the profiler evaluations so that the effects of temperature could be removed from the backcalculated ELTD. By doing so, the resulting temperature difference reflected the joint action of the construction built-in temperature (that is, the temperature profile that existed as the concrete set) and moisture-related shrinkage. This net ELTD was referred to as the "equivalent built-in temperature difference" (EBITD). The EBITD ranged from -3°C to -44°C (-5°F to -79°F, upward). An attempt was made to determine the EBITD using FWD corner deflection testing, but consistent results were obtained for

only two of the eleven sections. The EBITD determined for these two sections were much smaller (in absolute value) than the values obtained with the profiler approach.

A major effort to estimate the effects of curling and warping was conducted by the UCPRC in the late 1990s, in connection with the use of fast-setting concrete *(17)* at Palmdale, California. Static strain gauges embedded in the slabs indicated a differential strain (top to bottom of the slab) of -250 με for 200 mm (8 in.) thick slabs. This differential strain, which was attributed to drying shrinkage, was enough to cause top-down cracking of the longest slabs (5.5 m and 5.8 m [18 ft. and 19 ft.] long) before any traffic load was applied on the pavement. Later research on the Palmdale sections showed that the EBITD ranged from 0°C to -19°C (0°F to -34°F, upward) in the slabs with high deformation restraint (dowels and tied concrete shoulders or widened slabs) and from -19°C to -36°C (-34°F to -65°F, upward) in the slabs with low deformation restraint (no dowels or tied concrete shoulders) *(18)*. These EBITD values were obtained based on deflections measured under the load of a heavy vehicle simulator (HVS) during a 24-hour period. The high EBITD values were attributed to daytime construction, the use of fast-setting concrete, and the dry conditions of the Palmdale desert.

The high EBITD levels that were backcalculated from the Palmdale project were shown to have significant consequences on the expected fatigue life of the JPCP sections. Because of the high EBITD levels, the critical distress mechanism changed from bottom-up to top-down cracking *(18)*. The same conclusion was reached by Yu et al. *(19)* and by Beckemeyer et al. *(20)*, based on experimental data collected in concrete sections located on Interstate 80 in Colorado and Pennsylvania, respectively. They estimated EBITD using the measured slab displacements caused by variations of the temperature profile of the slab. The large vertical displacements that were measured in both studies at slab corners and edges could be only explained by the existence of a considerable strain gradient locked in the slabs. The EBITD backcalculated by Yu et al. in the Colorado sections was -11°C (-20°F, upward), while Beckemeyer et al. obtained -9°C (-16°F, upward) on open-graded granular materials and -7°C (-12°F, upward) on asphalt-treated permeable bases in two sections placed in Pennsylvania.

Using the slab profiles measured with a dipstick, Yu and Khazanovich *(21)* determined the EBITD in the same Pennsylvania sections evaluated by Beckemeyer et al. *(20)*. The results were much higher than the EBITD values (in absolute value) obtained by Beckemeyer et al. using the thermal response of the slabs. Based on the dipstick profiles, the EBITD in the slabs on top of the open-graded granular base was -37°C (-67°F, upward), roughly four times the value resulting from using slab thermal response. Yu and Khazanovich stated that even half of that EBITD value would have been enough to cause the sections to fail in their first year of service, which did not happen. They concluded that the actual slab support was much better than the support calculated from the slab profiles and, consequently, that the built-in curling and warping stresses were not as high as those obtained using

the profiler approach. Yu and Khazanovich considered the approach based on the thermal response of the slabs to be representative of actual slab support and the effective built-in curling and warping. It should be noted that the MnROAD study *(16)* previously discussed also reported that the EBITD values based on the slab profiles were much larger (in absolute value) than the values based on the structural response of the slabs.

A few studies have evaluated curling-warping levels based on static strain gauge records. Wells et al. *(22)* estimated moisture-related shrinkage strains of -98 με and -71 με at the top of unrestrained and restrained slabs, respectively, in a JPCP section in Philadelphia, Pennsylvania. This study showed that drying shrinkage can vary significantly within the same slab. Specifically, drying was higher near the free edges of the slab than in the rest of the slab. Another important observation from this study was that moisture-related shrinkage increased drastically during the first 50 days after construction. This result is in line with the UCPRC Palmdale experience *(17)*, where static strain was also recorded with vibrating wire strain gauges (VWSGs).

Jeong and Zollinger *(23)* determined the evolution (versus time) of moisture-related shrinkage in a JPCP section in Texas. Based on slab displacements measured with linear variable displacement transducer (LVDT) sensors, they quantified the moisture-related shrinkage in terms of EBITD. The EBITD values they determined were -0.9°C, -3.7°C, -5.0°C, and -21.2°C (-1.6°F, -6.7°F, -9°F, -38.2°F) one day, three days, six days, and two years after construction, respectively. Rao et al. *(24)* also determined the evolution of EBITD in a JPCP slab in Mankato, Minnesota, by measuring slab profiles with a dipstick right after construction, and after three days, fifteen days, forty days, and two years. An interesting finding from this study is that the EBITD decreased (in absolute value) between forty days and two years, which the authors attributed to concrete creep. Still, the EBITD was as high as -21.9°C (-39.4°F) after two years.

The national calibration of the *Mechanistic-Empirical Pavement Design Guide* (*MEPDG*) *(1)*, published in 2004, is an example of a fourth approach for determining the curling-warping level of concrete pavements slabs. A permanent curling-warping ELTD of -5.6°C (-10°F) was estimated in the *MEPDG* calibration. This permanent curling-warping parameter reflects the temperature gradients built in during slab construction (the temperature profile when the concrete sets) plus the unrecoverable moisture-related shrinkage. This parameter was obtained through model optimization, with the goal of minimizing the error of performance predictions in terms of transverse cracking. The approach essentially adjusts the ELTD to reflect any stress reducing phenomena that are occurring in the slabs.

2.2 Shrinkage Considerations in Current Concrete Pavement Mechanistic-Empirical Design Procedures

The *MEPDG*—currently implemented in the *AASHTOWare Pavement ME Design* software *(8)*—and *HIPERPAV (2)* are two acknowledged mechanistic-empirical pavement design and modeling procedures, and both consider concrete moisture-related shrinkage. The following discussion reviews the approach followed by each procedure, including the steps required to predict moisture-related shrinkage and to model its effects on pavement performance:

- Ultimate shrinkage
- Autogenous shrinkage
- Shrinkage profile
- Shrinkage evolution versus time
- Concrete creep
- Shrinkage use in performance models

2.2.1 Ultimate Shrinkage

Concrete ultimate shrinkage, $\varepsilon_{Sh\infty}$, is a parameter of the B3 *(7)* and ACI *(6)* shrinkage prediction models. It is the asymptotic value (long term) of the moisture-related shrinkage under a given constant value for the RH of the air (0% in the B3 model and 40% in the ACI model). Both the *MEPDG* and *HIPERPAV* include prediction models that estimate this parameter.

The 1999 first-release version of *HIPERPAV (25)* used the B3 shrinkage prediction model published by Bazant and Baweja in 1995 *(7)*. However, *HIPERPAV* II used an earlier version of the B2 model published by Bazant and Panula in 1978 *(26)*. The model was updated because a validation effort conducted within the framework of *HIPERPAV* showed that using the B2 model resulted in better predictions of drying shrinkage than the B3 model for a range of mix designs *(27)*. The documentation released with *HIPERPAV* III *(2)*—the latest version of the software—does not indicate the shrinkage prediction model.

There seems to be an inconsistency in the shrinkage prediction approach used in the *MEPDG*, based on the 2004 documentation *(1)*. This procedure defines concrete ultimate shrinkage as the "ultimate shrinkage at 40 percent relative humidity," but it uses the B3 prediction model, where ultimate shrinkage corresponds to 0% air RH. The ACI 209R-92 shrinkage model uses 40% air RH to define the ultimate shrinkage. Fortunately, the error associated with this difference is relatively small, since the long-term shrinkage does not usually change much when air RH drops below 40%. Another important point about the *MEPDG* shrinkage prediction approach is that the level 1 option for determining the ultimate shrinkage is unavailable. The 2004 *MEPDG* documentation states explicitly that testing to determine this parameter is "is not a practical approach since it could take several years to realize

the ultimate shrinkage strain" *(1)*, while the 2015 *MEPDG Manual of Practice (8)* states that such testing is "not practical."

Neither the *MEPDG* nor *HIPERPAV* documentation comments on the applicability of the shrinkage prediction models to RSC mixes. According to Bazant and Baweja *(7)*, the B2 and B3 models are not applicable to special concretes containing various admixtures, pozzolans, microsilica, or fibers. This statement raises questions about the applicability of the models to the mixes that will potentially be used in thin COA construction in California, since these mixes will likely include fibers in addition to water reducers, accelerators, and other admixtures.

The limitations for admixtures of the B2, B3, and ACI models have been overcome with the B4 model *(28).* This model, released in 2015, builds on the B2 and B3 models and incorporates data from 1,400 creep and 1,050 shrinkage laboratory tests as well as field data from 69 bridges. The shrinkage prediction equations in the B4 model consider the use of different admixtures in the concrete. The applicability of this model to the RSC mixes used in the United States has yet to be validated.

2.2.2 *Autogenous Shrinkage*

As explained in Section 1.1, autogenous shrinkage is the component of the moisture-related shrinkage that takes place because of concrete self-desiccation, which is the internal desiccation that occurs in mixes with a low water/cement (w/c) ratio. The desiccation occurs because of cement hydration water demand in the mix and the net volume reduction that results from the cement hydration reaction. Autogenous shrinkage can represent up to 50% of the total moisture-related shrinkage in mixes with around 0.30 w/c *(29)*.

The B3 model, which is used in *AASHTOWare Pavement ME Design,* does not specifically account for autogenous shrinkage. Part of this shrinkage is included indirectly in the model, but only the part that takes place during the drying period in laboratory shrinkage tests. The *AASHTOWare Pavement ME Design* documentation *(1,8)* does not include any reference to autogenous shrinkage.

HIPERPAV specifically considers autogenous shrinkage in mixes with w/c below 0.40. For these mixtures, *HIPERPAV* II uses the Jonasson and Hedlund *(30)* shrinkage prediction model developed for high-performance concrete with w/c below 0.40 and 28-day compressive strength over 80 MPa (11,600 psi). The model estimates both drying and autogenous shrinkage with simplified equations based on w/c. In fact, *HIPERPAV* II evaluates both the B2 and Jonasson and Hedlund models for mixes with w/c below 0.40 and then selects the model that results in the highest total moisture-related shrinkage. *HIPERPAV* II performs this comparison of the predictions

made by the B2 and Jonasson Hedlund models because the two models have yielded widely varying predictions for concrete mixes with 0.40 w/c *(29).* In theory, the two models should make similar predictions for that w/c ratio. The documentation released with *HIPERPAV* III *(2)*—the latest version of the software—does not specify which autogenous shrinkage prediction model is used.

2.2.3 Shrinkage Profile

The *AASHTOWare Pavement ME Design* assumes that shrinkage reaches its maximum value at the surface of the slabs and decreases linearly versus depth until it reaches zero at 50 mm (2 in.) depth. Below this depth, the *AASHTOWare Pavement ME Design* assumes shrinkage to be zero *(1)*. This profile is incompatible with the nature of autogenous shrinkage, which should be treated as independent of slab depth since the process is governed by concrete self-desiccation.

Based on the assumed shrinkage profile, the *AASHTOWare Pavement ME Design* determines an ELTD that is then added to the thermal effects during the calculation of stress. This ELTD is determined based on the shrinkage at the slab surface using a formula reported in the 2004 documentation *(1)*. This approach has several flaws. First, evidence provided by continuum mechanics shows that the reported formula underestimates slab bending by a factor of two. Second, the ELTD approach ignores the nonlinear component of the moisture-related shrinkage. Tensile stress caused by the nonlinear component of the moisture-related shrinkage can be as high as—or even higher than—the stress produced by the linear component.

The shrinkage profile in the first-release version of *HIPERPAV (25)* followed the same bilinear profile used in the *AASHTOWare Pavement ME Design,* although the shrinkage depth was assumed to be zero at the slab half-depth. The documentation released with later versions of *HIPERPAV* does not specify the profile of the moisture-related shrinkage *(2,27,29)*.

2.2.4 Shrinkage Evolution Versus Time

All the previously mentioned shrinkage prediction models determine the evolution of moisture-related shrinkage by multiplying the long-term shrinkage by a "time function." The time functions differ from one model to another, but they are all monotonic functions of time that asymptotically tend to one—that is, they reach one in the long term. The following B3 and ACI 209R-92 time functions are examples.

B3 time function:

$$S(t) = \overline{\frac{h}{\tau_{sh}}}\sqrt{\frac{t - t_0}{}} \qquad \textbf{(2.1)}$$

ACI 209R 92 time function: $$S(t) = \frac{(t-t_0)^{\alpha}}{f+(t-t_0)^{\alpha}}$$ **(2.2)**

where: t is time
t_0 is the time when drying begins
α, f, τ_{sh} are the model parameters

Another commonality of the time functions is that they consider the size of the specimen (or concrete member). The larger the specimen, the slower the time function increases, and the smaller the specimen, the faster the time function increases. This effect is introduced via the parameters of the time function (τ_{sh} in Equation 2.1 and *f* in Equation 2.2). The size of the specimen is quantified in the B2, B3, and ACI models as the ratio between the volume of the specimen and the surface area of the specimen exposed to the air. The *MEPDG* uses the ACI time function (Equation 2.2) with default values for α and *f*, 1 (non-dimensional) and 35 days, respectively. This means that *AASHTOWare Pavement ME Design* uses a unique time function no matter the slab thickness. It should be noted that the default parameters of the ACI time function correspond to a volume/surface ratio of only 21 mm (0.83 in.), which is much lower than the ratios in standard JPCP and thin COA slabs.

All the previously mentioned shrinkage prediction models assumed uniaxial shrinkage because they were calibrated using the results of laboratory shrinkage tests conducted on prisms that were allowed to dry uniformly over their entire surface. Under these conditions, the specimens contract uniaxially due to drying. The B2, B3, or ACI models were not conceived for slab bending, which is the main effect that drying shrinkage produces on pavement slabs.

All shrinkage prediction models include a correction factor to account for the RH of the air. However, two problems exist when using these correction factors. First, the effect of RH on moisture-related shrinkage was not immediate. Second, the prediction models were calibrated under constant temperature and RH conditions. *AASHTOWare Pavement ME Design* simplifies this problem by adopting a unique air RH value for each month. That RH is used to determine the RH correction factor that is then applied to the ultimate shrinkage. This approach is equivalent to assuming that the RH of the specific month has been present since the time the concrete started to dry (t_0 in Equation 2.1 and Equation 2.2).

2.2.5 Concrete Creep

Early-age stress calculations in *HIPERPAV* are conducted by using an effective, creep-adjusted modulus of elasticity. This modulus accounts for instantaneous (elastic) strain and for creep strain. Creep compliance is estimated using the Umehara et al. tensile creep model from 1995 *(31)*. This model accounts for the age of the concrete at loading and for temperature, and it is based on a combination of Kelvin-Voight mechanical elements.

The advantages of the model are its simplicity and the fact that it is calibrated for early-age tensile creep. The model was calibrated for a single concrete mix under constant temperature and stress conditions, so its applicability as a general model for any concrete mix and for changing temperature and stress conditions is debatable. Another research effort was conducted within the framework of *HIPERPAV* II to implement a more comprehensive creep model, and several models were considered. The candidate model selected was developed by Westman in 1999 *(32)*. This model is based on a modification of the triple power law to account for early-age loading. Nonetheless, implementation of the model could not be achieved due to lack of validation data *(29)*. No change in the creep model is reported in the *HIPERPAV* III documentation *(2)*. *AASHTOWare Pavement ME Design* does not consider concrete creep when modeling the effects of moisture-related shrinkage. This means that the same concrete stiffness is used under rapid traffic loads (typically less than a few seconds) and under much slower moisture-related shrinkage action (days to years).

2.2.6 Shrinkage Use in Performance Models

AASHTOWare Pavement ME Design uses shrinkage in its faulting and cracking models. In the faulting model, shrinkage is used to estimate joint opening. The joint opening is then used to determine the contribution of aggregate-interlock to the LTE across transverse joints. In the cracking model, shrinkage is used to determine an ELTD that is added to the thermal effects during stress calculation.

HIPERPAV uses shrinkage together with temperature differentials for estimating early-age (up to 72 hours) concrete stresses. These stresses are compared with the early-age tensile strength to assess the risk of cracking. While *HIPERPAV* is focused on short-term performance, shrinkage is a long-term phenomenon in the *MEPDG*. This is one of the main differences between *HIPERPAV* and the *MEPDG.* It should be noted that none of the B2 or B3 shrinkage prediction models has been calibrated to predict early-age shrinkage, as stated by the RILEM Technical Committee TC-242-MDC *(9)*. This is also true of the ACI 209R-92 model.

2.3 Concrete Pavement Shrinkage Modeling Studies

Many of the curling-warping experimental studies referred to in Section 2.1 used modeling to link moisture-related shrinkage to the structural response of the slab. In those studies, modeling was typically conducted using Westergaard equations or the finite element method (FEM) with *Islab2000* or an earlier version of the program. The modeling approach is very similar in all these studies: concrete is modeled as a linear elastic material, and shrinkage is typically quantified as an ELTD through the thickness of the slab.

Few studies exist that attempt to predict shrinkage in concrete pavements. Jeong et al. *(33)* used the ACI 209R-92 model to estimate the moisture-related shrinkage in a JPCP section in Texas. They obtained a good agreement between model predictions and the shrinkage measured with static strain gauges and estimated an ELTD of -30°C (-54°F) in a 300 mm (12 in.) thick slab around one year after concrete construction.

The studies referenced in this literature review have typically remarked on the nonlinear nature of moisture-related shrinkage since it mostly takes place in the top portion of the slabs. However, those studies have not reported much regarding the stress due to the nonlinear components of shrinkage.

The creep/relaxation capacity of concrete is frequently remarked upon in the literature referenced here, but only one study was found where concrete creep was modeled in a pavement structure *(34)*. This theoretical study from 1998 focused on continuously reinforced concrete pavements. Creep was modeled by using the "effective Young's modulus," which is the elastic modulus divided by $(1+\phi)$, with ϕ being the creep coefficient. A maximum creep coefficient of 2.0 was assumed in that study. That is, creep strain in the long term would be twice the elastic strain (total strain would be three times the elastic strain).

It should be noted that the B3, B4, and ACI 209R-92 models consider creep and shrinkage as inseparable phenomena. Therefore, they include prediction equations for either a concrete creep compliance function (B3, B4) or a concrete creep coefficient (ACI) in addition to shrinkage. A major limitation of these creep prediction models in terms of the modeling of concrete pavements is that they have been developed based on compressive creep tests instead of tensile creep tests.

Tensile stresses created by moisture-related shrinkage are reduced by concrete creep/relaxation capacity. An order of magnitude for that stress reduction can be set based on laboratory experimental studies. Weiss et al. *(35)* studied moisture-related shrinkage on unrestrained and fully restrained specimens. They estimated that around 50% of the tensile stress in the fully restrained specimens was released due to concrete creep. Umehara et al. *(31)* used their tensile creep model, the one implemented in *HIPERPAV*, to estimate early-age concrete stresses in a wall-shaped structure. They concluded that the equivalent modulus of elasticity of the concrete at early ages decreases by more than 50% due to creep. Altoubat and Lange *(36)* compared the unrestrained shrinkage in beam-shaped specimens with shrinkage stress measured in fully restrained specimens. They concluded that tensile creep strain was around 50% of the unrestrained shrinkage strain when the specimens cracked.

The findings from these three experimental studies *(35,31,36)* indicate that the tensile creep/relaxation capacity of concrete is very high at the early age. These results agree with the 2.35 ultimate creep ratio assumed in the ACI

209R-92 model, although the ACI model is based on creep tests conducted in compression. One consideration is that concrete damage can take place during the creep/relaxation process, especially at the early age. An important outcome from the study by Altoubat and Lange *(36)* is that failure stress in the fully restrained specimens was around 20% percent lower than the tensile strength of the material. This outcome was attributed to damage suffered by the concrete during the relaxation process.

2.4 Summary of Literature Review

The literature review indicated the following main conclusions:

- A large number of experimental studies exist where the permanent curling/warping level of in-service concrete pavements has been evaluated. Typically, experimental data come from slab profiles, slab vertical displacements due to temperature gradients, or dynamic deflections under the FWD. The curling/warping level is typically quantified in terms of the ELTD that matches the slab deformation or response.
- Overall, the moisture-related shrinkage ELTD values determined in the different experimental studies are very high. Values around -20°C (-36°F) and even lower are frequently reported. Profiler-based ELTD values are more extreme (larger absolute value) than ELTD values based on the structural response of the slabs.
- Few studies exist that compare actual moisture-related shrinkage in concrete pavements—determined from slab profiles, displacements, or deflections—with results obtained from prediction models, despite several recognized shrinkage prediction models, such as B3 and ACI 209R-92, that have long been available.
- A major limitation of the B3 and ACI 209R-92 shrinkage prediction models is that they are not applicable to mixes with fibers and/or admixtures. The B4 model has overcome this limitation for mixes with admixtures, but the model has yet to be validated for the mixes that will likely be used for concrete overlay construction in California. In addition, neither the B3 nor ACI models were calibrated to predict early-age shrinkage.
- Concrete pavement ME design procedures and most modeling studies neglect concrete creep/relaxation capacity. *HIPERPAV* is an exception, however, since this software considers the effects of creep by using an effective, creep-adjusted modulus of elasticity.
- Based on laboratory experimental studies, concrete tensile creep/relaxation capacity can reduce early-age shrinkage stress in fully restrained specimens by around 50%.

- The B3, B4, and ACI 209R-92 models include prediction equations for concrete creep. These models have been calibrated based on creep tests conducted in compression, a major limitation for modeling concrete pavements. A few models exist that have been calibrated based on tensile creep data, but these models are much less comprehensive and lack solid experimental validation.

3 EXPERIMENTAL DATA

3.1 Concrete Overlay on Asphalt Environmental Sections

As discussed in Section 1.3, six of the fifteen COA sections that were built at the UCPRC facility in February 2016 were instrumented with a total of 245 sensors to measure the response of the concrete slabs to the ambient environment and cement hydration. The response of these six sections, which are referred to as "ENV sections," is analyzed in this report. This set of sections is the result of a partial factorial design with three factors: concrete mix, concrete curing procedure, and slab sizes (Figure 3.1). These factors are regarded as the most important in determining the response of the slabs to the ambient environment and the cement hydration process. The levels of each of these three factors are as follows:

- Concrete mix (each type of concrete mix has been assigned an abbreviated name that is used where appropriate throughout the report)
    - P2: 10-hour design opening time (OT) with Type II/V portland cement and a 0.33 water/cement (w/c) ratio
    - P2-ICC: Internally cured concrete based on the P2 mix (50% sand replacement with prewetted lightweight aggregates)
    - P3: four-hour design OT with Type III portland cement and a 0.31 w/c ratio
    - CSA: four-hour design OT with calcium sulfoaluminate (CSA) cement and a 0.42 w/c ratio

  Note: the Caltrans flexural strength requirement for opening time of RSC is 2.8 MPa (400 psi).
- Concrete curing procedures
    - Curing compound
    - Shrinkage-reducing admixture (SRA) sprayed (topical use)
- Slab size (each slab size has been assigned an abbreviated name that is used where appropriate throughout the report)
    - 6×6: Half-lane width, 1.8×1.8 m (approximately 6×6 ft.) slabs
    - 12×12: Full-lane width, 3.6×3.6 m (approximately 12×12 ft.) slabs

The levels of the three factors were set as part of the complete full-scale experiment design, which includes not only the ENV sections but the 15 sections built in February 2016 as well. The complete full-scale experiment design is described in Mateos et al. *(10)*, together with details of the construction process and results of the construction quality assurance/quality control (QA/QC) testing.

The 6×6 ft. sections were 9 m (30 ft.) long and 3.6 m (12 ft.) wide to accommodate five slabs in the longitudinal direction and two in the transverse direction. The two 12×12 ft. sections were 10.8 m (36 ft.) long and 3.6 m (12 ft.) wide to accommodate three slabs in the longitudinal direction and one in the transverse direction. The transverse end joints of the sections were intentionally disconnected from the rest of the sections to prevent the performance and structural response of one section from interfering with adjacent sections.

The asphalt base in the 6×6 environmental sections was a hot mix asphalt (HMA) that was built in 2012 and tested for an earlier Caltrans research project on full-depth reclamation. That asphalt layer was 60 mm (2.4 in.) thick, and its surface was micromilled before placement of the concrete overlay. The asphalt base in the 12×12 environmental sections was a new HMA, 90 mm (3.6 in.) thick, with a rubberized gap-graded overlay 30 mm (1.2 in.) thick. Both layers were built on October 13, 2015. No asphalt surface texturing was used on the 12×12 sections. A brief description of the COA sections, including the underlying structure, can be found in a 2020 UCPRC report *(4)*, and a more detailed description is included in a 2018 UCPRC report *(10)*.

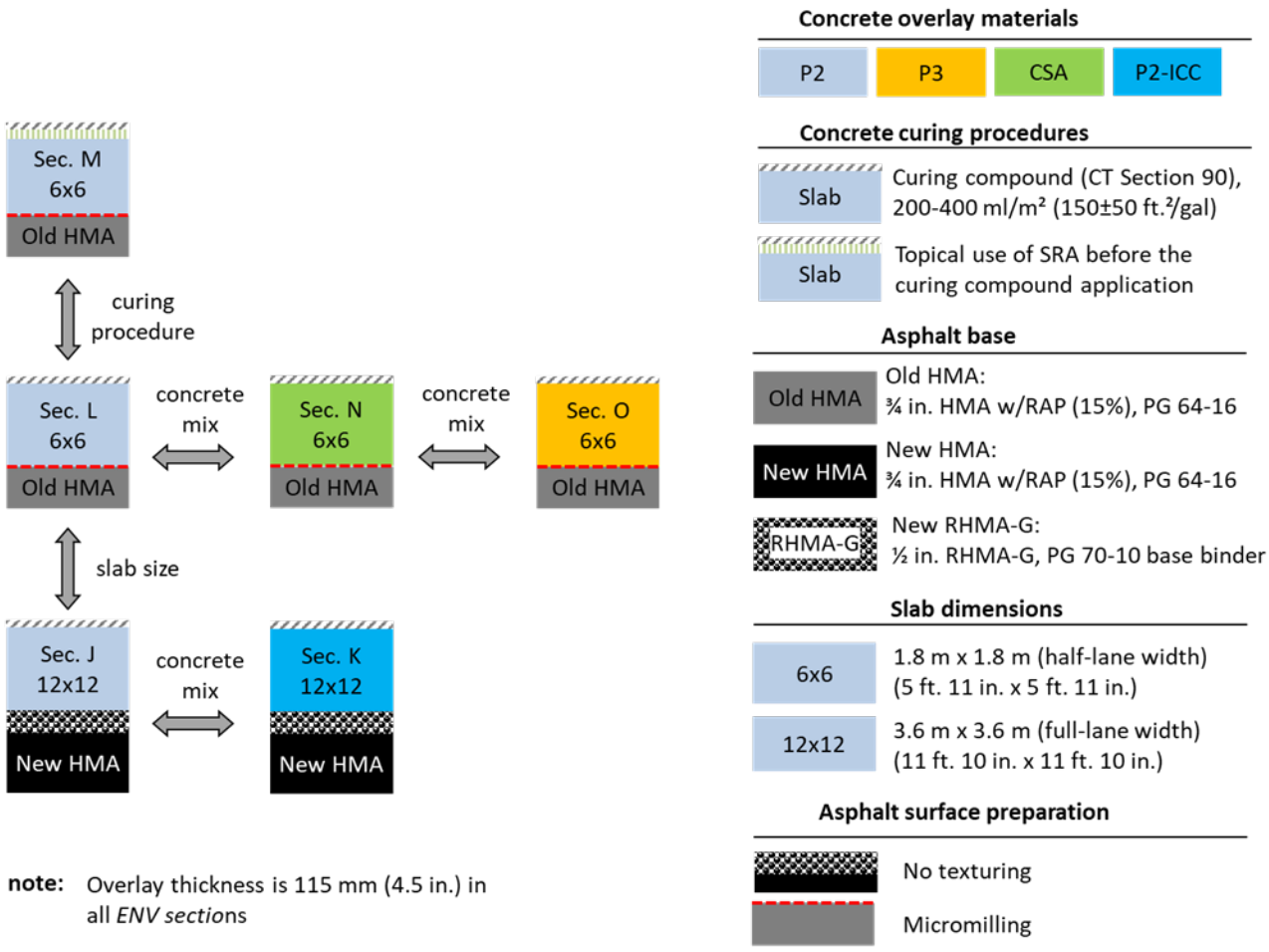

Figure 3.1: Partial factorial design behind the ENV sections.

3.2 Instrumentation of the Concrete Overlay on Asphalt Environmental Sections

The instrumentation of the ENV sections was designed with the goal of measuring the structural, thermal, and moisture-related responses of the slabs to environmental agents and the cement hydration process. The research presented in this report is mainly based on the following five response variables:

- *Temperature.* Temperature was measured with thermocouples that were installed in one slab of each ENV section, at three locations and at five depths: 5 mm (0.2 in.), 20 mm (0.8 in.), 50 mm (2 in.), 115 mm (4.5 in.), and 145 mm (5.7 in.). The last two depths correspond to the bottom of the slab and to the asphalt base, respectively. (Slab thickness was 115 mm [4.5 in.] in all ENV sections.)
- *Concrete relative humidity (RH).* This variable was measured with two types of sensors, although only the data collected with Campbell Scientific CS215-L sensors—which are referred to as "RHC sensors" in this report—were considered for this research. These sensors were installed at the center of a slab in each ENV section, at depths of 20 mm (0.8 in.) and 50 mm (2 in.).
- *Concrete moisture content (MC).* This variable was measured with embedded moisture sensors that are referred to by the shorthand "MC" in this report. These sensors included a wooden part where the moisture content was measured and reported. This sensor moisture content could be regarded as an indirect indication of the moisture content of the concrete but did not reflect the actual moisture content. These sensors were installed at the center of a slab in each ENV section, at depths of 20 mm (0.8 in.) and 50 mm (2 in.).
- *Concrete horizontal strain.* This variable was measured with vibrating wire strain gauges (VWSGs) that were installed in the center slab of each ENV section, at three locations and two depths: 20 mm (0.8 in.) below the slab surface and 20 mm (0.8 in.) above the slab bottom. They were configured this way to determine slab expansion/contraction as well as bending (curling and warping).
- *Slab displacement/transverse joint opening-closing.* The last variable was measured with an LVDT-based sensor called a joint displacement measuring device (JDMD). Sets of nine JDMD sensors were installed in each of the 6×6 sections: six to measure corner deflection (vertical displacement), one to measure edge deflection, and two to measure the opening and closing of transverse joints. Section K (12×12) was instrumented with seven JDMDs, and Section J was not instrumented with this type of sensor, shown in Figure 3.2. In all these cases, the JDMDs measuring vertical displacements were attached to an arm rod fixture that was anchored in the subgrade (Figure 3.3) to isolate the reference for the measurements from the slab movements.

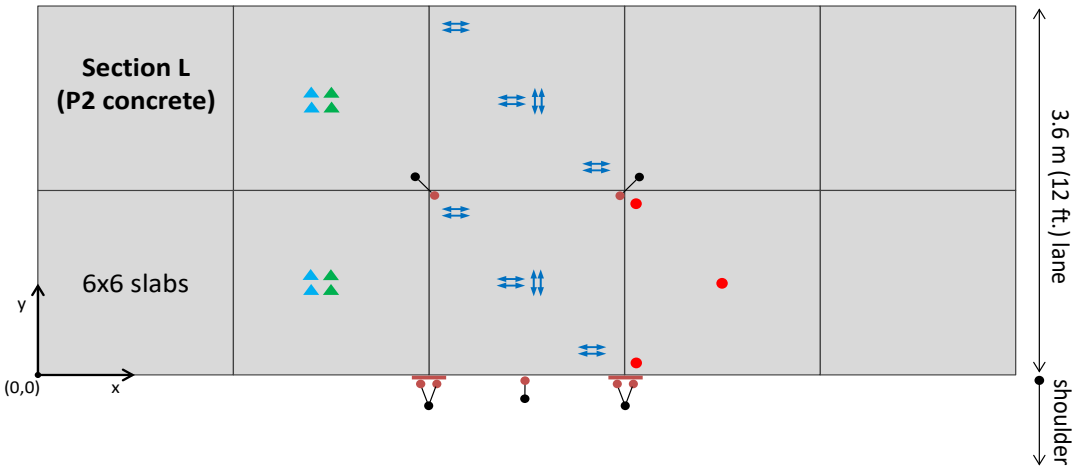

(a) Section L

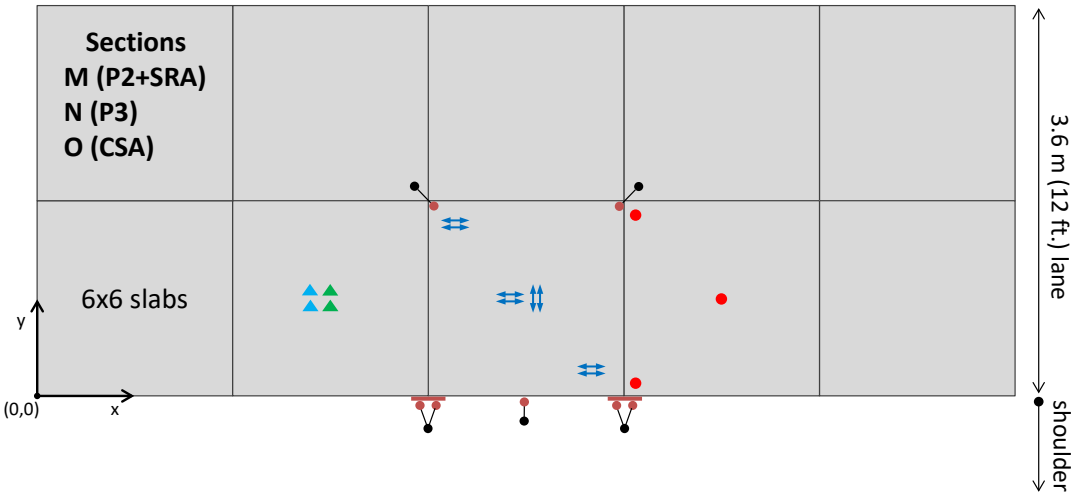

(b) Section M, N, and O

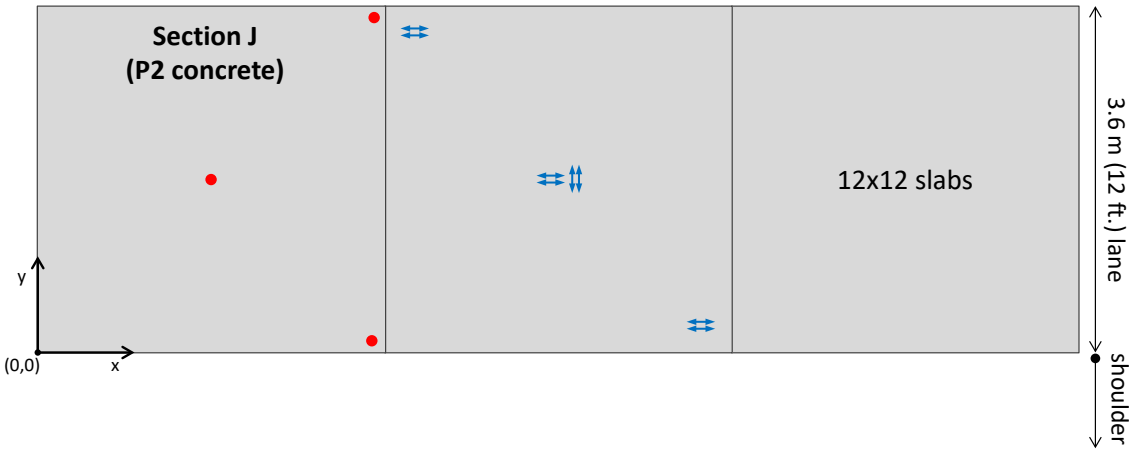

(c) Section J

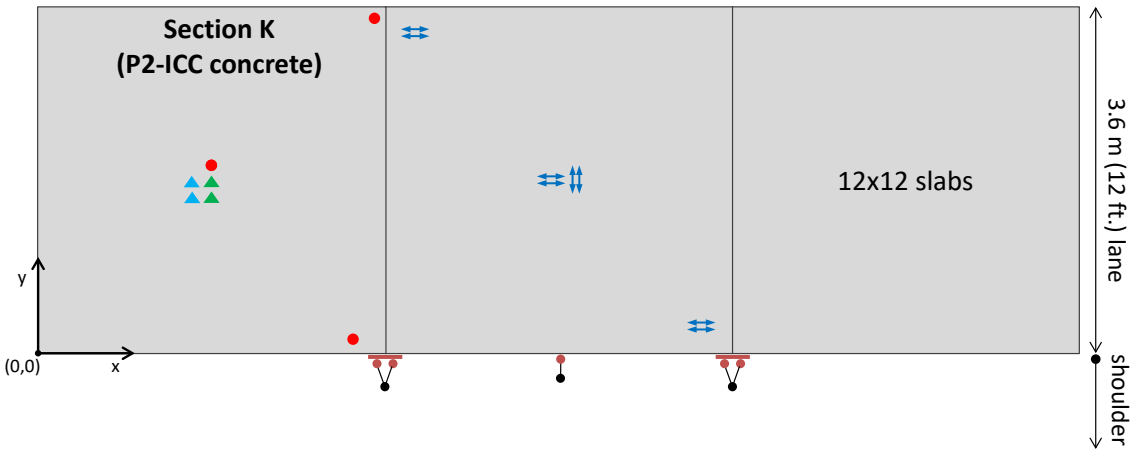

(d) Section K

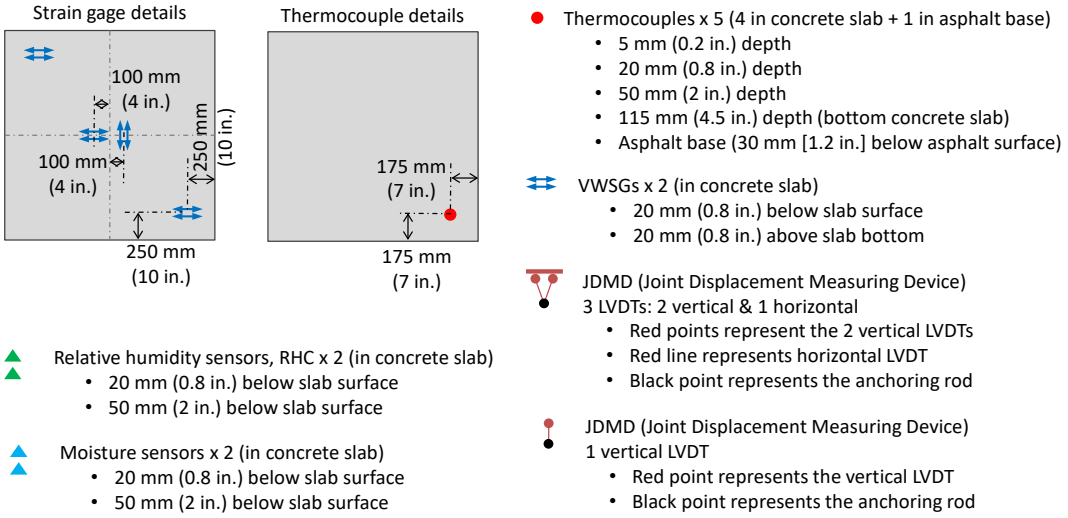

Notes: This figure shows the environmental instrumentation that supplied the data used in this report. Section L was instrumented with twice as many VWSGs and RH sensors than the other sections because its concrete type and slab size are representative of most of the COA sections.

Figure 3.2: Instrumentation of the ENV sections.

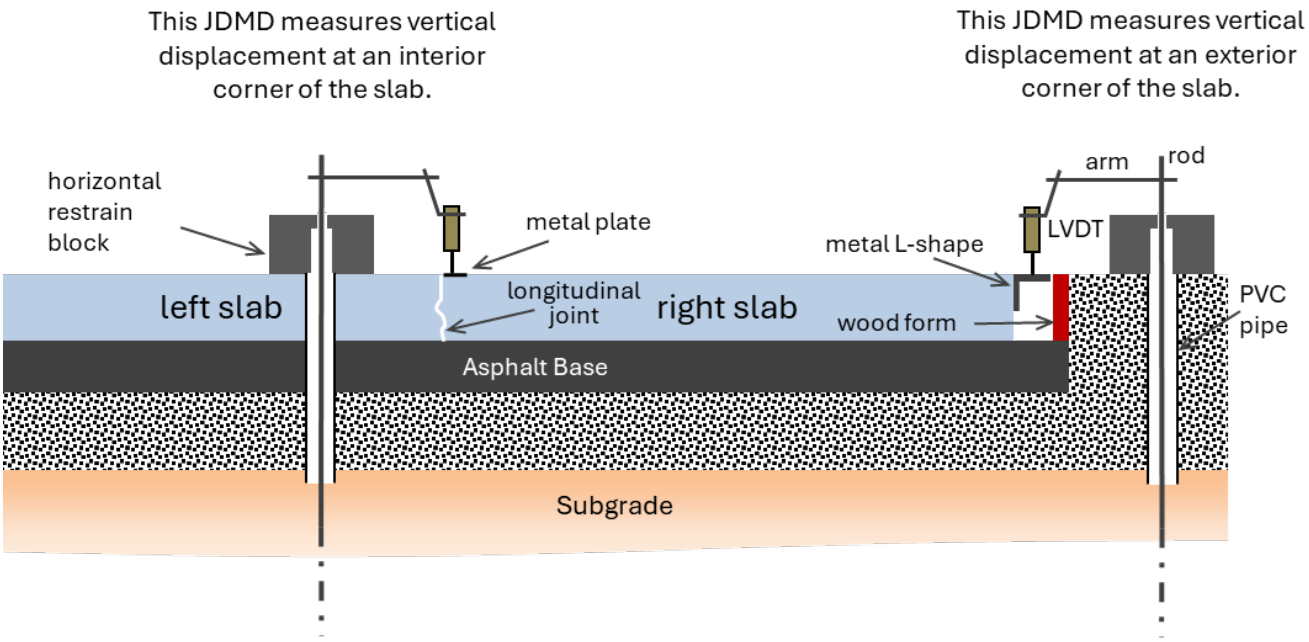

Figure 3.3: Anchoring system for vertical JDMDs.

Construction of the Lane 1 overlay (Section L) took place on February 23, 2016, and construction of the Lane 2 overlay (Sections J, K, M, N, and O) took place on February 25, 2016. Thermocouples, RH sensors, and VWSGs started to collect data the night before the overlay construction. Data collection by the JDMDs started after overlay construction since the installation of these sensors is relatively time-consuming and cannot be conducted before saw-cutting operations. For Section L, the JDMDs started to collect data at around 6:00 p.m. on February 23, the same day the overlay was placed and roughly eight hours after the concrete field setting time (which is defined in Section 3.4). JDMDs started to collect data on the Lane 2 sections on February 26, 2016, the day after overlay construction and around 24 hours (this time period varied from section to section) after the field setting time of the different mixes.

In the initial phase of data collection, the sampling interval was two minutes. After March 3, 2016, the sampling interval was set to five minutes, and after November 1, 2016, it was set to 20 minutes. The data analysis presented in this report uses one sample every 30 minutes during the first three days of data collection (February 23, 2016 to February 25, 2016) and one sample every hour after the initial data collection. As indicated in the introduction, the time period analyzed in this report extends to May 31, 2017. A summary of the characteristics of the sensors and their installation processes can be found in a 2020 UCPRC report *(4)*, and a more detailed description is included in a 2018 UCPRC report *(10)*.

3.3 Instrumentation of the Unrestrained Shrinkage Prisms

Eight unrestrained shrinkage prisms were prepared on the second day of the COA test track construction, on February 25, 2016. The prisms were prepared using the same mixes and following the same curing procedures used on the COA sections. Each of these prisms was instrumented with a VWSG to measure strain (Figure 3.4).

As with the VWSGs placed in the ENV sections, the VWSGs placed in the unrestrained shrinkage prisms started to collect data the night before the prisms were prepared. The VWSGs in these prisms were connected to the same data acquisition systems that collected data from the ENV sections, and, as with the ENV sections, the data collected up to May 31, 2017, are analyzed and presented in this report.

VWSG inside the mold

Prisms after demolding

Notes: Prisms 1 and 2: P2 cured with curing compound.
Prisms 3 and 4: P2 cured with SRA plus curing compound.
Prisms 5 and 6: P2-ICC cured with curing compound.
Prisms 7: P3 cured with curing compound.
Prisms 8: CSA cured with curing compound.
Curing compound and SRA were applied on the prisms, as in the sections.

Figure 3.4: Unrestrained shrinkage prisms.

3.4 Models for the Analysis of Strain Data

The strains measured with the VWSGs were analyzed using the incremental models in Equation 3.1 to Equation 3.3. Equation 3.1 is applicable to the strain measured in the unrestrained shrinkage prisms, ε_{USP}, while Equation 3.2 and Equation 3.3 are applicable to the strain measured with each pair of VWSGs (top and bottom of the slab). For each pair of strain gauges, ε_{MEAN} and ε_{DIFF} are defined in Figure 3.5. ε_{MEAN} quantifies slab expansion-contraction, while ε_{DIFF} quantifies slab bending.

Model for the unrestrained shrinkage prisms (USP):

$$\Delta\varepsilon_{USP} = \Delta\varepsilon_{Sh,T0} + CTE(t) \cdot \Delta T \quad \textbf{(3.1)}$$

where:
- ε_{USP} is the strain measured with the VWSG (ε=0 at field setting time)
- $\varepsilon_{Sh,T0}$ is the moisture-related shrinkage at the temperature T0
- *CTE(t)* is the time-dependent concrete CTE
- *t* is the time
- *T* is the prism temperature
- *T0* is the prism temperature when concrete sets (field setting time)

Model for the COA slabs (mean strain):

$$\Delta\varepsilon_{MEAN} = \Delta\varepsilon_{MEAN,Sh,T0} + \alpha \cdot CTE1(t) \cdot \Delta T_{MEAN} \quad \textbf{(3.2)}$$

where:
- ε_{MEAN} is the average strain measured with top and bottom VWSGs (ε_{MEAN} = 0 at field setting time)
- $\varepsilon_{MEAN,Sh,T0}$ is the moisture-related shrinkage component of ε_{MEAN} at the temperature *T0*
- *CTE1(t)* is the coefficient of thermal expansion (CTE) is the time-dependent equivalent CTE of the concrete slab
- α is a coefficient that reflects the restriction to slab expansion-contraction due to slab weight and slab interaction with the asphalt base (α is less than 1)
- *t* is time
- T_{MEAN} is mean slab temperature
- *T0* is the slab temperature profile when concrete sets (field setting time)

Model for the COA slabs (differential strain):

$$\Delta\varepsilon_{DIFF} = \Delta\varepsilon_{DIFF,Sh,T0} + \beta \cdot CTE2(t) \cdot \Delta ELTD \quad \textbf{(3.3)}$$

where:
- ε_{DIFF} is the differential strain measured with top and bottom VWSGs (ε_{DIFF} = 0 at field setting time)
- $\varepsilon_{DIFF,Sh,T0}$ is the moisture-related shrinkage component of ε_{DIFF} at the temperature *T0*
- *CTE2(t)* is the time-dependent equivalent CTE of the concrete slab
- β is a coefficient that reflects the restriction to slab bending due to slab weight, slab interaction with the asphalt base, and transverse joint locking or lack of deployment (β is less than 1)
- *t* is time
- *ELTD* is the equivalent linear temperature difference in the slab
- *T0* is the slab temperature profile when concrete sets (field setting time)

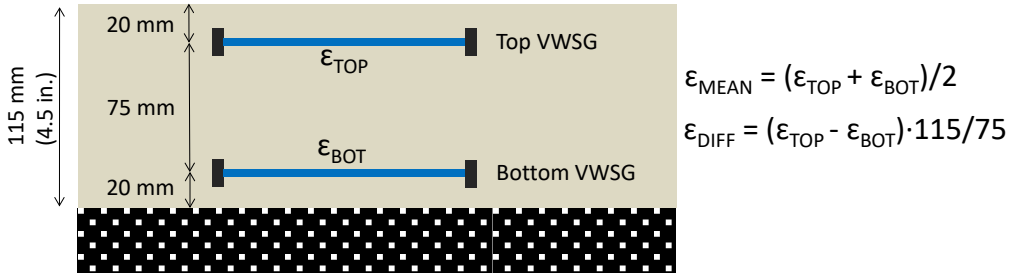

Figure 3.5: Strain composition used to analyze VWSG data in the COA slabs.

The models in Equation 3.1 to Equation 3.3 have two components, one that accounts for moisture-related shrinkage and another that accounts for thermal deformations. Thermal deformations in the ε_{USP} model are assumed to be proportional to changes in prism temperature, with the proportionality factor being the time-dependent CTE of the concrete. The time-dependency of the CTE was shown to be related to concrete moisture conditions *(4)*. Thermal deformations in the COA slabs are assumed to be proportional to changes in either slab mean temperature (ε_{MEAN} model) or slab ELTD (ε_{DIFF} model). In this case, the proportionality factors are the expansion-contraction thermal compliance of the slabs (α·CTE1) (for slab mean temperature) and the bending thermal compliance of the slabs (β·CTE2) (for slab ELTD).

The expansion-contraction thermal compliance (α·CTE1) is the ratio between slab expansion-contraction (quantified as the average of the top and bottom of slab strains) and the changes in slab mean temperature. The bending thermal compliance (β·CTE2) is the ratio between slab bending (quantified as the difference between the top and bottom of the slab strains) and the changes in the ELTD. Both thermal compliances changed in the COA environmental sections as a function of concrete moisture conditions, while β·CTE2 depended also—through β—on the level of deployment of the transverse joints *(4)*.

In formulating Equation 3.1 to Equation 3.3, moisture-related shrinkage is assumed to have two components. The first is the moisture-related shrinkage at the constant temperature T0, the temperature in the unrestrained shrinkage prisms when the concrete sets or the temperature profile in the COA slabs when the concrete sets. The second is the thermal component of the moisture-related shrinkage. This second component is added to the "pure" thermal deformations (based on the saturated CTE). The total thermal deformation is accounted for in the second term on the right-hand side of Equation 3.1 to Equation 3.3. The first term on the right-hand side of Equation 3.1 to Equation 3.3 is the first component of moisture-related shrinkage, the one at the constant temperature T0. That would be the moisture-related shrinkage if the temperature in the prisms or the temperature profile in the COA slabs was T0. A previous UCPRC report *(4)* includes the formulation of and further details about the three strain models.

It should be noted that strain in the three models was assumed to be zero at the concrete field setting time (FST). Field setting time is defined here as the time at which the concrete in the field is first able to develop stress when it is subjected to imposed deformations. The FST was determined for each of the environmental sections based on visual examination of strain and temperature evolution after concrete placement, following the methodology described in a previous UCPRC report *(4)*.

Two assumptions were made in analyzing the strain data using the three models: (1) the moisture-related shrinkage (constant temperature component) changes linearly within each day and (2) the CTE of the concrete and the thermal compliance of the slabs are constant within each day. Both assumptions are illustrated in Figure 3.6. After making these two assumptions, each of the models has two parameters per day:

- $\varepsilon_{Sh,T0i}$ and CTE_i are the parameters of the unrestrained shrinkage prisms ε_{USP} model
- $\varepsilon_{MEAN,Sh,T0i}$ and $\alpha \cdot CTE1_i$ are the parameters of the COA slabs ε_{MEAN} model
- $\varepsilon_{DIFF,Sh,T0i}$ and $\beta \cdot CTE2_i$ are the parameters of the COA slabs ε_{DIFF} model

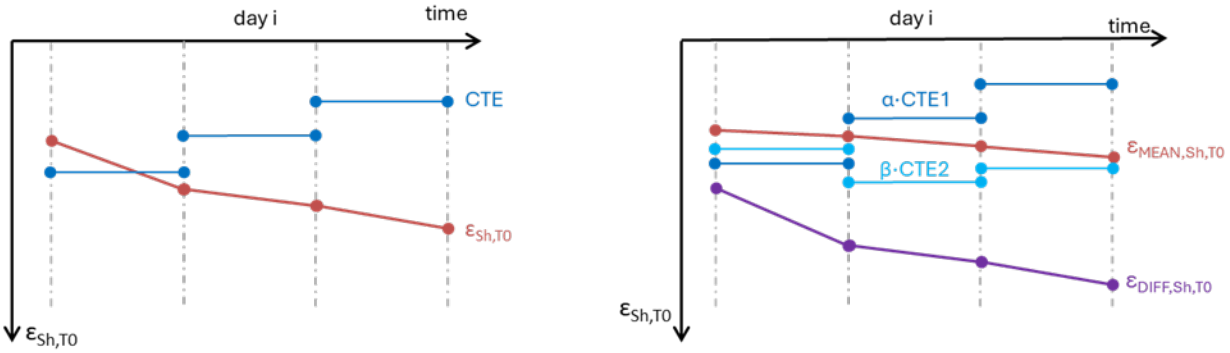

Unrestrained shrinkage prisms, ε_{USP} model **COA slabs, ε_{MEAN} and ε_{DIFF}, models**

Figure 3.6: Assumptions in the strain models.

The parameters of the models were determined through an iterative process of error minimization where the goal was to fit the strain recorded with the VWSGs. The mean square error of the ε_{USB} model was 7.2 με (pooled error of all unrestrained shrinkage prisms). An example of this fitting is shown in Figure 3.7. The mean square errors of the ε_{MEAN} and ε_{DIFF} models were 2.8 and 7.0 με, respectively (pooled error of all COA sections).

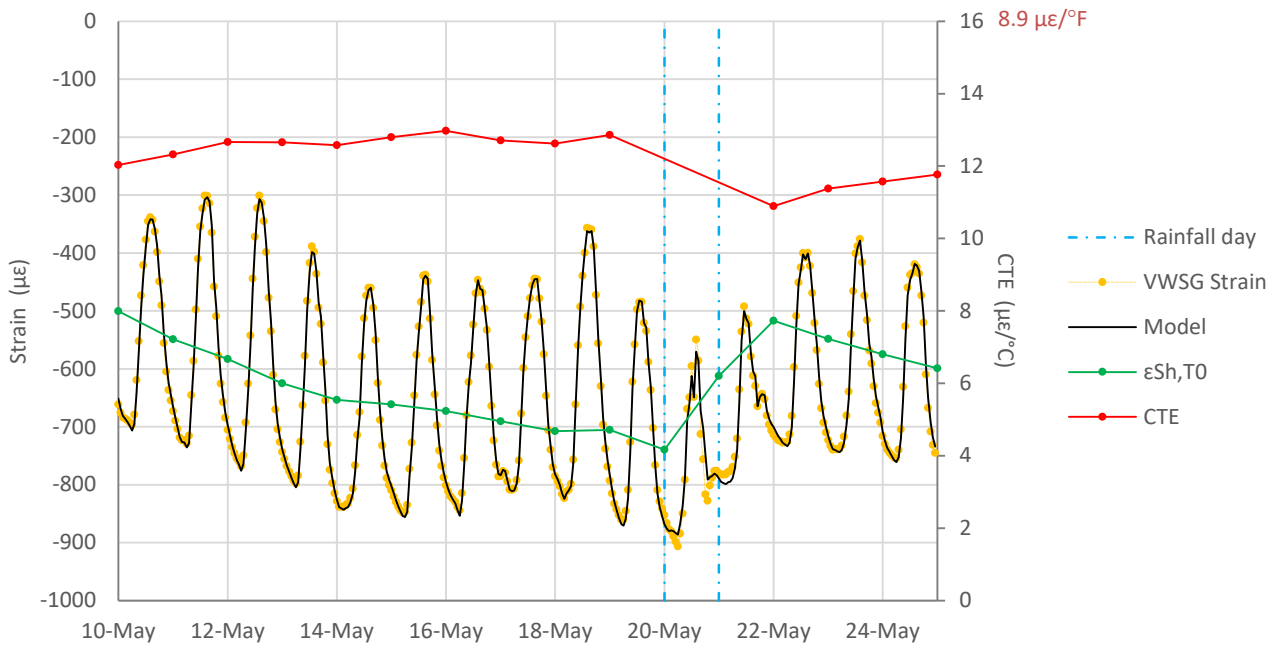

Notes: The series "Rainfall day" indicates days when rainfall occurred. The two vertical lines in the figure, on May 20 and May 21, indicate that some rainfall occured on those two days.

Figure 3.7: Example of fitting with the ε_{USP} model (Prism 1, P2 mix).

An important consideration must be noted at this point. The assumptions illustrated in Figure 3.6 (linear evolution of moisture-related shrinkage within each day and constant CTE within each day) were inaccurate on days when rainfall events occurred. For all mixes, a quick recovery of moisture-related shrinkage and a rapid decrease of the CTE were observed after rainfall *(4)*. Consequently, it is not realistic to assume a linear evolution of the moisture-related shrinkage and a constant CTE on these days. For these reasons, the moisture-related shrinkage backcalculated during the days with rainfall events (e.g., May 20 and May 21 in Figure 3.7), must not be regarded as a prediction of actual moisture-related shrinkage but rather a best-fit piecewise linear estimation.

3.5 Laboratory Testing

3.5.1 Concrete Laboratory Testing

The modeling presented in Chapter 7 of this report requires that a series of mechanical properties of the concrete be defined. In particular, it requires defining the stiffness, tensile strength, and moisture-related shrinkage. For this study, these properties were evaluated based on mixes prepared in the laboratory (lab mixes). The stiffness and strength testing was focused on three ages: design opening time (OT), four times the design opening time (4×OT), and 45 days. As explained in Section 3.1, the design opening time of the mixes was either 4 hours (P3 and CSA) or 10 hours (P2 and P2-ICC). The approach that was used for curing the specimens is presented in the

following discussion, and it is followed by a summary of the laboratory testing results obtained for each of the concrete mixes. Further details of the laboratory characterization can be found in a previous UCPRC report *(10)*.

3.5.2 Curing of Concrete Specimens

Stiffness and flexural strength testing was conducted on specimens that were cured following ASTM C192. Following this standard, the specimens that were not tested at opening time were demolded 24 hours after casting and stored at 23°C (73°F) in a moist curing room until testing.

The moisture-related shrinkage of the mixes was characterized following ASTM C157 except for the length of the curing period. The ASTM standard specifies that the specimens shall be stored in lime-saturated water until they reach the age of 28 days. For this research project, the specimens were stored in lime-saturated water until the age of 3 days. The curing period was shortened because it was believed the water storage until the 28-day age did not represent the average conditions of concrete pavement construction with RSC. The RSC develops strength much faster than standard concrete, and it is opened to traffic relatively soon after construction.

3.5.3 Concrete Stiffness

Concrete stiffness was characterized with the modulus of elasticity (E). This variable was measured following ASTM C469. According to that standard, a compressive load is applied to a cylindrical specimen in the longitudinal direction while the longitudinal deformation of the specimen is measured. The load is increased at a constant rate until reaching 40% of the compressive strength of the mix. The modulus of elasticity is determined as the chord modulus between 50 με and the strain corresponding to 40% of the compressive strength of the mix.

Three specimens per mix were tested at three ages: design OT, four times OT, and 45 days. Specimens were cylinders with a diameter of 150 mm (6 in.) and a length-to-diameter ratio of two. The results are presented in Figure 3.8, which shows that the four mixes resulted in similar stiffness at OT. The same occurred at four times OT. However, at 45 days, the stiffness of the portland cement mixes was much higher than the stiffness of the mix with CSA cement.

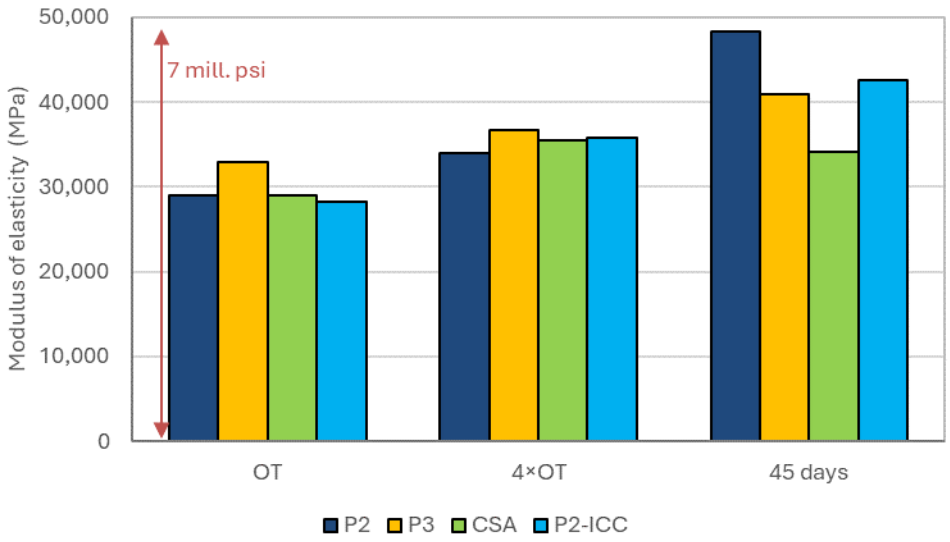

Figure 3.8: Modulus of elasticity of the lab mixes (ASTM C469).

3.5.4 Concrete Tensile Strength

Concrete tensile strength was characterized using flexural strength. This variable was measured following ASTM C469. According to that standard, the load is applied to a beam at the two central third points (third-point loading). The load is increased at a constant rate until the beam breaks. The peak load is used to determine concrete flexural strength (frequently referred to as the modulus of rupture).

Three beams per mix were tested at each testing age (OT, 4×OT, and 45 days), and the beams were 150×150×500 mm (6×6×20 in.). Figure 3.9 shows that, similar to what was observed for the stiffness, the flexural strength of the mixes with CSA cement increased with time less than the stiffness of the mixes with portland cement. In addition, while the ratio of flexural strength versus stiffness of the mixes with portland cement increased around 50% between OT and 45 days, it barely changed in the mix with CSA cement.

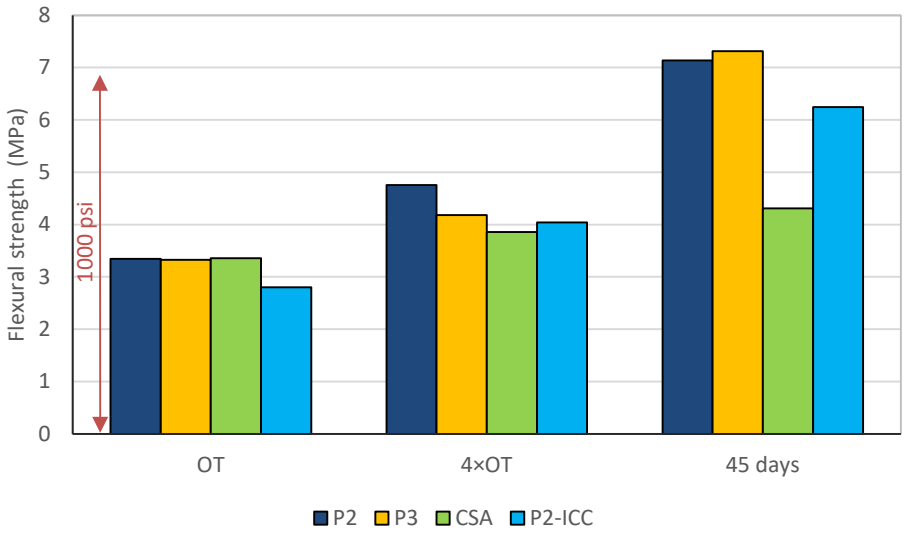

Figure 3.9: Flexural strength the lab mixes (ASTM C469).

3.5.5 Concrete Moisture-Related Shrinkage

Concrete moisture-related shrinkage was characterized following ASTM C157, except for the length of the curing period. In this standard, concrete prismatic specimens are subjected to a drying process in a room at a constant temperature of 23°C (73°F) and constant air RH of 50%. The change in the length of the specimens is measured using a length comparator or other suitable apparatus after 4, 7, 14, and 28 days, and after 8, 16, 32, and 64 weeks of drying. The change in length is used to determine the moisture-related shrinkage.

Three specimens per mix were tested. The specimens were demolded after either 4 hours (mixes with Type III or CSA cements) or 10 hours (mixes with Type II/V cement), and they were cured in a lime-saturated water bath at 23°C (73°F) until an age of three days. After the water immersion, the specimens were stored in the dry room. The specimens were 100×100×300 mm (4×4×12 in.). The results are shown in Figure 3.10, which includes the shrinkage measured in each of the three specimens and the average value of the three specimens for each of the four mixes. This figure shows that the variability between specimens of the same mix was relatively low and was definitively lower than the variability from mix to mix. In addition, the moisture-related shrinkage is much smaller in the mix with CSA cement than the mixes with portland cement. On average, the mix with CSA cement had around 30% the shrinkage of the mixes with portland cement.

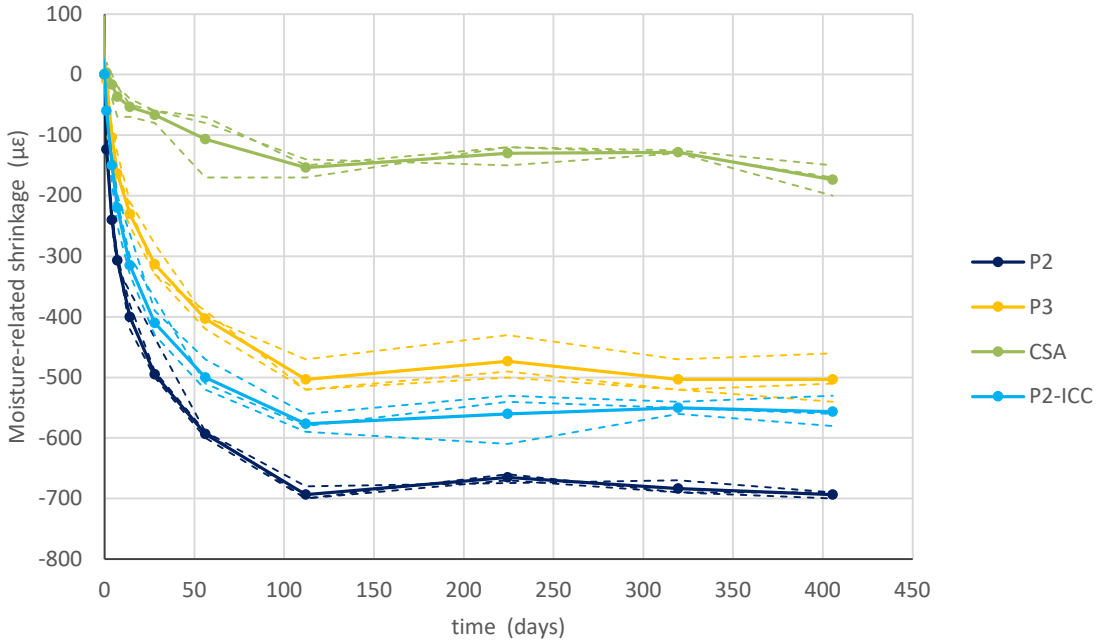

Figure 3.10: Moisture-related shrinkage of the lab mixes (ASTM C157).

3.5.6 Concrete Coefficient of Thermal Expansion

The coefficient of thermal expansion was measured following the AASHTO T 336-15 standard, which means the specimens were saturated in water before and during the test. Three specimens per mix were tested at the age of 21 days. Figure 3.11 shows that the saturated CTE of the mix with CSA cement was somewhat larger than the same variable in the mixes with portland cement.

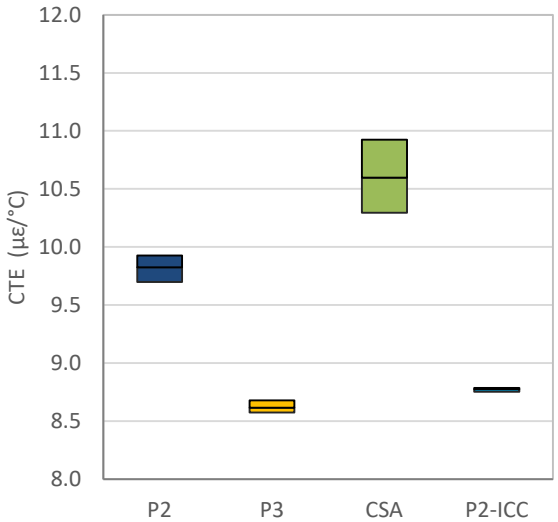

Note: Each box represents minimum, average, and maximum of the three specimens that were tested.

Figure 3.11: Coefficient of thermal expansion of lab mixes (AASHTO T 336).

3.5.7 Asphalt Laboratory Testing

The modeling presented in Chapter 7 of this report assumes the stiffness of the asphalt mixes to be a function of time of loading and temperature. Asphalt stiffness was characterized using the complex modulus determined for a range of temperatures and loading frequencies. Testing was conducted following AASHTO TP 79 with an asphalt mixture performance tester (AMPT). For that standard, a cylindrical specimen is tested in compression under sinusoidal loading. The test is conducted in load-control, and load levels are low so that the asphalt mix behaves in the linear range. The applied axial stress and the resulting axial strain are measured as a function of time, and they are used to calculate the dynamic modulus and phase angle of the mix (the dynamic modulus and phase angle constitute the complex modulus). Testing was conducted at three temperatures (10°C, 25°C, and 40°C [50°F, 77°F, and 104°F]) and frequencies from 0.01 to 25 Hz. The temperature range was selected after a series of calculations with the *CalME* temperature model *(37)*. Based on those calculations, 10°C to 40°C was the expected temperature range for an asphalt base underneath 100 to 175 mm (4 to 7 in.) thick concrete overlays in California. This predicted temperature range corresponds with the experimental data collected in the COA test track during a previous one-year period (see Section 3.6).

Two different asphalt bases existed in the COA test track (Figure 3.1). The first was an old HMA base that was built in 2012 and tested for an earlier project on full-depth reclamation. All the 6×6 ft. environmental sections were located in that area of the test track. This mix is referred to as "Old HMA" in this report. The second asphalt base was relatively new. It was built in October 2015, four months before the construction of the concrete overlay. The new asphalt base consisted of HMA, 90 mm (3.6 in.) thick, with a rubberized gap-graded overlay 30 mm (1.2 in.) thick. The two 12×12 ft. environmental sections were located in the area of the test track with the new asphalt base. The two new mixes are referred to as "New HMA" and "RHMA-G" (rubberized hot mix asphalt gap-graded) in this report. The Old HMA and New HMA were the same type of mix: a dense-graded mix with a 19 mm (3/4 in.) nominal maximum aggregate size, PG 64-16 binder, and 15% reclaimed asphalt pavement. This dense-graded mix is commonly used in California.

A major limitation of the complex modulus testing with the AMPT is that it requires relatively tall specimens that can rarely be extracted from existing pavements. In the standard approach, loose mix is used to prepare gyratory-compacted specimens that are cored and trimmed to produce 100 mm (4 in.) diameter and 150 mm (6 in.) tall cylindrical specimens. For this reason, the old asphalt mix in the test track could not be characterized with AMPT dynamic modulus testing. However, it was possible to use this testing on the two mixes in the new asphalt base. Both the New HMA and RHMA-G mixes were sampled during construction and then used in the laboratory to produce standard AMPT specimens. The air-void content (compaction level) in these laboratory specimens

matched the air-void content in the field. Dynamic modulus and Black diagrams are shown in Figure 3.12 and Figure 3.13, respectively.

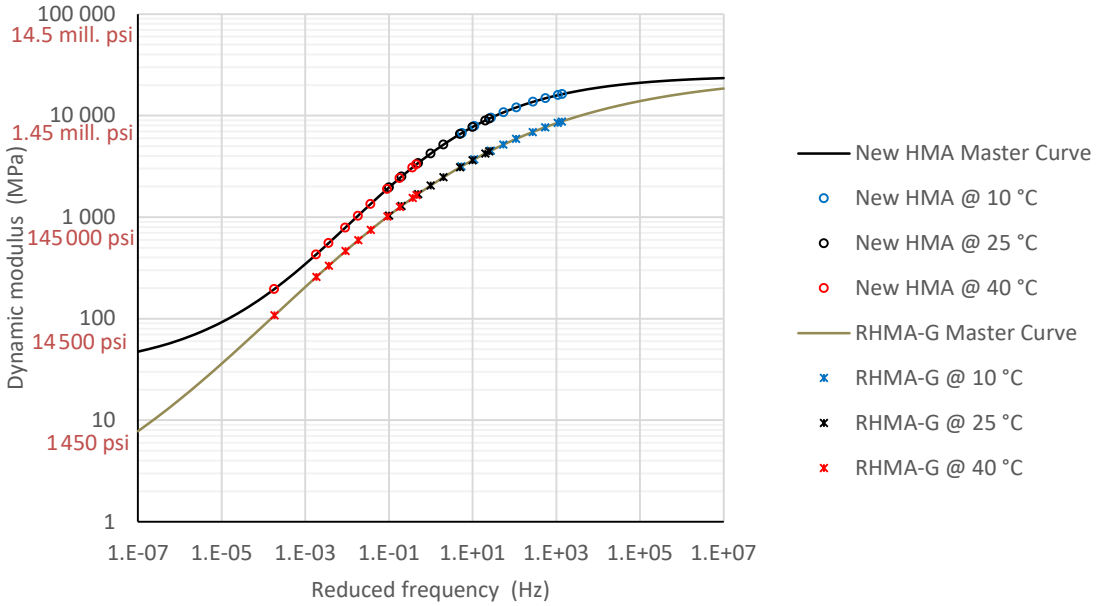

Figure 3.12: Dynamic modulus of the asphalt mixes (AASHTO TP 79).

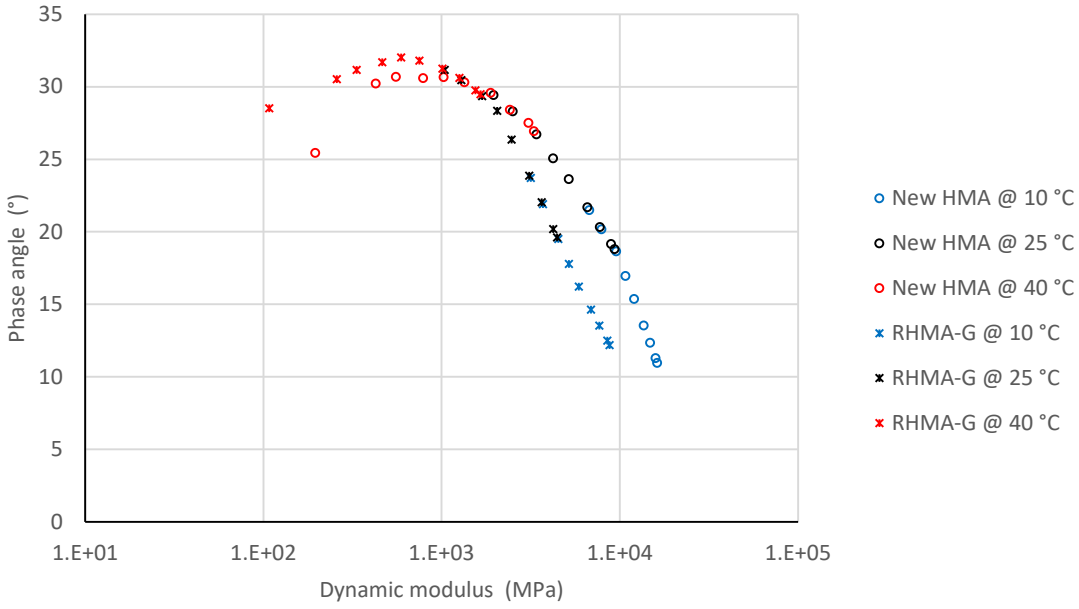

Figure 3.13: Black diagrams of the asphalt mixes (AASHTO TP 79).

3.6 Summary of Environmental Conditions During the Experiment

Environmental conditions—specifically, air temperature, air RH, rainfall, solar radiation, and wind speed—were measured by means of a weather station located near the test track. The daily mean, minimum, and maximum values of air temperature and air RH are plotted in Figure 3.14 and Figure 3.15, respectively. The data in these figures and the analysis in this report reflect the period from the construction of the overlays in February 2016 to May 31, 2017.

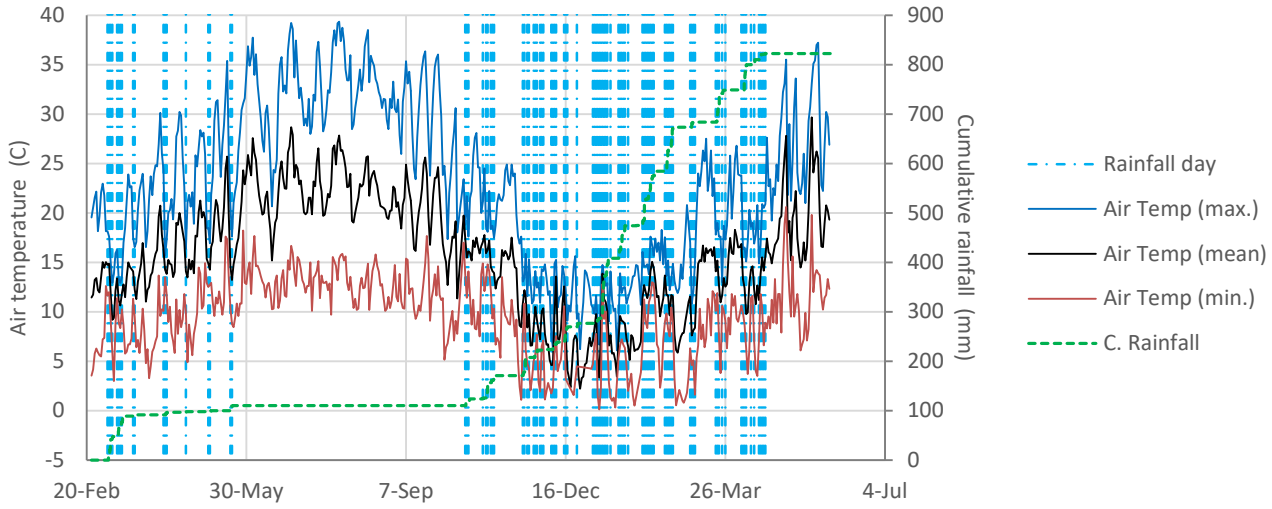

Notes: Temperature data in this figure are the daily means, daily minimums, and daily maximums. The series "Rainfall day" shows days when rainfall occurred.

Figure 3.14: Air temperature and rainfall during the analysis period.

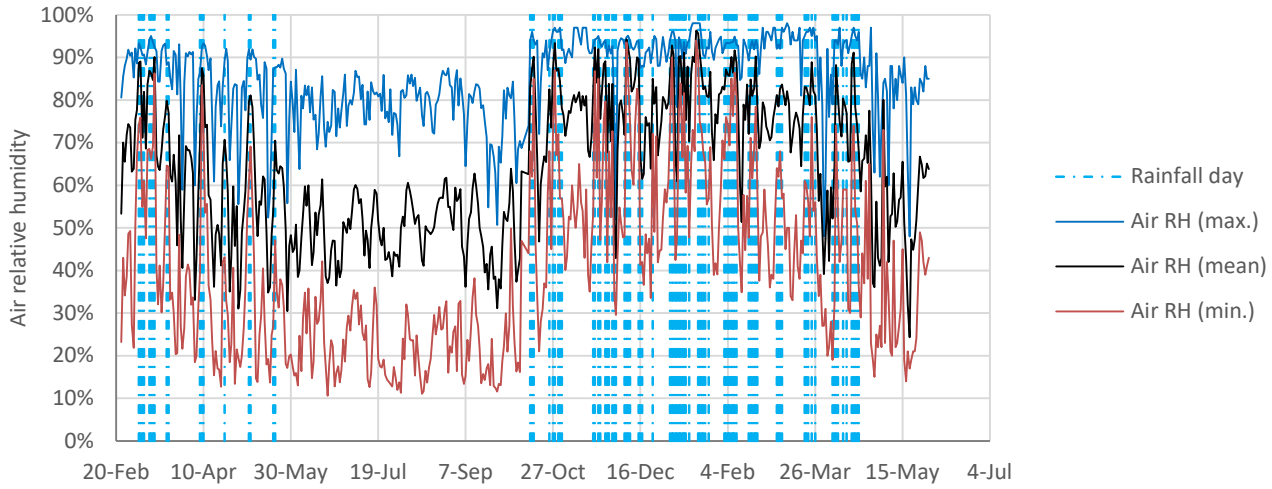

Notes: RH data in this figure are the daily means, daily minimums, and daily maximums. The series "Rainfall day" shows days when rainfall occurred.

Figure 3.15: Air relative humidity during the analysis period.

A previous UCPRC report *(4)* includes a preliminary analysis of the temperatures measured in the COA slabs over the course of one year. Some mix-to-mix differences, related to differences in the albedo of the mixes, were observed in that preliminary analysis. More specifically, the mixes with Type II/V portland cement (P2 and P2-ICC) had lower albedo—that is, a lower capacity to reflect solar radiation—than the mixes with Type III and CSA cements (P3 and CSA). The measured albedos were 0.32, 0.38, and 0.44 for the mixes with Type II/V portland, Type III portland, and CSA cements, respectively. As a result, the P2 and P2-ICC mixes had higher maximum concrete temperatures and higher daytime ELTD than the P3 and CSA mixes.

Figure 3.16 shows the cumulative distributions of three temperature-related variables: temperature measured with the shallowest thermocouple (T005, measured at 5 mm [0.2 in.] depth), mean slab temperature (TPCC), and asphalt temperature (TAC). In the three cases, the values shown are the average of all the environmental sections during a one-year period, from February 26, 2016, to February 26, 2017. The frequency distribution of the ELTD is shown in Figure 3.17. Again, the values shown are the average of all the environmental sections during a one-year period. The values in Figure 3.16 and Figure 3.17 can be considered estimates of the temperatures that a 115 mm (4.5 in.) thick COA slab will be subjected to in California's Inland Valley[4] climate region.

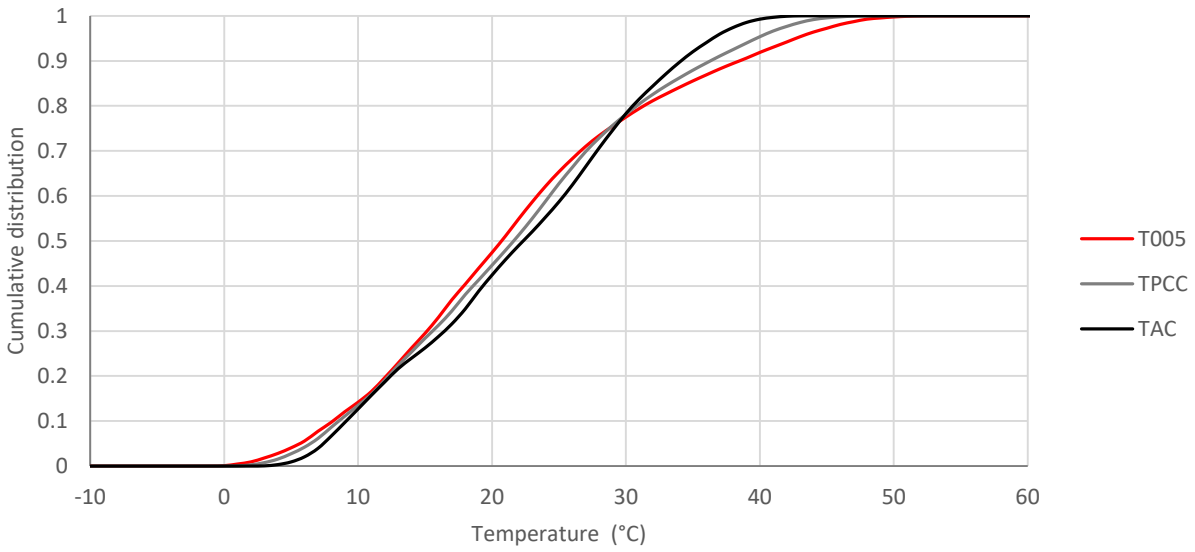

Notes: T005 is the temperature measured with the shallowest thermocouple (5 mm [0.2 in.] depth). TPCC is the mean slab temperature. TAC is the asphalt temperature (measured 30 mm [1.2 in.]) below the slab's bottom.

Figure 3.16: Temperature distribution over a one-year period (Feb. 26, 2016, to Feb. 26, 2017, mean all ENV sections).

[4] The Caltrans pavement climate regions map is available online *(38)*.

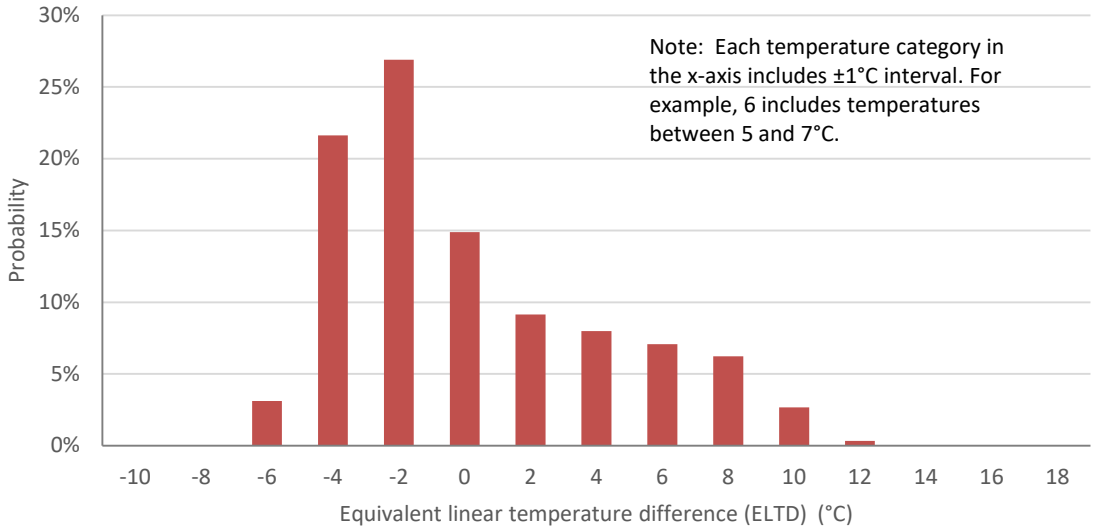

Figure 3.17: Frequency distribution of the ELTD over a one-year period (Feb. 26, 2016, to Feb. 26, 2017, mean all ENV sections).

3.7 Sign Conventions Used in This Report

This report uses the following conventions for referring to strain: a positive value (+) indicates an expansion and a negative value (-) indicates a contraction. This report also uses the following conventions for referring to vertical displacements: a positive value (+) indicates upward vertical movement and a negative value (-) indicates downward vertical movement. This convention applies to the JDMDs that measure the vertical displacements of slab corners and edges. For the horizontal JDMDs that measure joint opening and closing, a positive value (+) indicates joint opening and a negative value (-) indicates joint closing.

4 QUANTIFICATION OF SHRINKAGE IN THE CONCRETE OVERLAY ON ASPHALT SLABS

4.1 Preliminary Conclusions Based on Vibrating Wire Strain Gauges Data

The models presented in Section 3.4 were used to analyze the strain data collected by the VWSGs in the unrestrained shrinkage prisms and in the COA slabs. Using the results of that analysis, the moisture-related shrinkage at constant temperature ($\varepsilon_{Sh,T0}$) was backcalculated for the unrestrained shrinkage prisms, and values for the mean and differential moisture-related shrinkage at constant temperature ($\varepsilon_{MEAN,Sh,T0}$ and $\varepsilon_{DIFF,Sh,T0}$) were backcalculated for the COA slabs. As explained in Section 3.4, $\varepsilon_{MEAN,Sh,T0}$ represents the average shrinkage through the thickness of the slab and $\varepsilon_{DIFF,Sh,T0}$ represents the difference between shrinkage at the top and bottom of the slab. These shrinkage estimates are shown in Figure 4.1 ($\varepsilon_{Sh,T0}$), Figure 4.2 ($\varepsilon_{MEAN,Sh,T0}$), and Figure 4.3 ($\varepsilon_{DIFF,Sh,T0}$).

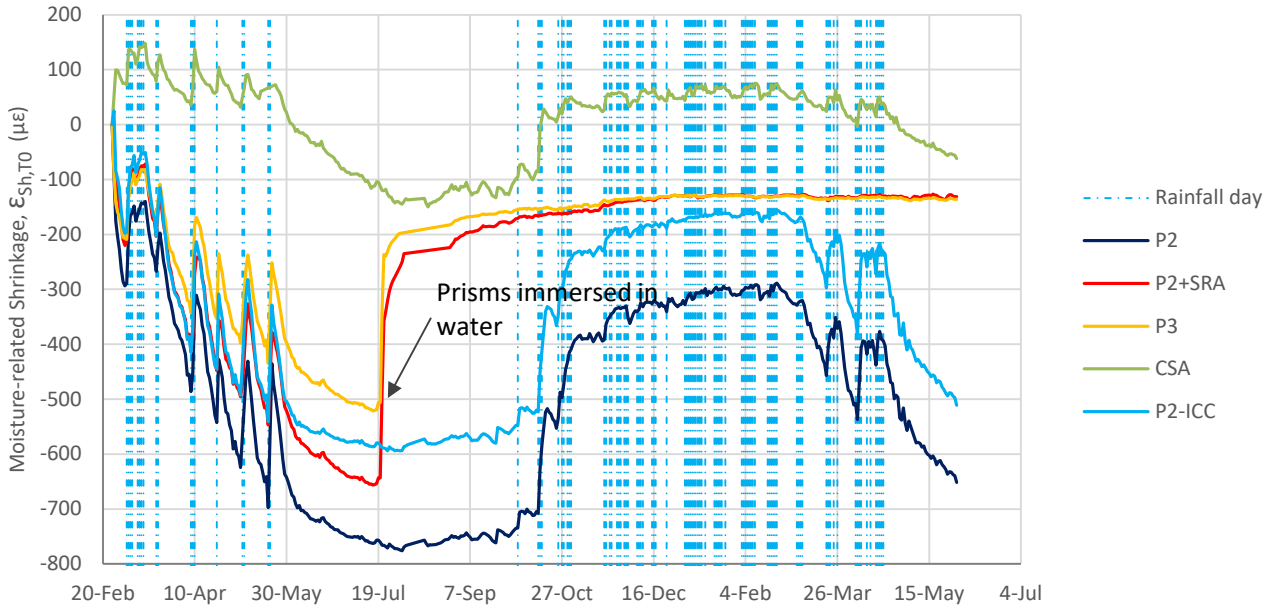

Note: The mix "P2+SRA" is the mix P2 cured with shrinkage-reducing admixture (SRA) before the curing compound application.

Figure 4.1: Moisture-related shrinkage in the unrestrained shrinkage prisms ($\varepsilon_{Sh,T0}$).

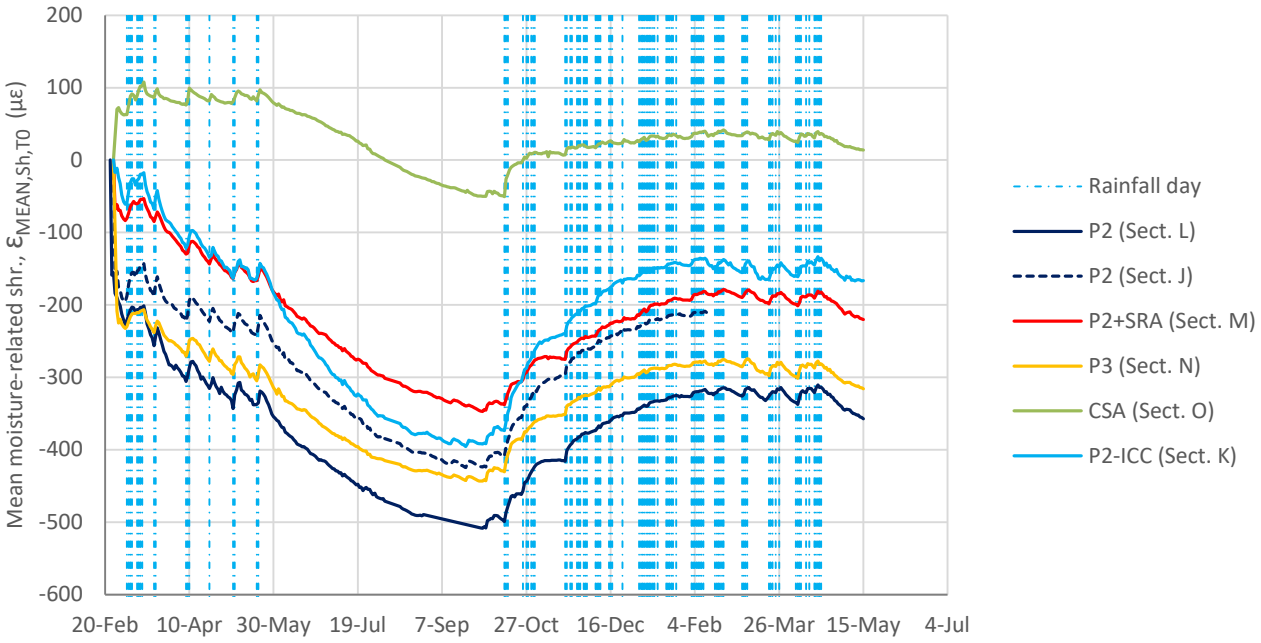

Notes: The plot reflects the average measurements of all pairs of strain gauges for each section. The mix "P2+SRA" is the mix P2 cured with shrinkage-reducing admixture (SRA) before the curing compound application.

Figure 4.2: Mean moisture-related shrinkage in the COA slabs ($\varepsilon_{MEAN,Sh,T0}$).

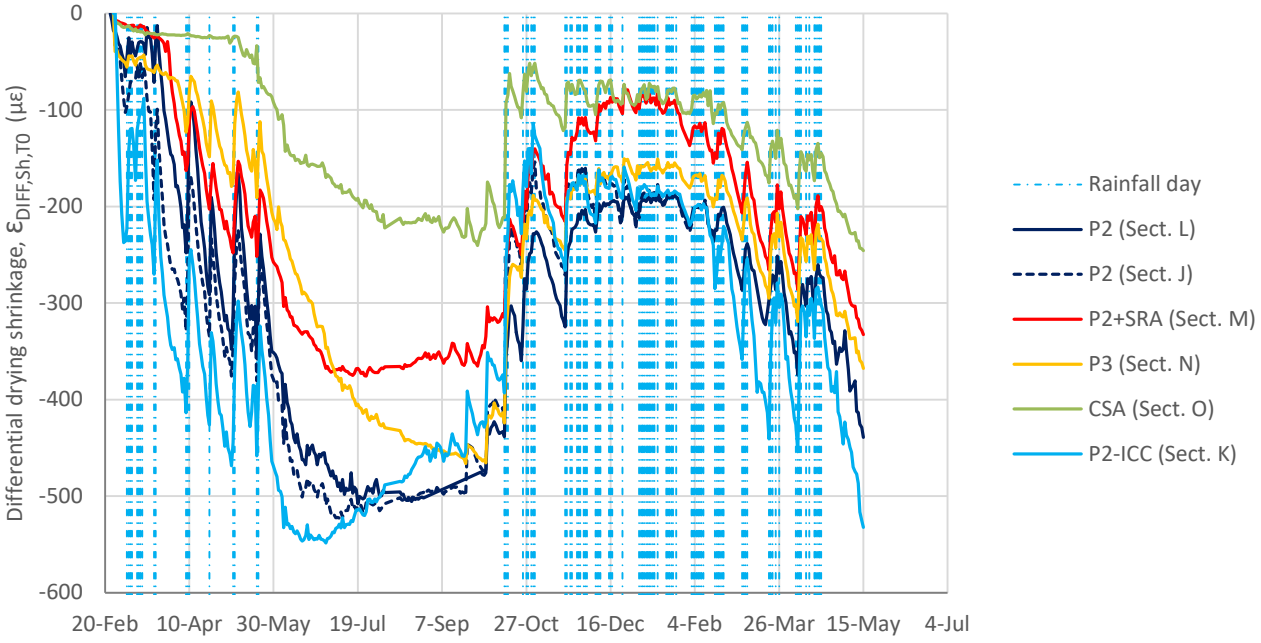

Notes: The plot reflects the average measurements of all pairs of longitudinal strain gauges located at the corners of each section. The mix "P2+SRA" is the mix P2 cured with shrinkage-reducing admixture (SRA) before the curing compound application.

Figure 4.3: Differential drying shrinkage in the COA slabs at the corners ($\varepsilon_{DIFF,Sh,T0}$).

For each section, the mean shrinkage shown in Figure 4.2 is the average measured by all the pairs of strain gauges in the section. That average can be considered an estimate of the unrestrained contraction of the slabs because under the slow action of shrinkage the stiffness of the asphalt is much less than the stiffness of the concrete, allowing the slabs to freely expand and contract with almost no restriction from the asphalt base. The similarity between the mean shrinkage ($\varepsilon_{MEAN,Sh,T0}$) results obtained from the pairs of strain gauges located at the center of the slabs and the pairs located at the corners (see the example in Figure 4.4 of Section L) is proof of the low stiffness of the asphalt. The low stiffness of the asphalt under the shrinkage action is discussed further in Section 7.4.

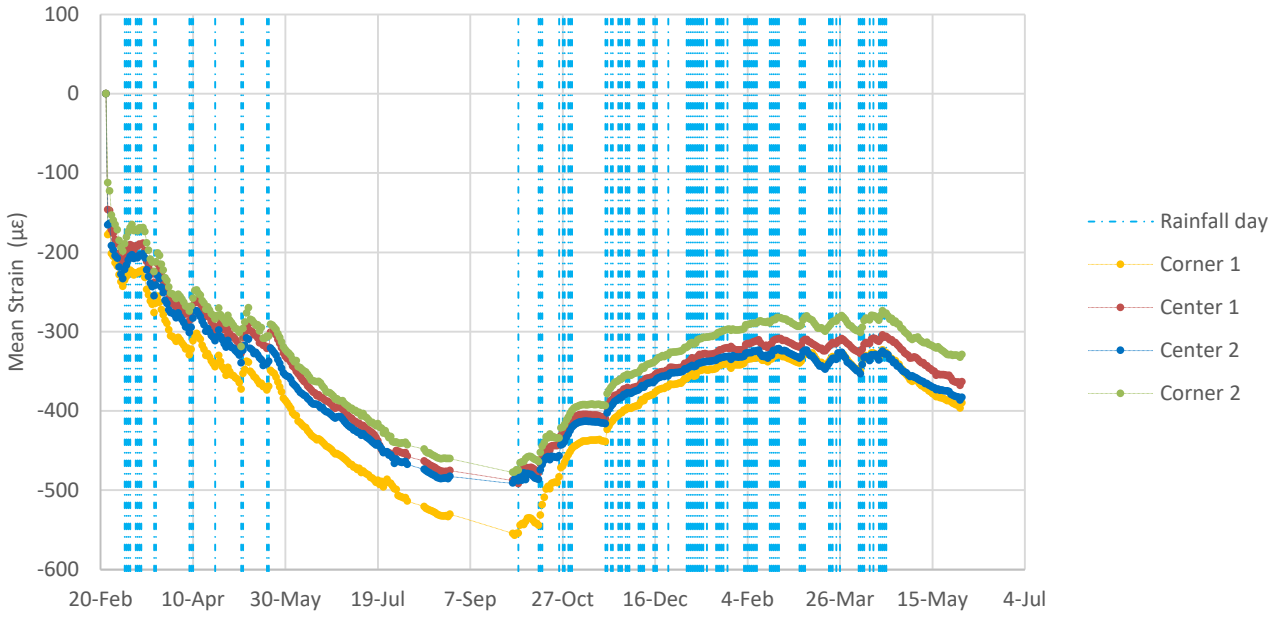

Figure 4.4: Comparison between mean moisture-related shrinkage at corner and center of the slabs, Section L.

The differential drying shrinkage for each of the sections shown in Figure 4.3 ($\varepsilon_{DIFF,Sh,T0}$) is the average obtained from the pairs of strain gauges located at the corners of the slabs. That average can be considered an estimate of the unrestrained bending of the slabs. Only measurements from the pairs of strain gauges located at the corners were used for this analysis because bending at the center of the slab is more restricted than at the corners. The pairs of corner strain gauges were located just 250 mm (10 in.) from the transverse joints. Because the gauges were so close to the joints and because of the low the stiffness of the asphalt under the shrinkage action, the slabs were almost free to rotate at that location after the transverse joints were deployed. For this reason, these pairs of strain gauges—and not those located at the center of the slabs—were deemed the most suitable for estimating the unrestrained bending of the COA slabs.

Based on the shrinkage estimations in Figure 4.1, Figure 4.2, and Figure 4.3, a series of preliminary conclusions can be drawn:

- Very high levels of differential drying shrinkage (top to bottom of the slab), with values as high as 450 to 550 με, were backcalculated for all the sections with portland cement mixes, except for Section M where the mix was treated with SRA before the curing compound application (all other sections were cured with the curing compound only).
- Around 200 to 250 με of autogenous shrinkage were backcalculated in the mixes P2 (Type II/V cement) and P3 (Type III cement), which had water/cement ratios of 0.33 and 0.31, respectively. No autogenous shrinkage was measured in the P2-ICC mix due to the internal curing provided by the prewetted lightweight aggregates, and no autogenous shrinkage occurred in the CSA mix, which actually expanded slightly after setting.
- Rainfall events produced an almost immediate decrease in the magnitude of the differential drying shrinkage in the COA slabs, except when the concrete was already saturated. The immediacy of the response to rainfall occurred with both the portland cement and CSA mixes.

4.2 Maximum Shrinkage in the Concrete Slabs

Moisture-related shrinkage (in absolute value) was expected to be greatest at the top surface of the slabs since drying mainly starts at the top and progresses downward. The shrinkage at the top of the slabs can be estimated by adding half of the differential drying shrinkage (Figure 4.3, $\varepsilon_{DIFF,Sh,T0}$) to the mean moisture-related shrinkage (Figure 4.2, $\varepsilon_{MEAN,Sh,T0}$). Figure 4.5 shows the results of that calculation. The shrinkage at the top of the slabs increased in all the sections during the summer of 2016 (June through September), although the shrinkage seemed to flatten by the time the rainfall season began in October. The maximum values are shown for each of the sections in Table 4.1. For four of the six mixes, the consistency between the peak shrinkage at the top of the slabs and the peak shrinkage in the unrestrained shrinkage prisms is strong. The exceptions are Section M and Section N, with mixes P2+SRA and P3, respectively. The P3 prism was immersed in water before the shrinkage peak was reached, which may explain the differences shown in Table 4.1. The P2+SRA prism was also immersed in water before the peak shrinkage was reached, but the shrinkage value in the prism is much higher (absolute value) than in the COA slabs. As explained in a previous UCPRC report *(4)*, the SRA treatment seemed to produce a much bigger effect in the COA slabs than in the unrestrained shrinkage prisms. An interesting observation for the P2, CSA, and P2-ICC mixes is that the peak shrinkage values were similar in the prisms and slabs, but those values were reached in the prisms earlier than in the slabs.

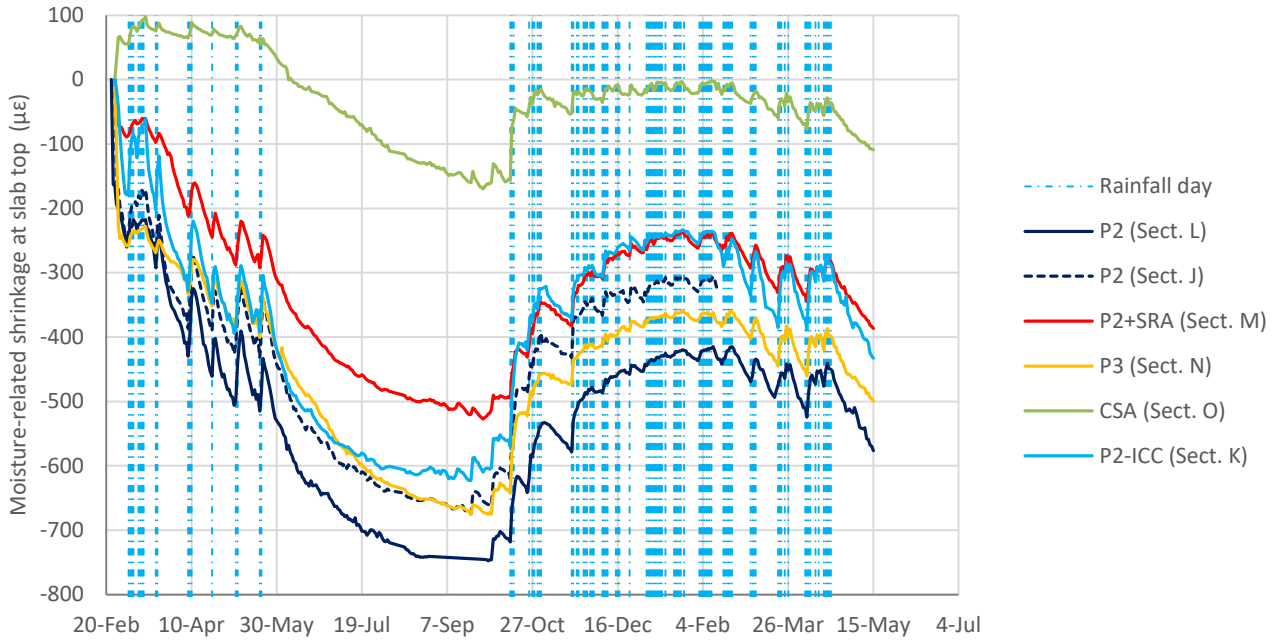

Notes: The plot reflects the average values measured by the pairs of longitudinal strain gauges at the corners for each section. The mix "P2+SRA" is the mix P2 cured with shrinkage-reducing admixture (SRA) before the curing compound application.

Figure 4.5: Moisture-related shrinkage at the top of the COA slabs (at the corners).

Table 4.1: Maximum Field Shrinkage (με)

Mix/Section	Field Unrestrained Shrinkage Prisms	COA Slabs (corners, top)
P2 / Sect. J	-776	-747
P2 / Sect. L		-675
P2+SRA / Sect. M	-656[a]	-527
P3 / Sect. N	-521[a]	-675
CSA / Sect. O	-150	-170
P2-ICC / Sect. K	-594	-623

[a] Prisms were immersed in water before the peak shrinkage was reached. For these mixes, the value in the table is the shrinkage before the immersion.

It should be noted that the comparison of shrinkage in the prisms versus shrinkage in the slabs is not straightforward. Drying in the slabs was expected to be less than in the prisms because the ratio of volume to exposed surface is higher in the slabs than in the prisms. In addition, drying in the prisms was expected to be relatively uniform because they are not very thick (40 mm [1.6 in.]). Consequently, the backcalculated moisture-related shrinkage can be considered an estimate of the unrestrained shrinkage of the concrete for the average moisture conditions of the prism. However, the same does not apply to the concrete slabs. In the slabs, the

measured (backcalculated) shrinkage will typically be different than the unrestrained shrinkage, the shrinkage profile that would exist if the concrete was fully free to contract (i.e., if it were not subjected to any stress). At the corners, the slabs are free to rotate after the transverse joints are deployed. Under such conditions, the backcalculated moisture-related shrinkage profile can be assumed to be a function of—but not necessarily the same as—the unrestrained shrinkage profile in the slabs.

Figure 4.6 is an example illustrating the difference between unrestrained shrinkage (the action) and shrinkage in the slab (the reaction). In this example, a 115 mm (4.5 in.) thick slab is subjected to shrinkage action (unrestrained shrinkage) that reaches -100 με at the surface and decreases linearly until reaching zero at a depth of 25 mm (1 in.). The slab contracts and bends upward as a result of this action, but the strain at the top of the slab is only -39 με, roughly 40% of the unrestrained shrinkage at the slab surface. This example shows, first, that the unrestrained shrinkage at the top of the slab cannot be backcalculated without making some assumptions about the unrestrained shrinkage profile and, second, that the shrinkage strain at the top of the slab is a lower bound estimation of the unrestrained shrinkage at the same location. The two values would match if the unrestrained shrinkage decreased linearly between slab surface and slab bottom.

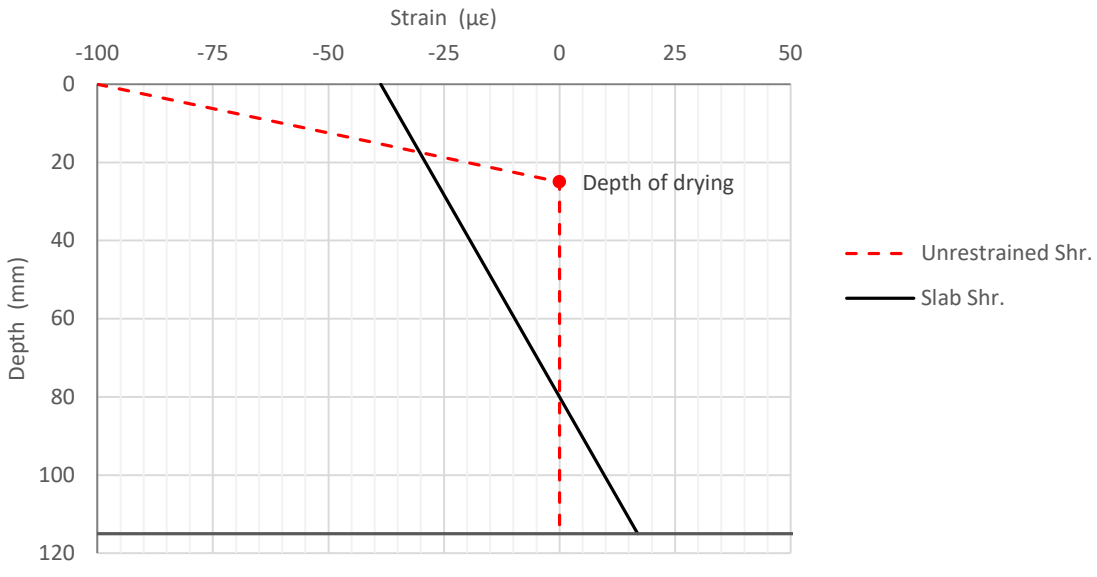

Figure 4.6: Example of the difference between unrestrained shrinkage and slab shrinkage.

4.3 Depth of Drying Shrinkage in the Concrete Slabs

The differential drying shrinkage (Figure 4.3, $\varepsilon_{DIFF,Sh,T0}$) in the sections with Type II/V cement (Sections J, K, L, and M) reached a maximum during the summer of 2016, mostly in June and July, depending on the type of mix. After the maximum, $\varepsilon_{DIFF,Sh,T0}$ decreased in all these sections even though drying continued for a few more months, as evidenced by the air RH measured with sensors located at a depth of 20 mm (0.8 in.) in the concrete

(Figure 4.7). The drying was also evidenced by the mean moisture-related shrinkage in the slabs (Figure 4.2, $\varepsilon_{MEAN,Sh,T0}$), which continuously increased (in absolute value) until the rainfall season started in October. This pattern indicates that drying was affecting the bottom half of the slabs. Something similar occurred in Section N and Section O, which had Type III and CSA cements, respectively. In these two sections, $\varepsilon_{DIFF,Sh,T0}$ flattened in September, although the RH sensors indicated that drying continued.

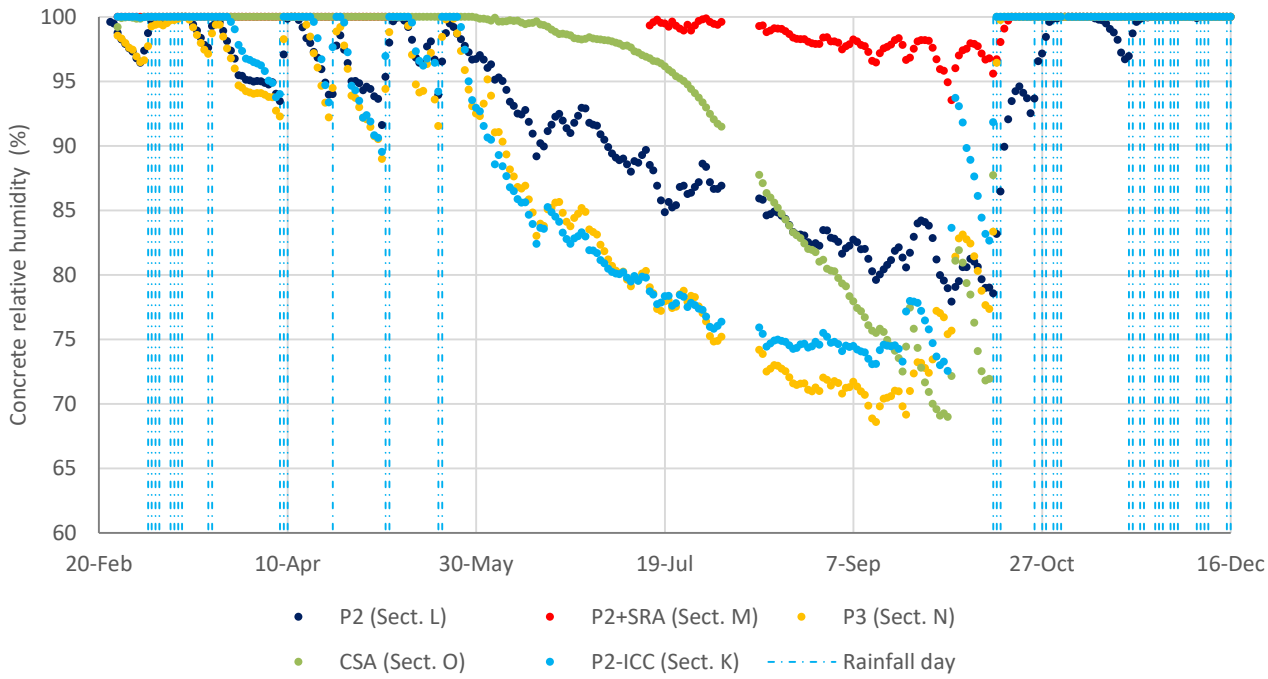

Notes: Each point in the graph is the mean value of RH values measured in one day. The mix "P2+SRA" is the mix P2 cured with shrinkage-reducing admixture (SRA) before the curing compound application. The RH sensors started malfunctioning in January 2017, around 10 months after the installation.

Figure 4.7: Relative humidity measured by RHC sensors at the slab center at depth of 20 mm (0.8 in.).

The depth of the slab affected by drying shrinkage is a modeling parameter in ME design procedures (at least in those procedures that account for moisture-related shrinkage) for concrete pavements like the *MEPDG (1,8)* and the first release of *HIPERPAV (25)*. The *MEPDG* assumes that drying shrinkage reaches a depth of 50 mm (2 in.), while *HIPERPAV* assumes it reaches a half-depth of the slab. In both cases, the depth of drying is kept fixed in time while the unrestrained shrinkage (shrinkage action) at the top of the slab is varied in time as a function of time and air RH (Figure 4.8 a). According to this approach, the ratio between mean and differential shrinkage in the slabs ($\varepsilon_{MEAN,Sh,T0}/\varepsilon_{DIFF,Sh,T0}$) should be a constant, which is not what happened in the COA slabs. It is very likely that the pattern of shrinkage evolution was more similar to the "alternative approach," shown in Figure 4.8 (b). In the alternative approach, the unrestrained shrinkage at the top of the slab is kept constant while the depth affected

by shrinkage and—to a lesser extent and depending on slab thickness—the shrinkage at the bottom of the slab increases.

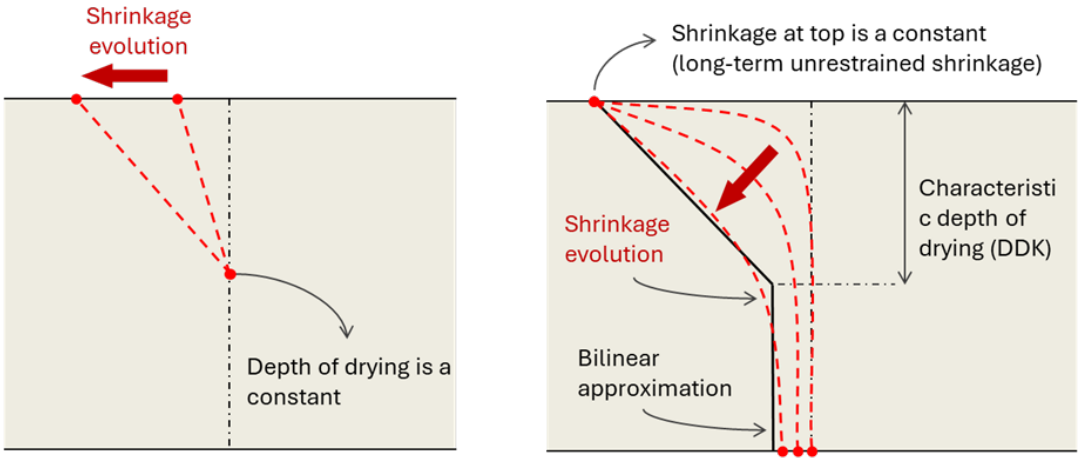

(a) *MEPDG* and *HIPERPAV* approach (b) Alternative approach

Figure 4.8: Unrestrained drying shrinkage profile in the slabs.

As previously discussed, the alternative approach in Figure 4.8(b) assumes that the unrestrained shrinkage at the top of the slabs is a constant, the long-term unrestrained shrinkage of the concrete. This assumption is based on the fact that drying takes place very rapidly in the top few millimeters of the slabs. The first drawback of this approach is that the long-term unrestrained shrinkage of the concrete depends on the RH of the air. As a result, the unrestrained shrinkage at the top of the slab changes with the RH of the air. The second drawback of the approach is it cannot reproduce the shrinkage profile after rainfalls, which produce top-down wetting of the slabs. Under such conditions, the unrestrained shrinkage profile will bend toward zero at the slab surface. Even with these limitations, the alternative shrinkage profile seems much more realistic than the standard hypothesis currently used in the ME design of concrete pavements. For this reason, the alternative approach was used in this study to predict the depth of drying in the COA slabs, as explained in the following discussion.

The bilinear approximation of the alternative shrinkage profile in Figure 4.8(b) has three parameters: unrestrained shrinkage at the slab top (ε_{TOP}), characteristic depth of drying (DDK), and unrestrained shrinkage at the slab bottom ($\varepsilon 1$). Such a profile would result in the mean and the differential shrinkage shown in Equation 4.1 and Equation 4.2, respectively, provided that the slab is free to rotate and contract without restriction. By using these equations, two parameters of the shrinkage profile are functions of $\varepsilon_{MEAN,Sh,T0}$ and $\varepsilon_{DIFF,Sh,T0}$, if the third parameter is assumed. In this study, ε_{TOP} was assumed and then $\varepsilon_{MEAN,Sh,T0}$ and $\varepsilon_{DIFF,Sh,T0}$ (the latter obtained for the corner strain gauges) were used to backcalculate $\varepsilon 1$ and DDK. ε_{TOP} was assumed to be the maximum moisture-related shrinkage backcalculated in the unrestrained shrinkage prisms, shown in Table 4.1. This analysis could not be

conducted for Section M (P2+SRA) and Section N (P3) since the corresponding prisms were immersed in water before the peak shrinkage was reached. For the other sections, the backcalculated characteristic depth of drying is shown in Figure 4.9, and the unrestrained shrinkage at the slab bottom ($\varepsilon 1$) is shown in Figure 4.10. For each of the sections, the figures show only data after the joints were fully deployed.

$$\varepsilon_{MEAN,Sh,T0} = \varepsilon 1 + \frac{1}{2} \cdot (\varepsilon_{TOP} - \varepsilon 1) \cdot r \quad \textbf{(4.1)}$$

$$\varepsilon_{DIFF,Sh,T0} = 6 \cdot (\varepsilon_{TOP} - \varepsilon 1) \cdot r \cdot \left(\frac{1}{2} - \frac{r}{3}\right) \quad \textbf{(4.2)}$$

where: r relative characteristic depth of drying, DDK/slab thickness
ε_{TOP} unrestrained shrinkage at the slab top
$\varepsilon 1$ unrestrained shrinkage at the slab bottom

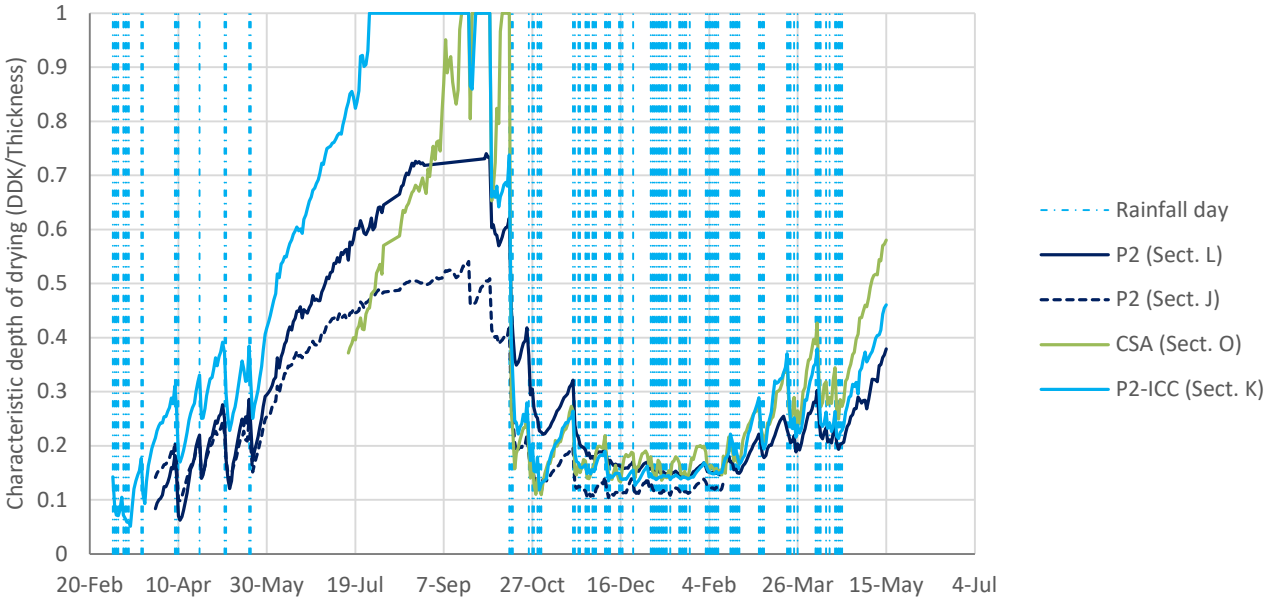

Note: Data are shown, for each section, after the joints were fully deployed.

Figure 4.9: Characteristic depth of drying (DDK).

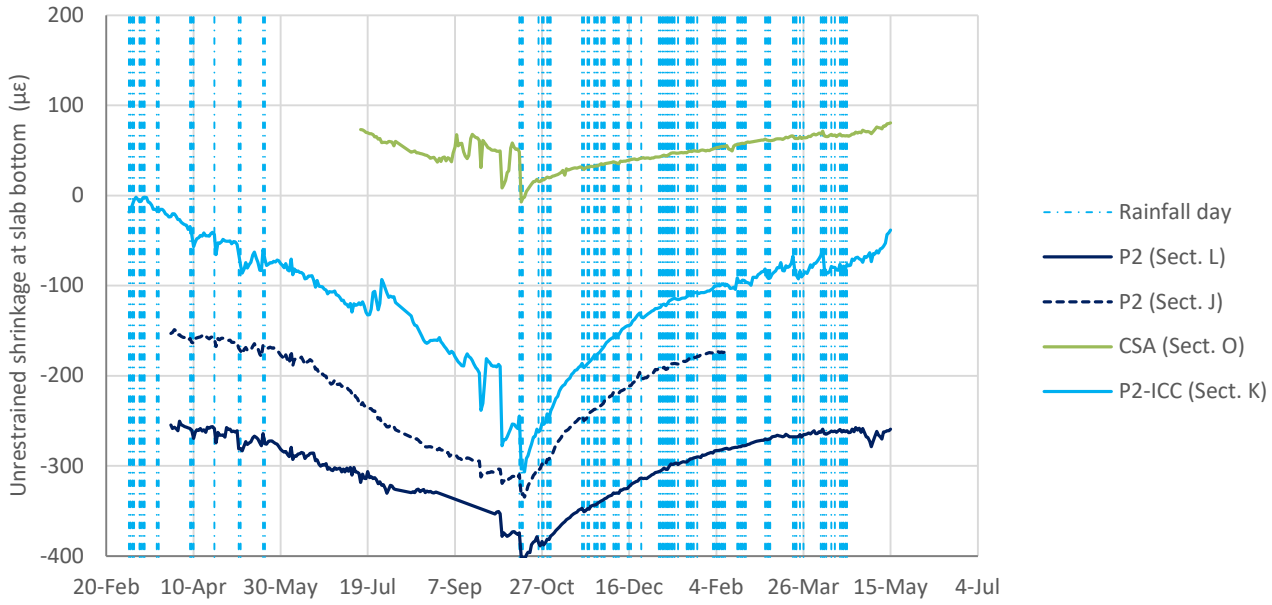

Note: Data are shown, for each section, after the joints were fully deployed.

Figure 4.10: Unrestrained shrinkage at the slab bottom (*ε1*).

Figure 4.9 and Figure 4.10 show that drying considerably affected the bottom half of the slabs with the P2, CSA, and P2-ICC mixes. This finding contradicts the standard hypothesis currently used in the ME design of concrete pavements that drying shrinkage does not occur below 50 mm (*MEPDG*) or half the thickness of the slab (*HIPERPAV*). The standard hypothesis is also contradicted by moisture content measurements near the middle of the slabs at 50 mm (2 in.) depth. As shown in Figure 4.11, the moisture content measured at that depth decreased in all sections during the summer of 2016.

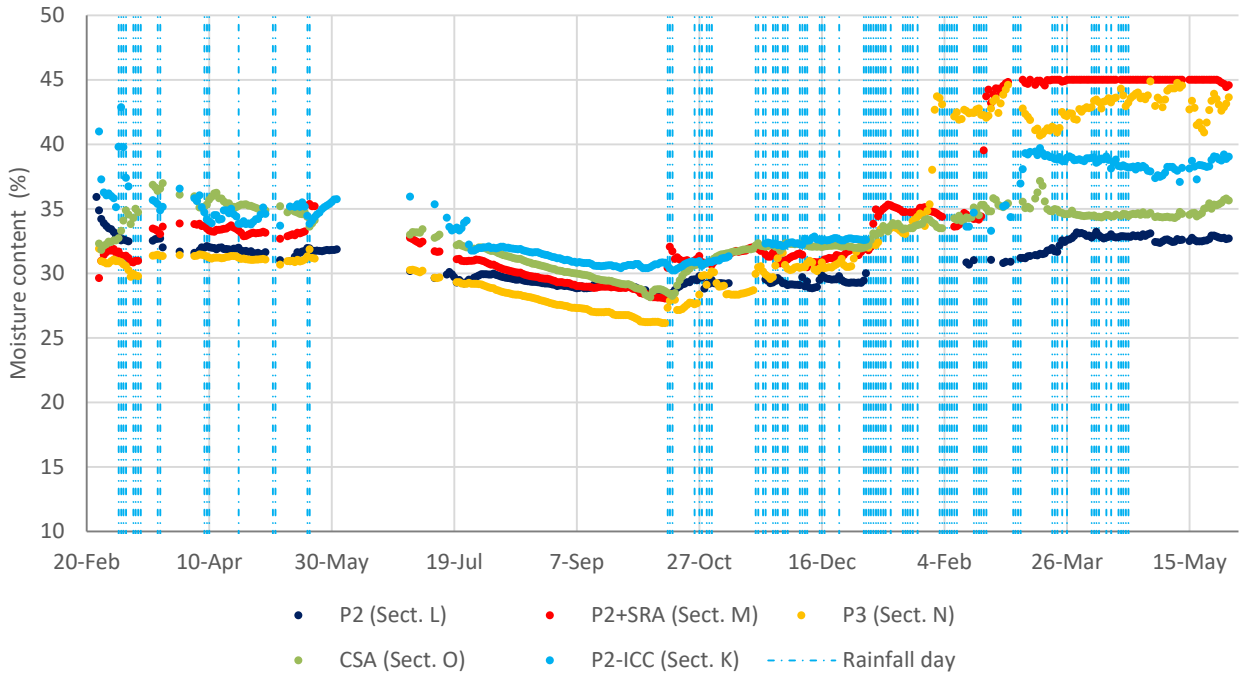

Notes: Each point in the graph is the average of moisture content (MC) values measured in one day. The sensors do not measure MC in the concrete; they measure in the wood in which the sensor is embedded. This yields an indirect measure of concrete MC. The mix "P2+SRA" is the mix P2 cured with shrinkage-reducing admixture before the curing compound application.

Figure 4.11: Moisture content at 50 mm (2.0 in.) depth.

An interesting observation from Figure 4.10 is that the unrestrained shrinkage at the bottom of the slabs with the P2 mix was around 200 με a few days after construction. This strain is very likely the autogenous shrinkage in this mix, which has a relatively low water/cement ratio (0.33). The higher autogenous shrinkage in Section L compared with Section J was discussed in a previous UCPRC report *(4)*, and it was attributed to a higher water content of the mix in Section J compared with Section L. The unrestrained shrinkage at the bottom of the slabs with P2-ICC mix was around zero after the construction. This indicates that internal curing was effective in reducing the autogenous shrinkage that barely occurred in that mix.

5 EVALUATION OF SHRINKAGE PREDICTION MODELS

This chapter includes an evaluation of three shrinkage prediction models: B3 *(7)*, B4 *(9)*, and ACI 209R-92 *(6)*. The B3 and ACI 209R-92 models are not applicable to concrete with admixtures, such as the mixes used in the COA environmental sections. Still, evaluation of these models for these mixes was considered an interesting exercise. One reason is that the shrinkage prediction equations used in the *MEPDG* are based on these two models. The B4 model is applicable to mixes with admixtures, although its authors warn users about the difficulty of shrinkage prediction when multiple admixtures are used in the mix—as is the case with the mixes used in the COA environmental sections—due to potential interactions among them *(9)*. These three models cannot account for the internal curing provided by lightweight aggregates, so no attempt was made to predict shrinkage in the P2-ICC mix. The same applies to the CSA mix, since none of these models considers CSA cement.

The three shrinkage prediction models have a similar format, where shrinkage is the result of multiplying the ultimate shrinkage, $\varepsilon_{Sh\infty}$, by a series of factors. One factor accounts for air RH, and another factor is a time function. The three models assume that specimen size does not affect the ultimate shrinkage but that it does affect the speed of shrinkage development. Consequently, specimen size is accounted for in the parameters of the time function. The ACI model includes mix properties in a series of correction factors that multiply the default ultimate shrinkage (780 με). The B3 and B4 models use the properties of the mix in their estimations of the ultimate shrinkage. A more detailed description of each of these models can be found in previous research *(6,7,9)*.

The models were evaluated using laboratory data. As explained in Section 3.5.1, concrete moisture-related shrinkage was measured in the laboratory following ASTM C157, except for the length of the water immersion period prior to the dry exposure. After the immersion period, the concrete prisms were subjected to a drying process in a room at a constant temperature of 23°C (73°F) and a constant air RH of 50%. It should be noted that the B3 and B4 models indirectly account for the length of the water immersion period, based on the stiffness of the concrete when the drying process begins.

A comparison between measured and predicted shrinkage is shown in Figure 5.1 (for mix P2) and Figure 5.2 (for mix P3). The B3 and B4 models considerably underestimated shrinkage in the two mixes. An interesting outcome is that the B4 model did not improve upon the predictions of the B3 model. One reason is that the B4 model failed to predict the autogenous shrinkage in the two mixes. For Type II/V cement, B4 assumes null autogenous shrinkage while for Type III cement it assumes a slight expansion.[5] These assumptions do not agree with the

[5] The B4 model uses the cement types in the CEB-FIP Model Code, but the model's authors recommend using SL (slow-hardening class) for cement Type II and RS (rapid-hardening class) for cement Type III.

experimental data from this research project, since both the P2 and P3 mixes experienced considerable autogenous shrinkage *(4)*. Overall, the ACI shrinkage predictions were not far from the shrinkage measured in the laboratory, even though this model was not developed for mixes with admixtures.

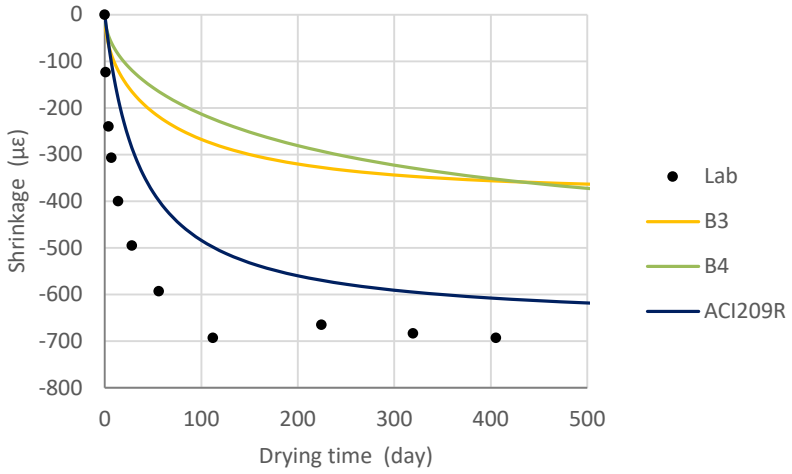

Figure 5.1: Evaluation of shrinkage prediction models (P2 mix).

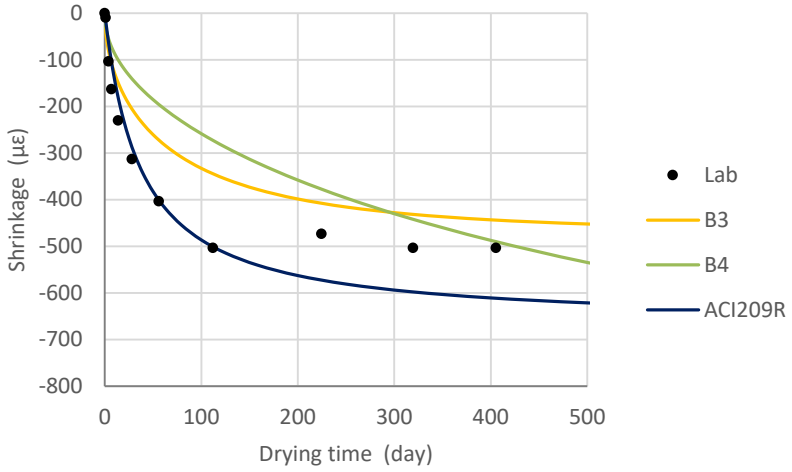

Figure 5.2: Evaluation of shrinkage prediction models (P3 mix).

6 RELATIONSHIP BETWEEN LAB AND FIELD SHRINKAGE

This chapter focuses on the third question called out in the introduction: *What is the relationship between laboratory and field shrinkage?* Unfortunately, the comparison of laboratory shrinkage versus field shrinkage was not straightforward for several reasons. The following are the reasons believed to be the most important:

- *Effects of curing time.* The laboratory prisms were immersed in water until they reached an age of three days, after which they were removed from the water and allowed to dry. However, drying began much earlier in the field prisms and slabs because the curing compound spray is not as effective as water immersion in preventing the concrete from drying. This difference is important since it means the concrete in the lab prisms was more mature than the concrete in the field when the drying process began.
- *Effects of size.* The ratio between the volume of concrete and the exposed surface (V/S) in the lab shrinkage prisms was different from the V/S ratio in the field prisms and the COA slabs. This difference is important since the speed of shrinkage evolution depends on this ratio.
- *Constant versus variable ambient conditions.* Concrete temperature and air RH were constant in the laboratory drying process (23°C and 50% RH in this study), while they changed daily and seasonally in the field. Since shrinkage is dependent on concrete temperature and air RH, a direct comparison between lab and field shrinkage would not be realistic. Although the different shrinkage prediction models include air RH correction factors, these factors were conceived not to predict changes in shrinkage due to changes in air RH but to determine shrinkage under an arbitrary yet constant air RH, shown in Figure 6.1.

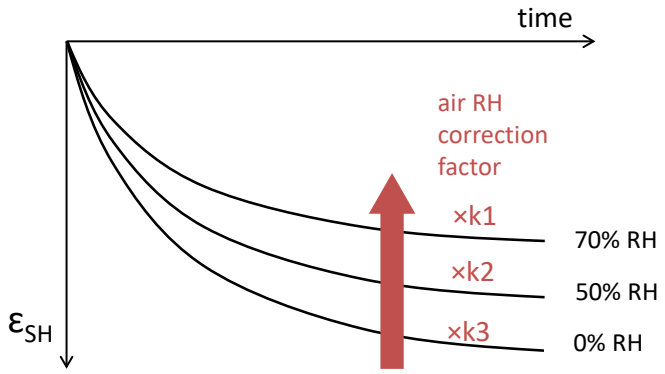

Figure 6.1: Air RH correction in shrinkage prediction models (B4 model).

- *Dry and wetting versus monotonic drying.* Concrete dried monotonically in the lab shrinkage tests—that is, the concrete water content continuously decreased. However, concrete in the field can dry or become wet depending on environmental conditions. Concrete can become wet when the air RH is high compared

with the RH in the concrete's air pores or because of rainfall. In fact, both the field unrestrained shrinkage prisms and the COA slabs experienced alternating increasing and decreasing shrinkage.

- *Uniaxial versus bending shrinkage.* The surfaces of the lab shrinkage prisms dried uniformly. Because of that, the prisms deformed uniaxially. It was also assumed that the field unrestrained shrinkage prisms deformed uniaxially since their thickness was relatively small (40 mm [1.6 in.]) and the strain was measured at mid-depth. However, this assumption was not valid for the concrete slabs, where drying shrinkage produced not only contraction but also upward bending. For pavement performance, that bending is as important as the contraction that the slabs undergo. The ACI and B3/B4 shrinkage models were not conceived to predict shrinkage bending.

As a first step to compare lab versus field shrinkage, the B4 model parameters were backcalculated for each of the mixes based on lab shrinkage data (instead of by using model equations). Then, the lab-calibrated model was used to predict shrinkage in the field. When moving from lab to field, curing time and size effects were considered based on the B4 equations (Section 6.3). The variable concrete temperature and air RH were considered using the *CalME* time-hardening approach. Several assumptions were made to model the wetting of the concrete due to air humidity, as explained in Section 6.3.

The B4 model was chosen for several reasons. First, it is the most recent shrinkage prediction model. Second, it explicitly considers concrete temperature (which the B3 and ACI models do not). Third, it is applicable to a wider range of concrete mixes than the other prediction models.

6.1 Overview of B4 Shrinkage Model

The B4 shrinkage prediction model is presented in Equation 6.1. This equation shows that shrinkage is predicted by multiplying the ultimate shrinkage ($\varepsilon_{Sh\infty}$) by two factors, one that accounts for air relative humidity (k_h) and another that accounts for the duration of the drying exposure (S). The notation used in Equation 6.1 and in this section of the report is the same used in the B4 model *(9)*.

$$\varepsilon_{Sh}(\tilde{t}, \tilde{t}_0) = \varepsilon_{Sh\infty}(\tilde{t}_0) \cdot k_h(RH) \cdot S(\tilde{t}) \quad \textbf{(6.1)}$$

where: $\varepsilon_{Sh\infty}$ is the ultimate shrinkage (long-term shrinkage for 0% air RH):

$$\varepsilon_{Sh\infty} = -\varepsilon_{\infty} \cdot k_{\varepsilon a} \cdot \frac{E(7 \cdot \beta_{Th} + 600 \cdot \beta_{Ts})}{E(\tilde{t}_0 + \tau_{Sh} \cdot \beta_{Ts})}$$

k_h is the air RH correction factor:

$$k_h = \begin{cases} 1 - RH^3 & if\ RH \leq 0.98 \\ -0.2\ (swelling) & if\ RH = 1 \\ linear\ interpolation & if\ 0.98 < RH < 1 \end{cases}$$

S is the time factor:

$$S(\tilde{t}) = tanh\sqrt{\frac{\tilde{t}}{\tau_{Sh}}}$$

τ_{Sh} is the shrinkage half-time (days):

$$\tau_{Sh} = \tau_0 \cdot k_{\tau a} \cdot \left(k_s \frac{D}{1\ mm}\right)^2$$

E is the concrete modulus of elasticity, as measured by ASTM C469

$\tilde{t}$ is the equivalent drying time (the superscript "~" indicates equivalent time, considering temperature history); if temperature was constant and equal to 20°C (68°F), $\tilde{t}$ would be the duration of the drying exposure

$\tilde{t}_0$ is the concrete equivalent (temperature corrected) age when drying begins; if temperature was constant, $\tilde{t}_0$ would be equal to concrete age (t_0) multiplied by the corresponding β_{Th}

β_{Th} is the time-temperature correspondence factor for cement hydration (applicable to curing time before drying); β_{Th} is a mix-dependent function of concrete temperature

β_{Ts} is the time-temperature correspondence factor for moisture diffusion (applicable to drying time); β_{Ts} is a mix-dependent function of concrete temperature

k_s is the shape factor that depends, exclusively, on specimen shape

D is the equivalent thickness of the specimen (two times the ratio of concrete volume to exposed surface)

$\varepsilon_\infty, k_{\varepsilon a}, \tau_0, k_{\tau a}$ are parameters that depend on mix properties (cement and aggregate types and proportions)

The following are several comments about the B4 model:

- The time factor, *S*, is a function of the exposure duration divided by the shrinkage half-time (τ_{Sh}). In other words, the duration of drying exposure is accounted for in relative terms.
- The shape and size of the specimen are accounted for in the shrinkage half-time. The larger the specimen, the larger the shrinkage half-time (and the slower the shrinkage that takes place).
- The age of the concrete when drying begins, t_0, has an effect on the ultimate shrinkage. The older the concrete when the drying begins, the larger the stiffness and the lower the ultimate shrinkage.

6.2 Lab Calibration of B4 Shrinkage Model

The B4 model, Equation 6.1, is fully defined with $\varepsilon_{Sh\infty}$ and τ_{Sh} parameters. The third factor in Equation 6.1 can be easily determined from air RH (50%, in this case): $k_h = 1\text{-}0.5^3 = 0.875$. Instead of using the model's equations, the

parameters $\varepsilon_{Sh\infty}$ and τ_{Sh} were backcalculated based on the lab shrinkage data. The backcalculation was conducted through an iterative process of error minimization using the Excel Solver tool. The backcalculated parameters are presented in Table 6.1, and the laboratory-calibrated model predictions are plotted together with actual lab shrinkage data in Figure 6.2.

Table 6.1: Lab-Calibrated Parameters of the B4 Shrinkage Model

Mix	Shrinkage Half-Time τ_{Sh}	Ultimate Shrinkage $\varepsilon_{Sh\infty}$
P2	31.8 days	-790 με
P3	59.0 days	-592 με
CSA	109.3 days	-185 με
P2-ICC	37.6 days	-655 με

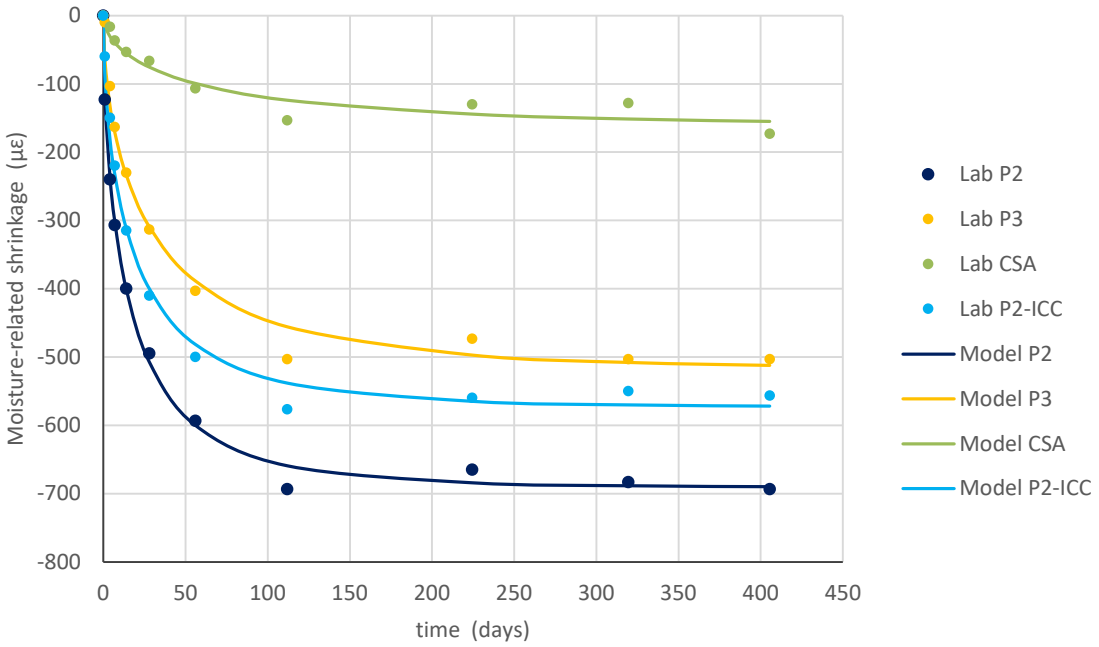

Figure 6.2: Lab-calibrated B4 shrinkage model.

The lab calibration of the B4 model was conducted without introducing any temperature correction. Because of that, the shrinkage half-time values in Table 6.1 are compatible with the 23°C (73°F) concrete temperature, which is the temperature in the lab shrinkage tests. The extrapolation of the model to any other temperature requires time-scaling with the corresponding time-temperature factor. Based on the B4 model, this factor is determined, shown in Equation 6.2.

$$\beta_{Ts} = exp\left[\frac{U_s}{R}\left(\frac{1}{273+T_R} - \frac{1}{273+T}\right)\right] \quad \textbf{(6.2)}$$

where: T is the concrete temperature

T_R is the reference temperature, 23°C (73°F)

R is the universal gas constant

U_s is the activation energy of moisture diffusion; the authors of B4 recommend a 4,000°K default value for U_s/R

6.3 Field Application of B4 Shrinkage Model

6.3.1 Extrapolation of B4 Lab-Calibrated Parameters to Field Specimens and Slabs

It should be noted that not only are the $\varepsilon_{Sh\infty}$ and τ_{Sh} parameters of the B4 model functions of the mix properties, but they depend on other variables as well. In Equation 6.1, $\varepsilon_{Sh\infty}$ also depends on the ratio of the concrete modulus of elasticity at 607 days and t_0 plus shrinkage half-time. τ_{Sh} also depends on the specimen shape and equivalent thickness (D). The dependency of $\varepsilon_{Sh\infty}$ and τ_{Sh} on these other variables is explicitly considered in the B4 equations (Equation 6.1). Because of that, the parameters can be easily extrapolated to field conditions, shown in Equation 6.3 and Equation 6.4. In both equations, the lab and field mixes are assumed to be identical. In Equation 6.4, temperature differences between the laboratory and the field are assumed to have a small effect on the stiffness ratio used in the prediction equation.

$$\tau_{Sh;FIELD} = \tau_{Sh;LAB} \cdot \frac{\left(k_{s;FIELD} \cdot D_{FIELD}\right)^2}{\left(k_{s;LAB} \cdot D_{LAB}\right)^2} \quad \textbf{(6.3)}$$

$$\varepsilon_{Sh\infty;FIELD} = \varepsilon_{Sh\infty;LAB} \cdot \frac{\frac{E\left(7 \cdot \beta_{Th;FIELD} + 600 \cdot \beta_{Ts;FIELD}\right)}{E\left(\tilde{t}_{0;FIELD} + \tau_{Sh;FIELD} \cdot \beta_{Ts;FIELD}\right)}}{\frac{E\left(7 \cdot \beta_{Th;LAB} + 600 \cdot \beta_{Ts;LAB}\right)}{E\left(\tilde{t}_{0;LAB} + \tau_{Sh;LAB} \cdot \beta_{Ts;LAB}\right)}} \approx \varepsilon_{Sh\infty;LAB} \cdot \frac{E\left(t_{0;LAB} + \tau_{Sh;LAB}\right)}{E\left(t_{0;FIELD} + \tau_{Sh;FIELD}\right)} \quad \textbf{(6.4)}$$

The extrapolated parameters $\varepsilon_{Sh\infty}$ and τ_{Sh} are shown in Table 6.2. The extrapolation required taking the following considerations into account:

- The equivalent thickness (D) of the lab specimens was 41.7 mm (1.6 in.), corresponding to a 100×100×250 mm (4×4×10 in.) prism. The equivalent thickness of the field unrestrained shrinkage prisms was 31.6 mm (1.2 in.), corresponding to a cross-section of 40×150 mm (1.6×6 in.). For the COA slabs, the equivalent thickness was twice the actual thickness (D = 230 mm [9 in.]) since drying was assumed to take place only from the top.

- The shape parameter, k_s, was assumed to be 1.25 (infinite prism) in the lab specimens and 1.0 (infinite slab) in the field unrestrained shrinkage prisms and in the COA slabs. Shape parameters corresponding to a variety of geometries are included in the B4 model *(9)*.
- The modulus of elasticity of the different mixes at each age was estimated based on the results of the laboratory testing conducted at OT, 4×OT, and 45 days. The lab results were fitted with a second-order polynomial function of the logarithm of time. The fitted function assumed a long-term versus 28-day ratio of 1.20 in the portland cement mixes and of 1.10 in the CSA mix. The ratio used in the portland cement mixes is the default value in the *MEPDG (1)*.
- The age when drying begins, t_0, is three days for the lab specimens. In the field, drying was assumed to start after one day.

Table 6.2: Extrapolation of B4 Model Lab Parameters to Field Conditions

Mix	Lab Prisms			Field Prisms			COA Slabs		
	τ_{Sh} (days)	$E(t_0+\tau_{Sh})$ (MPa)	$\varepsilon_{Sh\infty}$ (με)	τ_{Sh} (days)	$E(t_0+\tau_{Sh})$ (MPa)	$\varepsilon_{Sh\infty}$ (με)	τ_{Sh} (days)	$E(t_0+\tau_{Sh})$ (MPa)	$\varepsilon_{Sh\infty}$ (με)
P2	31.8	47,016	-790	11.7	43,588	-852	620.1	53,494	-694
P3	59.0	41,923	-592	21.7	40,472	-613	1150.3	46,116	-538
CSA	109.3	34,666	-185	40.2	33,937	-189	2130.7	36,433	-176
P2-ICC	37.6	43,142	-655	13.8	40,632	-696	733.6	48,319	-585

6.3.2 Consideration of Variable Temperature and Air Relative Humidity in the Field

Time evolution of temperature and air RH was modeled using the *CalME* time-hardening incremental-recursive approach. *CalME (11)* is a software program and the Caltrans ME design procedure for asphalt pavements. According to the *CalME* time-hardening approach, time is divided into intervals where problem conditions (air RH and concrete temperature, in this case) are regarded as constant. The damage (shrinkage in this case) at the beginning of each time interval is used together with the interval conditions to determine the damage at the end of the interval. This final damage is used as the input for the following time interval. These steps were followed to apply the *CalME* time-hardening approach to this particular research (Figure 6.3):

Step 1. Determination of interval conditions:

- Mean air RH during the time interval (RH_{MEAN}) and the corresponding k_h (Equation 6.1)
- Mean concrete temperature during the time interval (T_{MEAN}) and the corresponding β_{Ts} (Equation 6.2)
- Maximum shrinkage that can be reached under RH_{MEAN}: $\varepsilon_{Sh,MAX} = \varepsilon_{Sh\infty} \cdot k_h$

Step 2. Determination of interval initial conditions:

- Initial shrinkage, $\varepsilon_{Sh,INI}$

- Equivalent time factor at the beginning of the interval: $S_{INI} = \varepsilon_{Sh,INI}/\varepsilon_{Sh,MAX}$
- Equivalent time at the beginning of the interval: $\tilde{t}_{INI} = [arc\,tanh(S_{INI})]^2 \cdot \tau_{Sh}$

Step 3. Determination of interval final conditions:

- Equivalent time at the end of the interval: $\tilde{t}_{END} = \tilde{t}_{INI} + \beta_{Ts} \cdot \Delta t$
- Equivalent time factor at the end of the interval: $S_{END} = tanh\sqrt{\tilde{t}_{END}/\tau_{Sh}}$
- Final shrinkage: $\varepsilon_{Sh,END} = \varepsilon_{Sh\infty} \cdot k_h \cdot S_{END}$

Step 4. Use $\varepsilon_{Sh;END}$ as initial condition of the following interval, and repeat Steps 1 through 4.

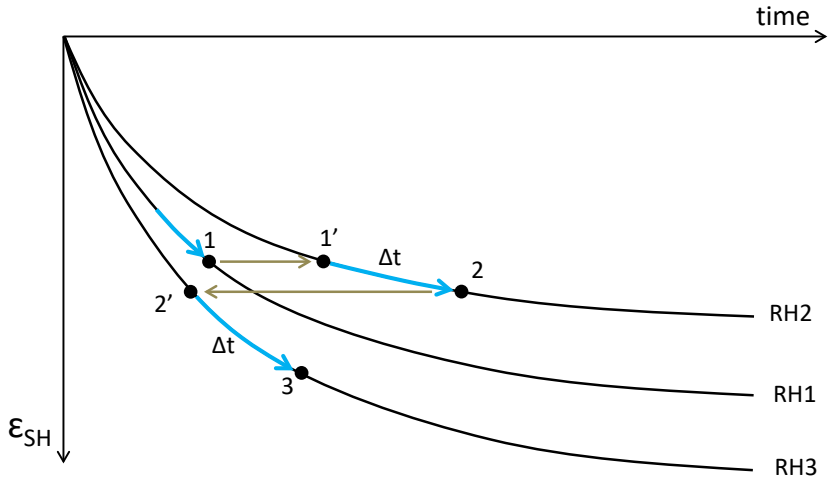

Figure 6.3: Application of the *CalME* time-hardening approach to modeling shrinkage evolution.

The approach presented in Steps 1 through 4 results in monotonically increasing shrinkage—that is, the approach cannot reproduce shrinkage reduction. Still, both the field unrestrained shrinkage prisms and the COA slabs experienced alternating increasing and decreasing shrinkage. Shrinkage reduction took place as a consequence of rainfall but also, apparently, as a consequence of air RH. This limitation of the approach can be easily illustrated through Figure 6.3, which shows that the air RH during time interval 3 was RH3. If air RH after this interval returned to RH2, the actual value of the shrinkage would be larger (in absolute value) than the maximum shrinkage that can be reached when air RH is RH2. Based on Step 2, this situation would mean ε_{INI} is larger (in absolute value) than $\varepsilon_{Sh,MAX}$, so S_{INI} would be larger than 1. This would result in an error when trying to calculate the inverse hyperbolic tangent of a number larger than 1. From the physical point of view, the situation described corresponds to a wetting period where the RH in concrete air pores would increase because of a relatively high air RH.

The problem described was overcome by modeling concrete wetting due to air RH. Two assumptions were made in order to conduct this modeling: (1) concrete shrinkage reduction (in absolute value) takes place when actual

shrinkage is larger (in absolute value) than the maximum shrinkage that concrete can reach under the existing air RH ($|\varepsilon_{INI}| > |\varepsilon_{Sh,MAX}|$) and (2) the wetting curve (shrinkage reduction curve) is symmetric to the drying curve corresponding to the existing air RH, with the axis of symmetry axle being the asymptote of the drying curve. This hypothesis is illustrated in Figure 6.4.

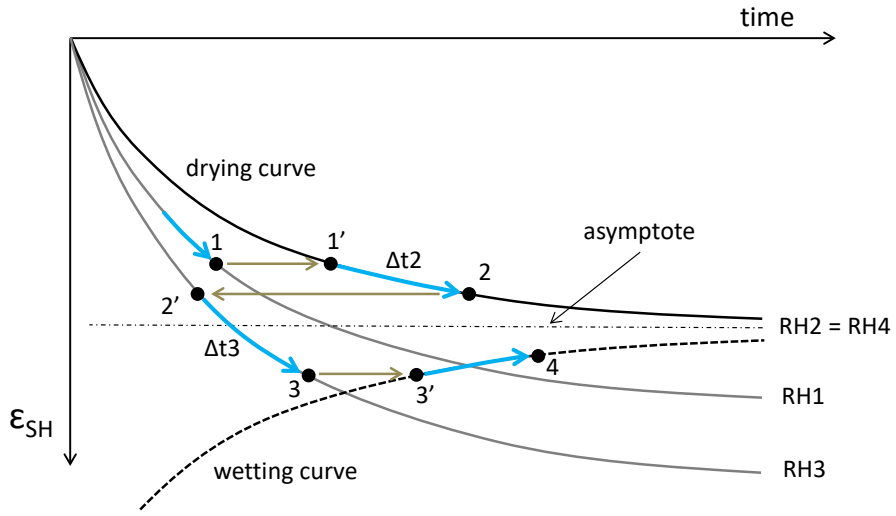

Note: The curves "drying" and "wetting" are symmetric versus the horizontal asymptote.

Figure 6.4: Hypothesis for modeling concrete wetting due to air RH.

The implementation of the hypothesis shown in Figure 6.4 was conducted by introducing a "drying" variable that was +1 in drying intervals and -1 in wetting intervals (i.e., when $|\varepsilon_{INI}| > |\varepsilon_{Sh,MAX}|$). Steps 2 and 3 of the four-step approach after this modification are the following (Steps 1 and 4 remain the same):

Step 2. Determination of interval initial conditions:

- Initial shrinkage, $\varepsilon_{Sh;INI}$
- Drying or wetting interval: $D = \begin{cases} 1 & if\ |\varepsilon_{Sh,INI}| \le |\varepsilon_{Sh,MAX}| \\ -1 & if\ |\varepsilon_{Sh,INI}| > |\varepsilon_{Sh,MAX}| \end{cases}$
- Calculus initial strain: $\varepsilon_{Sh;INI;CALC} = \begin{cases} \varepsilon_{Sh,INI} & if\ D = 1 \\ 2 \cdot \varepsilon_{Sh,MAX} - \varepsilon_{Sh,INI} & if\ D = -1 \end{cases}$
- Equivalent time factor at the beginning of the interval: $S_{INI} = \varepsilon_{Sh,INI,CALC} / \varepsilon_{Sh,MAX}$
- Equivalent time at the beginning of the interval: $\tilde{t}_{INI} = [arc\,tanh(S_{INI})]^2 \cdot \tau_{Sh}$

Step 3. Determination of interval final conditions:

- Equivalent time at the end of the interval: $\tilde{t}_{END} = \tilde{t}_{INI} + \beta_{Ts} \cdot \Delta t$
- Equivalent time factor at the end of the interval: $S_{END} = tanh\sqrt{\tilde{t}_{END} / \tau_{Sh}}$
- Change in strain during the interval: $\Delta\varepsilon_{CALC} = \varepsilon_{Sh\infty} \cdot k_h \cdot (S_{END} - S_{INI})$
- Final shrinkage: $\varepsilon_{Sh,END} = \varepsilon_{Sh,INI} + D \cdot \Delta\varepsilon_{CALC}$

The combination of the B4 shrinkage model, the *CalME* time-hardening approach, and the aforementioned hypothesis to model concrete wetting due to air RH is referred to as the "B4-IR" model in this report. The suffix IR stands for "incremental-recursive."

In this study, the time interval considered in the incremental-recursive approach was one day. Mean air relative humidity (RH_{MEAN}) and mean concrete temperature (T_{MEAN}) were, consequently, the daily mean values. In the unrestrained shrinkage prisms, concrete temperature is the temperature measured with the strain gauge inside the prism. In the COA slabs, concrete temperature is the average through the thickness of the slab, which is determined based on thermocouple readings at four depths. Concrete wetting due to rainfalls was not modeled in this study because additional research is required before shrinkage reversals due to rainfalls can be adequately modeled.

6.4 Relationship Between Lab and Field Shrinkage in the Unrestrained Shrinkage Prisms

As previously explained, the B4-IR model combines the B4 model, the *CalME* time-hardening approach, and a simplified hypothesis to account for concrete wetting due to air RH. The model's parameters $\varepsilon_{Sh\infty}$ and τ_{Sh} were initially calibrated based on laboratory shrinkage test data and then extrapolated to the field using the B4 equations. Comparisons between measured (backcalculated) moisture-related shrinkage in the field unrestrained shrinkage prisms and predictions by the B4-IR model are shown in Figure 6.5 (for the portland cement mixes) and Figure 6.6 (for the CSA mix). Overall, the comparisons show excellent agreement between measured and predicted shrinkage for the three portland cement mixes, but the model underestimated shrinkage for the CSA mix. It should be noted that concrete wetting due to rainfall was not modeled, so the model was forced to fit the measured shrinkage after each of the rainfall periods. In other words, the initial shrinkage ($\varepsilon_{Sh,INI}$) in the time intervals following rainfalls was not estimated but was just assumed to be equal to the shrinkage measured at the beginning of the interval.

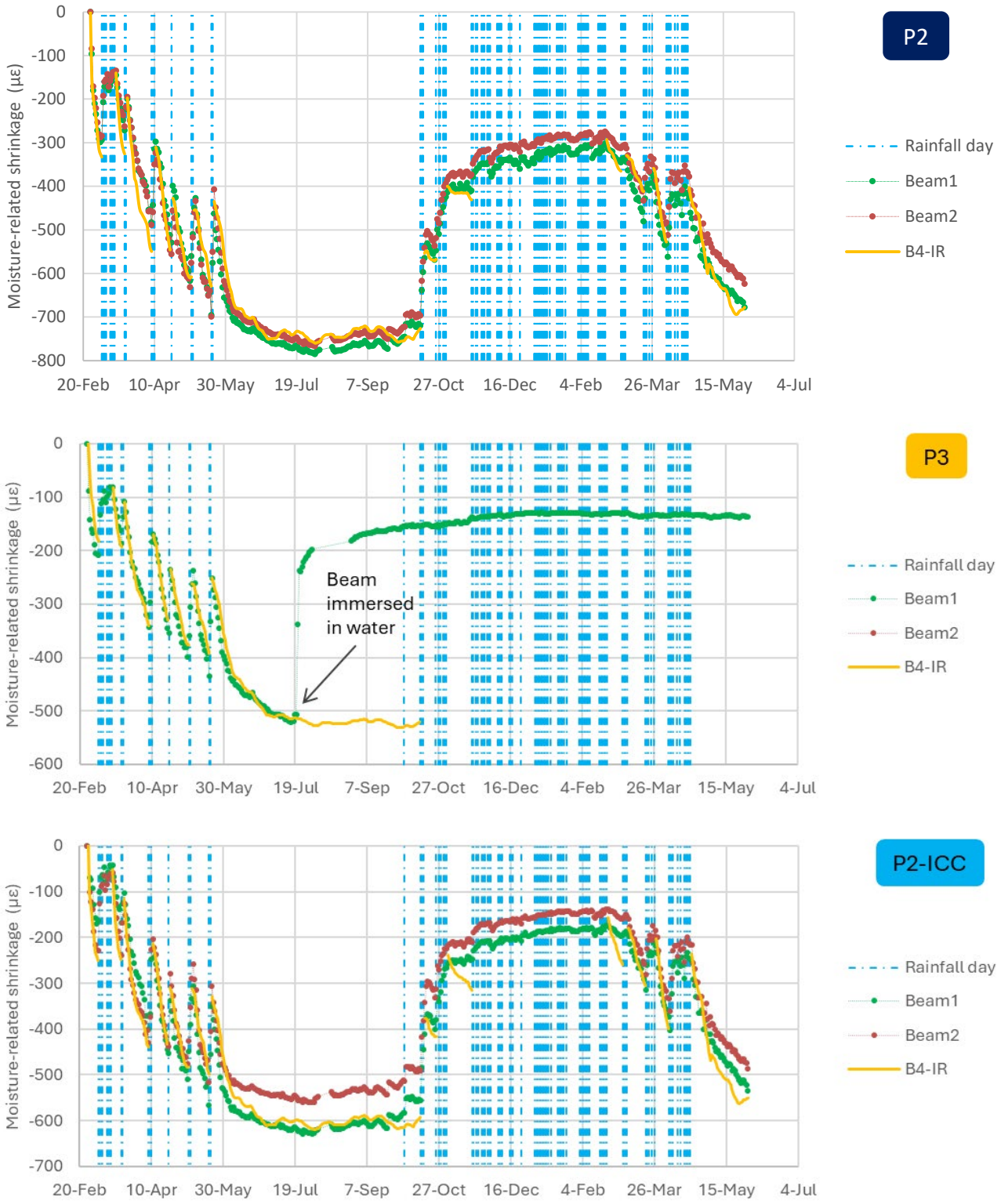

Figure 6.5: Evaluation of B4-IR model for the unrestrained shrinkage prisms with portland cement.

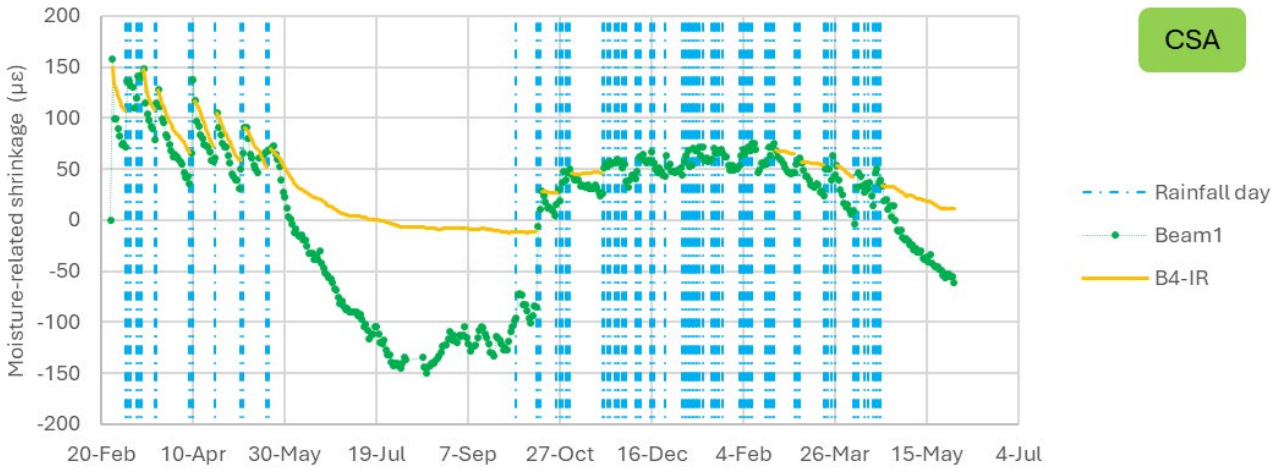

Note: Since expansion was measured in this mix, shrinkage data was shifted -150 με in order to do model calculations.

Figure 6.6: Evaluation of the B4-IR model for the unrestrained shrinkage prisms with CSA cement.

An interesting observation from Figure 6.5 is that the model mimicked shrinkage fluctuations measured in the portland cement prisms during the summer of 2016. This indicates that those fluctuations are unrelated to random errors in measuring or in the analysis of the strain data and instead reflect changes in air RH that affected the moisture condition of the field prisms.

Good agreement between measured and predicted shrinkage was not expected for the internally cured mix because it was believed this mix was produced in the field with a relatively high water content. This hypothesis was first formulated based on the relatively low strength of this field-produced mix compared with the P2 mix and with the same P2-ICC mix produced in the lab *(10)*. The hypothesis was supported by RH measurements at 20 mm (0.8 in.) depth since the drying performance of the P2-ICC mix was worse than the performance of the P2 mix *(4)*. A relatively high water content in the field P2-ICC mix would result in higher porosity and, consequently, higher susceptibility to drying compared with the same mix produced in the lab. Since the model calibration was based on lab mix shrinkage data, the model's predictions were expected to underestimate shrinkage—at least the speed of shrinkage development—in the field mix.

The good predictions for the portland cement mixes in the B4-IR model contrasted with the bad outcome for the CSA mix (Figure 6.6). This outcome is likely related to the fact that the B4 equations were not calibrated for mixes with CSA cement. Although model parameters $\varepsilon_{Sh\infty}$ and τ_{Sh} were initially calibrated based on lab data (not a prediction equation), the extrapolation to field conditions was based on the B4 equations, which are not conceived for mixes with CSA cement. Moisture-related shrinkage is known to be very different in CSA cement than in portland cement *(39)*.

As explained in Section 6.3.2, the incremental-recursive modeling was implemented in one-day time increments. Concrete temperature and air RH in each of these time intervals were assumed to be the daily mean values. This assumption is debatable since the relationship between shrinkage and each of these two variables is not linear. Therefore, even though the assumption worked in this particular case, it is still recommended that the topic be studied further.

6.5 Relationship Between Lab and Field Shrinkage in the Concrete on Asphalt Slabs

Drying shrinkage in the COA slabs was modeled with B4-IR following the same four-step approach used with the unrestrained shrinkage prisms. The modeled variable in the COA slabs was $\varepsilon_{MEAN,Shr}$ (slab expansion/contraction). Slab bending ($\varepsilon_{DIFF,Shr}$) can be determined based on slab expansion/contraction, but this determination requires assuming an unrestrained shrinkage profile with just one degree of freedom. That determination consists of three steps: (1) use the B4-IR model to predict $\varepsilon_{MEAN,Shr}$, (2) use $\varepsilon_{MEAN,Shr}$ to backcalculate the unrestrained shrinkage profile, and (3) use the unrestrained shrinkage profile to determine $\varepsilon_{DIFF,Shr}$.

In this study, the unrestrained shrinkage was assumed to follow the evolution pattern shown in Figure 6.7 (left). This figure shows that unrestrained shrinkage is assumed to be constant at the top of the slab, ε_{TOP}, and it is assumed to decrease linearly versus depth until it either reaches zero at a certain depth in the slab or reaches ε1 at the bottom of the slab. The degree of freedom of this shrinkage profile is the characteristic depth of drying, DDK, shown in Figure 6.7.

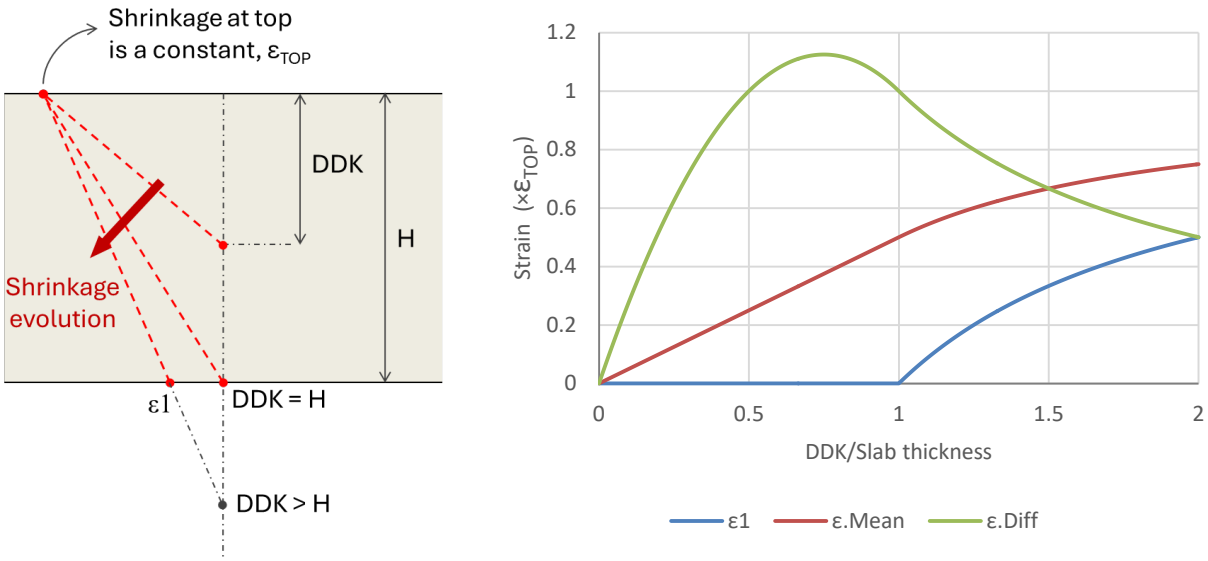

Figure 6.7: Evolution of unrestrained shrinkage profile assumed in the slabs.

In summary, the approach that was followed to determine $\varepsilon_{DIFF,Shr}$ consisted of the following steps:

(1) For each time interval, $\varepsilon_{MEAN,Shr}$ was determined following the same incremental-recursive procedure that was used for the unrestrained shrinkage prisms. The parameters τ_{Sh} and $\varepsilon_{Sh\infty}$ are shown in Table 6.2.

(2) For each time interval, Equation 6.5 was used to determine r (DDK/H) based on $\varepsilon_{MEAN,Shr}$.

(3) For each time interval, r was used to determine $\varepsilon_{DIFF,Shr}$ with Equation 6.6.

$$\varepsilon_{MEAN,Sh} = \begin{cases} \frac{1}{2} \cdot \varepsilon_{TOP} \cdot r & if\ r \leq 1 \\ \frac{\varepsilon_{TOP} + \varepsilon 1}{2} & if\ r > 1 \end{cases} \quad \textbf{(6.5)}$$

$$\varepsilon_{DIFF,Sh} = 6 \cdot (\varepsilon_{TOP} - \varepsilon 1) \cdot r \cdot \left(\frac{1}{2} - \frac{r}{3}\right) \quad \textbf{(6.6)}$$

where: r relative characteristic depth of drying, DDK/slab thickness
ε_{TOP} unrestrained shrinkage at the slab top
$\varepsilon 1$ unrestrained shrinkage at the slab bottom

The strain at the top of the slab, ε_{TOP}, was assumed to be a constant, shown in Figure 6.7. The logic behind this assumption is that drying takes place very fast at the top of the slab and, consequently, shrinkage at this location reaches the maximum value very quickly. The main problem with this assumption is that shrinkage depends on air RH. Therefore, even if drying in the top millimeters (tenths of an inch) of the slab took place immediately, ε_{TOP} would be still a function of air RH. In this study, ε_{TOP} was assumed to be the long-term shrinkage at 50% air RH. That strain is the product that results from multiplying the field-adjusted $\varepsilon_{Sh\infty}$ parameter (Table 6.2) by the 50% RH correction factor ($k_h = 1\text{-}0.5^3$). This air RH was selected since the daily mean values of this variable fluctuated between 40% and 60% during the summer of 2016.

Model B4-IR predictions are shown in Figure 6.8 together with the differential shrinkage measured (backcalculated) in the COA slabs. Although the prediction errors were comparable to the variability between the different pairs of strain gauges, the model tended to overestimate the measured response. One reasons for the overestimation is the assumption that drying does not affect the bottom of the slab (at least not during an initial phase when DDK ≤ slab thickness). Because of this assumption, a change in $\varepsilon_{MEAN,Shr}$ will translate into a higher change in $\varepsilon_{DIFF,Shr}$ compared with a scenario where the strain at the bottom of the slab changes as well. The backcalculated drying shrinkage in the COA slabs was compatible with the $\varepsilon_{Sh\infty}$ parameters below the extrapolated values reflected in Table 6.2. To match measured data, the $\varepsilon_{Sh\infty}$ parameters in Table 6.2 should be reduced by 25%, 10%, and 5% in the sections with mixes P2, P3, and P2-ICC, respectively. The final $\varepsilon_{Sh\infty}$ parameters are shown in Table 6.3.

Table 6.3: B4 Model Parameters Used in COA Slab Modeling

Mix	Direct Extrapolation (Table 6.2) (used in series B4-IR in Figure 6.8)		Field-Adjusted (used in series B4-IR (2) in Figure 6.8)	
	τ_{Sh} (days)	$\varepsilon_{Sh\infty}$ (με)	τ_{Sh} (days)	$\varepsilon_{Sh\infty}$ (με)
P2	620	-694	620	-521
P2+SRA	Not measured[a]		620	-382
P3	1,150	-538	1,150	-484
P2-ICC	734	-585	404	-566

[a] The mix P2 treated with SRA was not evaluated in the laboratory. The differential shrinkage measured in the corresponding COA slab was compatible with 45% reduction in εSh∞ (-694 με) in the P2 mix.

In the section with P2-ICC mix, measured differential shrinkage seemed to develop faster than predicted by the model. For this section, the model's predictions improved considerably when the shrinkage half-time parameter (τ_{Sh}) was reduced. Reducing τ_{Sh} in this section agrees with the hypothesis that was formulated for the P2-ICC field mix. That hypothesis was that the water content in this mix was higher than that specified in the job mix formula and that because of this relatively high water content, the field mix would be more susceptible to drying than the lab mix. Consequently, the shrinkage half-time extrapolated from lab mix results was expected to overestimate the shrinkage half-time of the field mix. The B4-IR predictions matched the measured data for this section when τ_{Sh} was reduced by 45%. That reduction is equivalent to reducing the slab thickness by 25%, since τ_{Sh} depends on the square of the equivalent thickness of the specimen (Equation 6.1).

The field concrete was cured with curing compound in all the COA sections. In Section M, an SRA solution was sprayed on the surface before the application of the curing compound. That combination was not evaluated in the laboratory, so the τ_{Sh} and $\varepsilon_{Sh\infty}$ parameters of the B4 model could not be determined in the laboratory or extrapolated to the field. The differential drying shrinkage measured in Section M was compatible with a 45% reduction in $\varepsilon_{Sh\infty}$ in the P2 mix.

The B4-IR model's predictions after modification of the τ_{Sh} and $\varepsilon_{Sh\infty}$ parameters (Table 6.3) are included in Figure 6.8 as the series "B4-IR (2)." Overall, excellent agreement was achieved for the three portland cement mixes. No results are shown for Section O, the CSA mix because, as expected, model predictions could not reproduce the measured differential shrinkage.

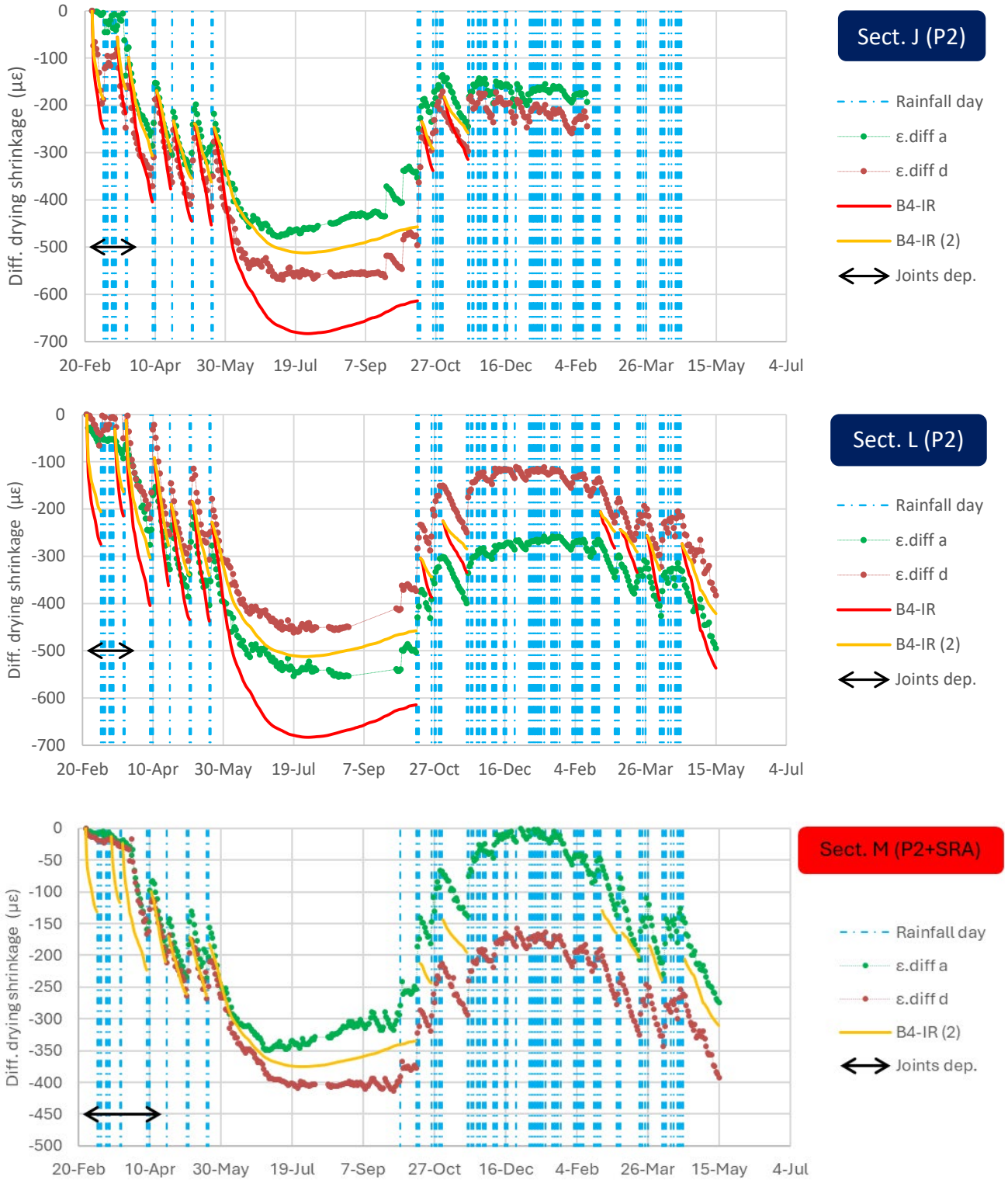

Notes: The series "ε.diff a" and "ε.diff d" correspond to two pairs of strain gauges located at two different joints. B4-IR(2) results are after modification of ultimate shrinkage and shrinkage half-time parameters.

Figure 6.8: Evaluation of the B4-IR model for the COA slabs with Type II/V portland cement.

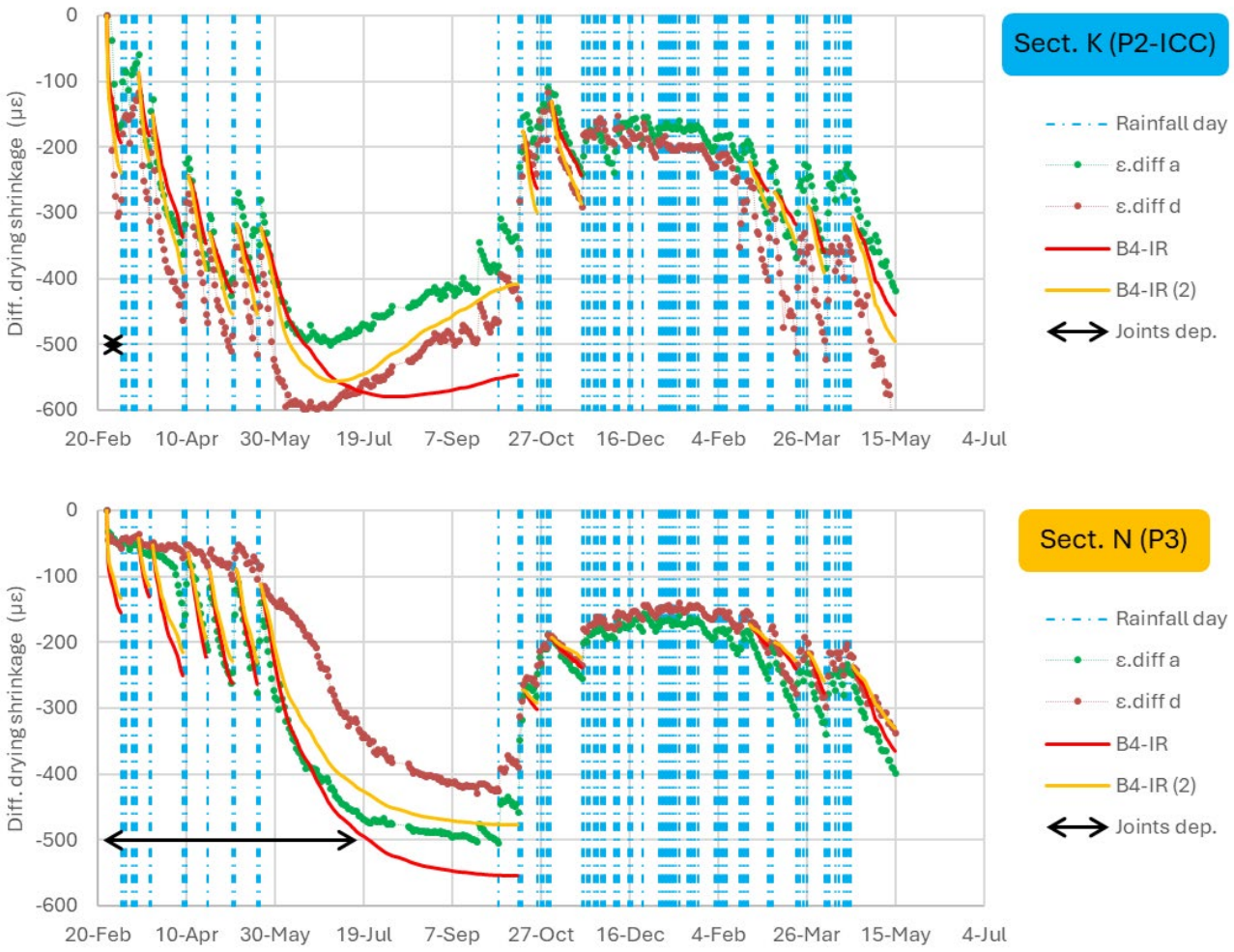

Note: B4-IR(2) results are after modification of ultimate shrinkage and shrinkage half-time parameters**.**

Figure 6.8 (cont.): Evaluation of the B4-IR model for the COA slabs with internally cured and Type III portland cement.

The joint deployment period is shown for each section in Figure 6.8. As expected, the model overpredicted the measured differential shrinkage before the joints were fully deployed. This is particularly noticeable for Section N, which is where the joints deployed last.

It should be noted that concrete wetting due to rainfall was not modeled, so the B4-IR model was forced to fit the measured differential shrinkage after each of the rainfall periods. In other words, the initial differential shrinkage ($\varepsilon_{Sh,DIFF,INI}$) in the time intervals following rainfalls was not estimated and was just assumed to be equal to the differential shrinkage measured in the slabs at the beginning of the interval.

As shown in Figure 6.7, the modeling assumed that unrestrained shrinkage was constant at the top of the slab while the shrinkage depth changed as the slab concrete dried. This assumption is very different from the one in

the *MEPDG,* where the depth of drying is kept constant and the unrestrained shrinkage at the top of the slab is the one that is assumed to change as the slab concrete dries. An attempt was made to reproduce the measured shrinkage using the B4-IR model with this second assumption, but it was not possible, even when very unrealistic correction factors were applied to the τ_{Sh} and $\varepsilon_{Sh\infty}$ parameters.

7 MODELING SLABS RESPONSE TO THE SHRINKAGE ACTION

This chapter focuses on the last question called out in the introduction: *What is the stress due to moisture-related shrinkage?* To answer this question, the structural response of the COA slabs under the shrinkage action was modeled using the finite element method (FEM). The unrestrained shrinkage action was assumed to be at its maximum, in terms of absolute value, at the top of the slab and decrease linearly versus depth until it reached zero at the slab half-depth (Figure 7.1). The unrestrained shrinkage was assumed to be zero in the bottom half of the slab. The unrestrained shrinkage at the top of the slab was assumed to be the long-term shrinkage at 50% air RH, the same assumption that was made for the B4-IR modeling presented in Section 6.5. That strain at the top of the slab, which is shown for each mix in Table 7.1, is the product that results from multiplying the field-adjusted $\varepsilon_{Sh\infty}$ parameter (Table 6.3) by the 50% RH correction factor (k_h = 1-0.5^3). As explained in Section 6.5, that air RH was chosen because the daily mean values of air RH fluctuated between 40% and 60% during the summer of 2016.

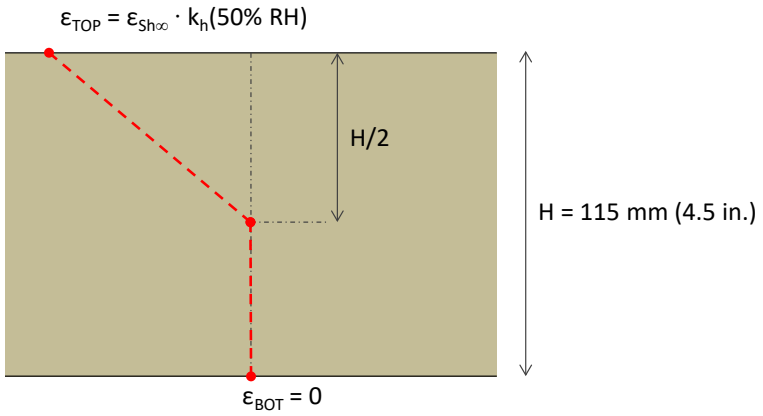

Figure 7.1: Unrestrained shrinkage action used in FEM modeling.

Table 7.1: Shrinkage Action at Slab Top

Mix	$\varepsilon_{Sh\infty}$ (με)	ε_{TOP} (με)
P2	-521	-455
P2+SRA	-382	-334
P3	-484	-424
P2-ICC	-566	-495

Both 6×6 and 12×12 slab sizes were modeled with FEM. The 12×12 section with P2-ICC showed generalized surface microcracking that was unrelated to traffic loading (*40*). That microcracking, which was first observed about 15 months after construction, occurred in the center of the slab and at the edges (Figure 7.2). The cracking depth was minor (millimetric size) and the orientation seemed random. The microcracks did not coalesce into a

single crack discrete in any case. The cracking was not related to traffic loading as it was present in areas far from the HVS wheelpath that had not been subjected to any loading. On the contrary, no surface microcracking was observed in the 12×12 Section J, with mix P2. The differences between these two sections were related to the concrete mix since they shared the same asphalt base and underlying structure and were built the same day at approximately the same time. No surface microcracking was observed in the 6×6 sections. Section L was the only 6×6 section that was modeled with FEM. The rest of the 6×6 sections showed lower shrinkage and were expected to be less critical for top-down cracking than Section L.

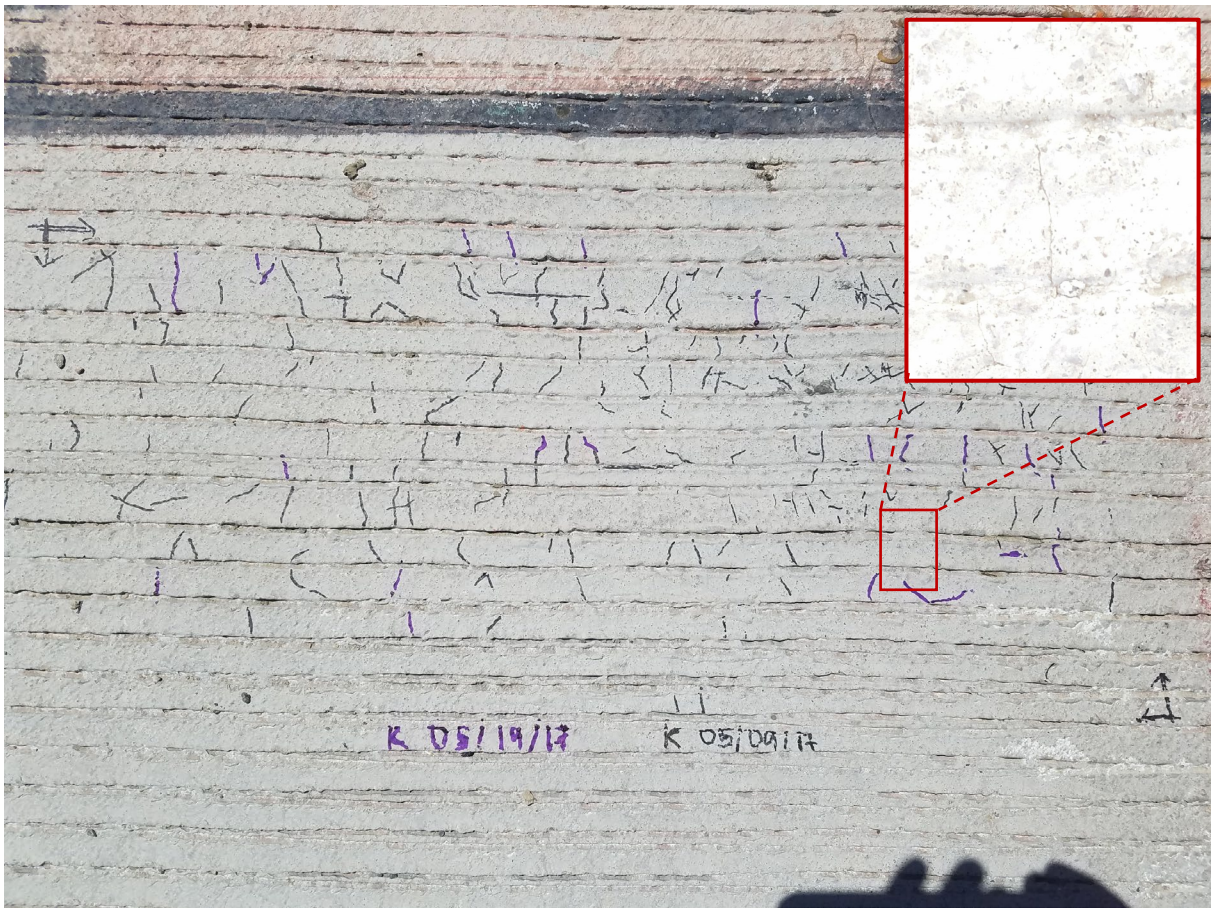

Figure 7.2: Surface microcracking on 12×12 section with P2-ICC.

The drying reaches the slab half-depth in the shrinkage profile shown in Figure 7.1. Based on the B4-IR modeling (Section 6.5), that condition occurred around early June 2016 in the section with P2-ICC mix and around late June 2016 in the sections with P2 mix. It should be noted that the shrinkage action shown in Figure 7.1 is not necessarily the most critical for top-down cracking—that is, the action that results in the highest tensile stresses at the top of the slab compared with the flexural strength of the mix. Other drying profiles may exist that result in a more

critical condition. Nonetheless, the profile shown in Figure 7.1 was regarded as appropriate enough for the analysis presented in this report.

7.1 Consideration of the Shrinkage Action

The modeling presented in this report accounts for the time-dependent behavior of concrete and asphalt mixes. Defining the unrestrained shrinkage profile (as in Figure 7.1 and Table 7.1) is not enough to fully define the shrinkage action, and loading time is required as well. Strictly speaking, the modeling should require defining the shrinkage profile as a function of time. However, to simplify the calculations, the shrinkage action was assumed to increase linearly over four months, from February 2016, when the slabs were constructed, until June 2016, when drying reached the half-depth of the slabs.

7.2 Consideration of Concrete and Asphalt Creep/Relaxation Capacity

The creep/relaxation capacity of the concrete and asphalt were considered by modeling those materials as linear viscoelastic. The viscoelastic model was the generalized Maxwell model, which is also known as the Maxwell-Wiechert model. This model consists of a series of Maxwell models arranged in parallel, shown in Figure 7.3. It should be noted that the Maxwell model is a spring and a dashpot in series. The complex modulus and the relaxation modulus can easily be determined from the model's parameters, which are the constants of the springs and dashpots.

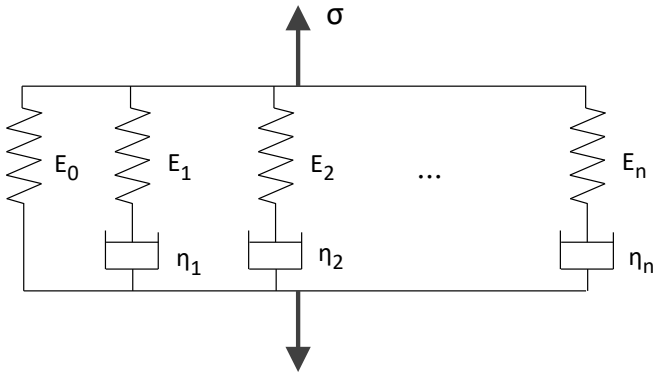

Figure 7.3: Viscoelastic model used for concrete and asphalt (generalized Maxwell model).

The generalized Maxwell model was chosen because it is the linear viscoelastic model used by the FEM software *Abaqus*, which was used to analyze the data in this report. *Abaqus* is a widely known FEM program that can be used for mechanistic and thermal analyses, among other types of analyses. The program defines material viscoelasticity for shear and volumetric behavior independently. Therefore, two generalized Maxwell models need to be defined for each material, one for shear stiffness and another for bulk stiffness.

7.2.1 Determination of Viscoelastic Model's Parameters in the Asphalt Mixes

The parameters of the generalized Maxwell model were determined based on the results of dynamic modulus testing. As explained in Section 3.5.7, frequency sweep dynamic modulus testing was conducted at 10°C, 25°C, and 40°C (50°F, 77°F, and 104°F). The results of that testing were used to build the dynamic modulus master curve (Figure 3.12) and the Black diagrams (Figure 3.13) of the asphalt mixes. Those data referred exclusively to longitudinal stiffness (E*), but the model definition required the complex shear modulus (G*) and the complex bulk modulus, (K*). Some simplifications and assumptions were done to overcome this limitation, as explained in the following discussion.

It is important to clarify that E*, υ* (Poisson ratio), G*, and K* are complex numbers. Their mathematical moduli—|E*|, |υ*|, |G*|, and |K*|—are referred to as dynamic longitudinal modulus, dynamic Poisson's ratio, dynamic shear modulus, and dynamic bulk modulus, respectively.

Most of the viscoelasticity of an asphalt mix is attributed to its shear stiffness. For this reason, a reasonable approach for modeling this material is assuming that its bulk modulus is linear elastic (constant versus frequency) while its shear modulus is linear viscoelastic *(41)*. The bulk modulus, K, can be determined using the maximum Young modulus, Eg (E* for infinite frequency), once the Poisson's ratio is assumed. At infinite frequency, asphalt is assumed to be an elastic material (phase angle equals zero) and, consequently, Eg and the assumed Poisson's ratio can be used to determine K using the formula based on elasticity: $K = Eg/3/(1-2 \cdot \upsilon g)$. In this study, the Poisson's ratio at infinite frequency, υg, was assumed to be 0.1. Once the bulk modulus was determined, it was used with E* to determine G* at each frequency. As a final step, the set of G* values were used to backcalculate the parameters of the generalized Maxwell model. In this project, 20 parallel Maxwell elements were included in the generalized model. For each Maxwell element, the relaxation time (Gi/ηi) was fixed and the spring constant (Gi) was backcalculated. Relaxation times of 10^{-7} to 10^{9} seconds were chosen for the Maxwell elements so that the model could provide a good match to the experimental data for the required range of reduced frequencies. Figure 7.4 includes an outline of the approach described, and the results of the fitting are shown in Figure 7.5 (dynamic shear modulus) and Figure 7.6 (phase angle of shear modulus).

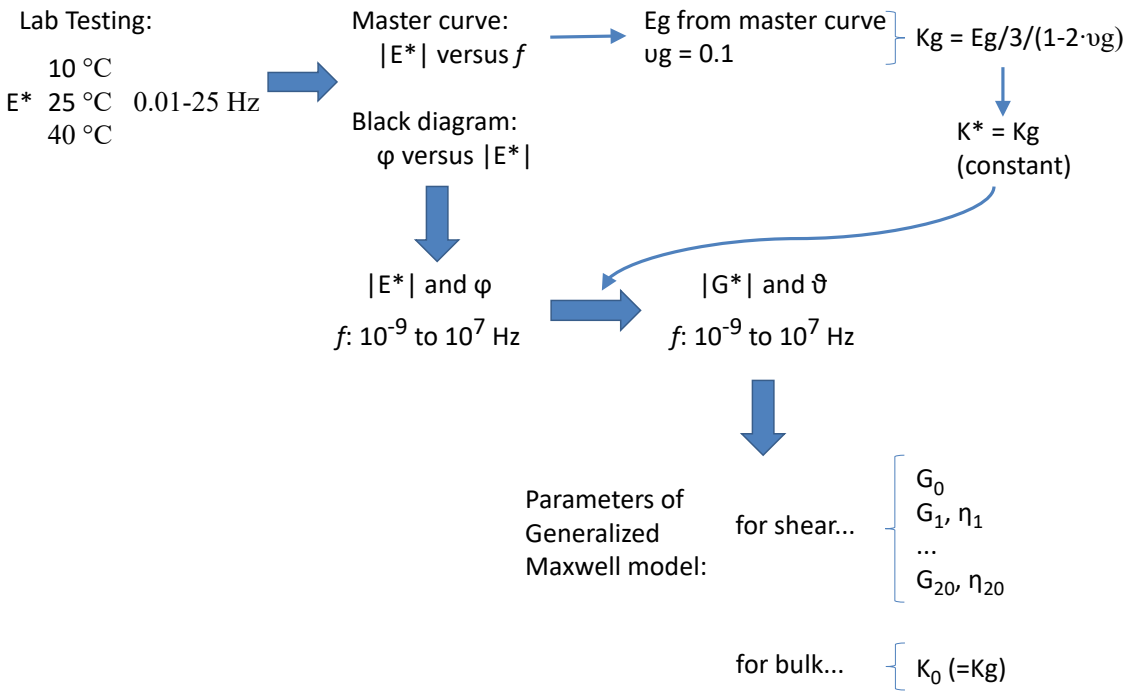

Figure 7.4: Approach for determining the parameters of the asphalt viscoelastic model.

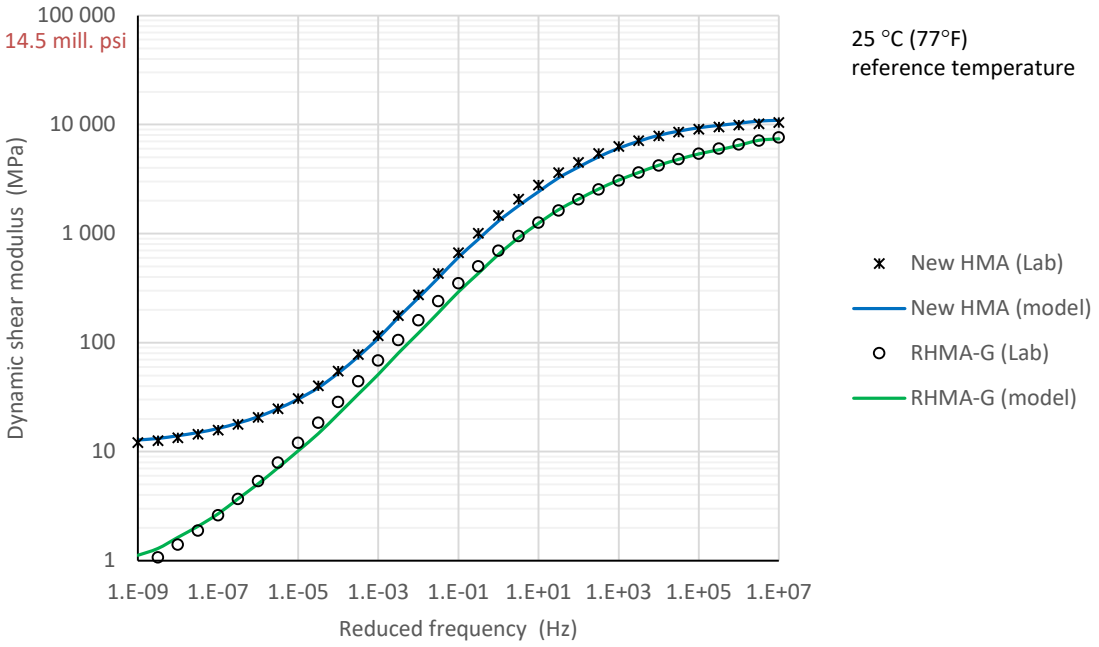

Figure 7.5: Fitting of experimental data with the generalized Maxwell model (dynamic shear modulus).

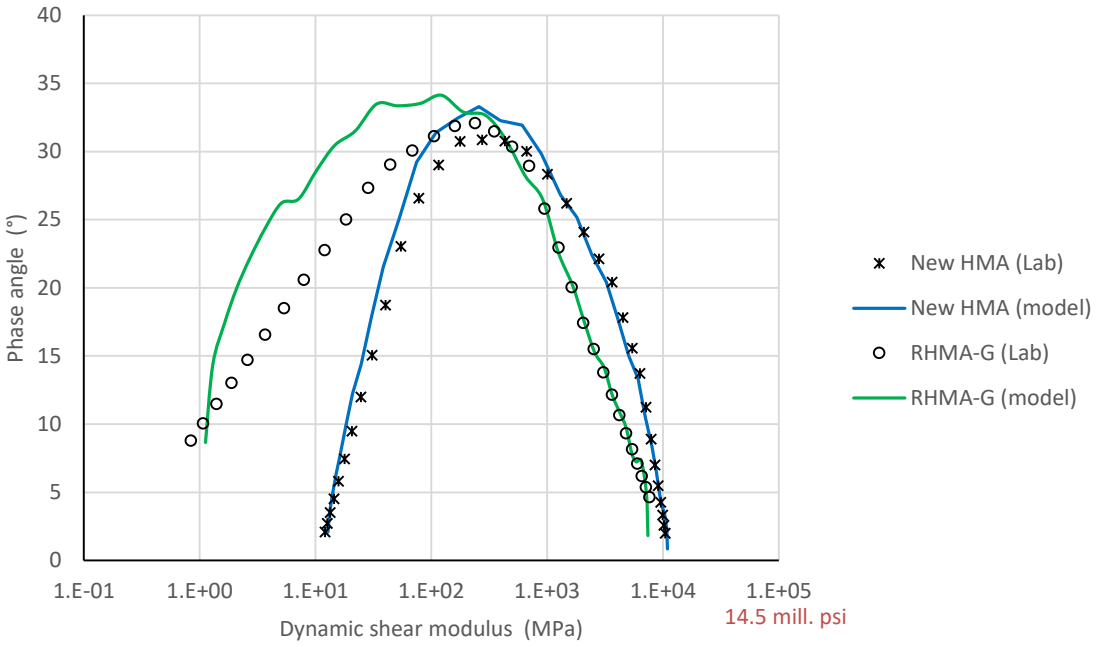

Figure 7.6: Fitting of experimental data with the generalized Maxwell model (phase angle of shear modulus).

It should be noted that part of the "Lab" data in Figure 7.5 and Figure 7.6 are extrapolations of the lab results. The actual lab results correspond to a reduced frequency range from 10^{-4} to 10^{3} Hz, shown in Figure 3.12. The data above 10^{3} Hz and below 10^{-4} Hz were extrapolated using the master curve. The extrapolation of the low frequencies is particularly uncertain since the actual lab results can be fitted, with an almost identical fitting error, using different master curves where the minimum stiffness varies considerably. This limitation could be overcome, in theory, by extending the experimental reduced frequency range (e.g., by testing at temperatures higher than 40°C [104°F]). However, other problems related to plastic deformations and the nonlinearity of the asphalt mix would then make the results questionable. The fact is that defining the stiffness of the asphalt for a very low loading frequency, like the frequency that would correspond to the shrinkage action, is a very complex task. At that low frequency, the asphalt aggregate skeleton plays a major role in the stiffness of the asphalt, and this may result in strong nonlinearity and anisotropy as well as a different behavior in tension versus compression. In this study, no attempt was made to follow a more fundamental approach to defining the minimum stiffness of the asphalt mix.

It should be noted that the approach in Figure 7.4 could be followed for the mixes labeled "New HMA" and "RHMA-G," but not for the "Old HMA" mix. As explained in Section 3.5.7, dynamic modulus testing could not be conducted in the Old HMA since test specimens could not be extracted from the existing asphalt lifts. The Old HMA mix was the same type as the New HMA mix, which means that it had similar gradation, binder content,

binder type, and compaction level. However, the Old HMA layer was built in 2012 and had experienced somewhat more aging than the New HMA, which was built in 2015. Some of the Old HMA areas were tested with the HVS in an earlier research project, and an evaluation with the FWD showed that the stiffness of the Old HMA mix was similar to the laboratory values measured of the New HMA mix. For this reason, the Old HMA mix was modeled with *Abaqus* using the parameters of the New HMA mix.

The temperature of the asphalt mixes varied daily and seasonally during the four-month period modeled in this report. That variation can be accounted for using the time-temperature correspondence principle. However, to simplify the calculations, a constant temperature of 25°C (77°F) was assumed in the modeling. That was approximately the average temperature of the asphalt mix during the modeled period.

7.2.2 Determination of Viscoelastic Model's Parameters in the Concrete Mixes

The modulus of elasticity of concrete was measured in the laboratory following ASTM C469. Unfortunately, no test was conducted to determine the viscoelastic properties of the concrete. For this reason, a default creep function was used to estimate the parameters of a concrete viscoelastic model. The selected creep function, based on the ACI 209R-92 model *(6)*, is shown in Equation 7.1.

$$D(t-t') = \frac{1}{E} \cdot \left(1 + \phi(t-t')\right) \quad \textbf{(7.1)}$$

where:
- $D(t-t')$ is the concrete creep function (strain divided by constant stress)
- E is the concrete elastic modulus (following ASTM C469)
- $\phi(t)$ is the creep coefficient: $\phi(t) = \frac{(t-t')^{\Psi}}{d+(t-t')^{\Psi}} \cdot \phi_u$
- t is time
- t' is the time when loading is applied
- ϕ_u is the ultimate creep coefficient: $\phi_u = 2.35$
- Ψ, d are model parameters; default values are: $\Psi = 0.6$ and $d = 10$ days

It is important to bear in mind that the creep coefficient of the ACI model is linked to an elastic modulus determined using the procedure in ASTM C469. A loading time of 0.01 days (around 15 minutes) can be assumed for that testing procedure *(7)*. Once the elastic modulus of the concrete is defined, the creep function can be built using the ACI 209R-92 default parameters in Equation 7.1. This approach was followed in this study.

The modeled shrinkage action was assumed to extend for four months (120 days), from construction of the slabs in February 2016 to June 2016. The concrete mixes hardened considerably during that period. For example, the elastic modulus of the P2 mix increased around 20% between the ages of one week and four months. Modeling

that hardening would require breaking those four months into smaller time intervals where the concrete elastic modulus could be assumed to be constant. To simplify the calculations for this research project, a unique age was chosen to determine the concrete elastic modulus. That age was two months, the middle of the time interval that was modeled.

The elastic modulus of the concrete was estimated based on the results of the laboratory testing conducted at OT, 4×OT, and 45 days. The lab results were fitted with a second-order polynomial function of the logarithm of time. The fitted function assumed a long-term versus 28-day ratio of 1.20 (the default value in the *MEPDG).* The estimated elastic modulus at an age of two months was 48,510 MPa (7.04 million psi) in the P2 mix and 43,950 MPa (6.37 million psi) in the P2-ICC mix. Once the elastic modulus was determined, the creep function was built for each of the mixes using Equation 7.1 with default parameters.

The creep function was used to determine the parameters of the longitudinal stiffness generalized Maxwell model, following the procedure outlined in Figure 7.7. Nine Maxwell elements were included in the generalized model. Shear and bulk stiffness parameters were determined based on the parameters of the longitudinal stiffness model, assuming the Poisson's ratio was 0.2 (constant, real number). As an example, Figure 7.8 shows a comparison between the creep function of the P2 mix (used to calibrate the viscoelastic model) and the result of an *Abaqus* simulation of a creep test (using the calibrated viscoelastic model).

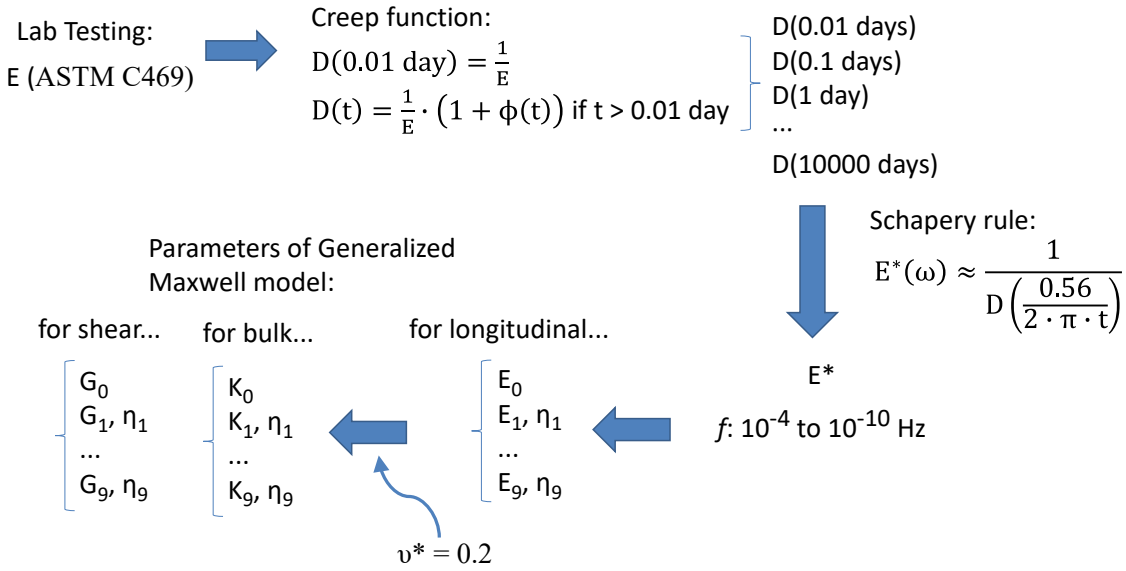

Figure 7.7: Approach for determining the parameters of the concrete viscoelastic model.

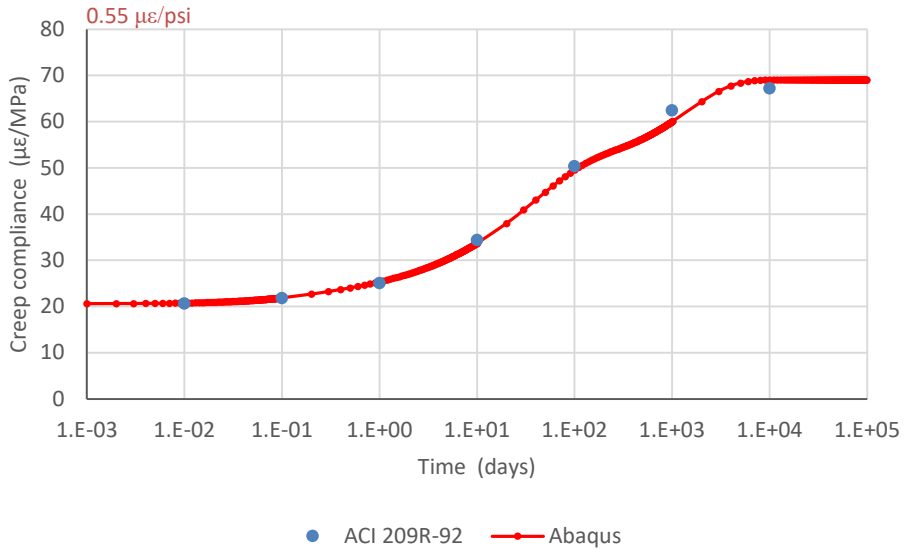

Figure 7.8: *Abaqus* software simulation of a longitudinal creep test (mix P2).

7.3 Finite Element Method Model

As described in Section 7.3, the FEM modeling was conducted with *Abaqus* software. Several modeling scenarios were considered for each of three sections (Section L, Section J, and Section K). In the first two scenarios, modeling was conducted following current standard practice for the ME design of concrete pavements. In that practice, the concrete and asphalt are regarded as linear elastic materials and asphalt stiffness is determined for a frequency that is representative of traffic loading. In this study, that frequency was set at 5 Hz. Then, additional modeling scenarios were considered to quantify the effect of the time-dependent behavior of asphalt and concrete. The following is a summary of all the modeling scenarios:

- Scenario 1: Concrete and asphalt are elastic with a Winkler type foundation (linear springs).
- Scenario 2: Concrete and asphalt are elastic, and foundation is tensionless springs.
- Scenario 3: Concrete is elastic, asphalt is viscoelastic, and foundation is tensionless springs.
- Scenario 4: Concrete and asphalt are viscoelastic, and foundation is tensionless springs.

Images showing the FEM modeling results of a 6×6 section and a 12×12 section are shown in Figure 7.9 and Figure 7.10, respectively. The following are details of the modeling:

- Analysis type: either Static (Scenarios 1 and 2) or Viscoelastic (Scenarios 3 and 4)
- Element type: 20-node quadratic brick with reduced integration (for concrete and asphalt)
- Number of slabs: six slabs (3×2) in 6×6 sections and three slabs (3×1) in 12×12 sections
- Slab thickness: 115 mm (4.5 in.)

- Asphalt thickness: 60 mm (2.4 in.) Old HMA in Section L; 120 mm (4.8 in.) (90 mm New HMA plus 30 mm RHMA-G) in Section J and Section K
- Foundation: either Winkler or tensionless foundation; in both cases, K = 0.15 N/mm³ (550 lb/in.³), based on FWD backcalculation
- Concrete stiffness: either elastic or viscoelastic; in the elastic calculations, E_{P2} = 48,510 MPa (7.04 million psi) and $E_{P2\text{-}ICC}$ = 43,950 MPa (6.37 million psi), based on ASTM C469
- Asphalt stiffness: either elastic or viscoelastic; in the elastic calculations, $E_{Old\ HMA} = E_{New\ HMA}$ = 6,575 MPa (0.95 million psi) and $E_{RHMA\text{-}G}$ = 3,100 MPa (0.45 million psi), corresponding to 25°C (77°F) and 5 Hz; in the viscoelastic calculations, asphalt temperature is assumed to be 25°C (77°)
- Bonding conditions: Concrete and asphalt are fully bonded

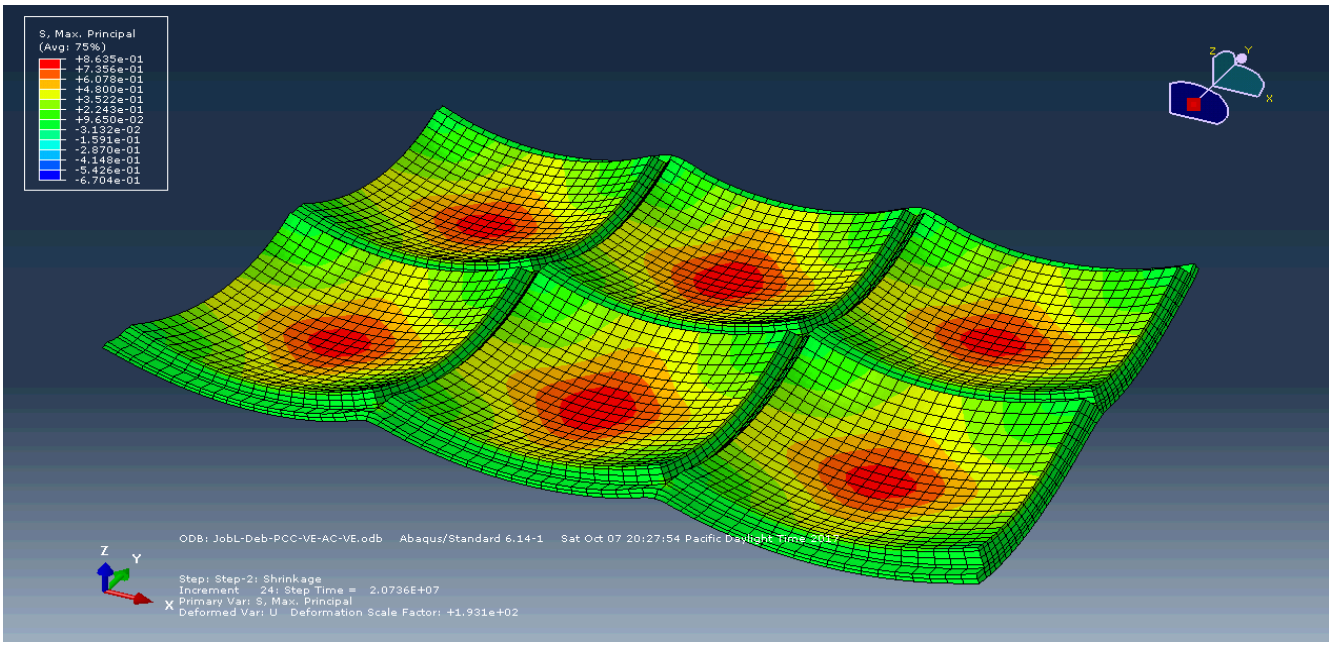

Figure 7.9: *Abaqus* modeling of 6×6 COA section for Scenario 1.

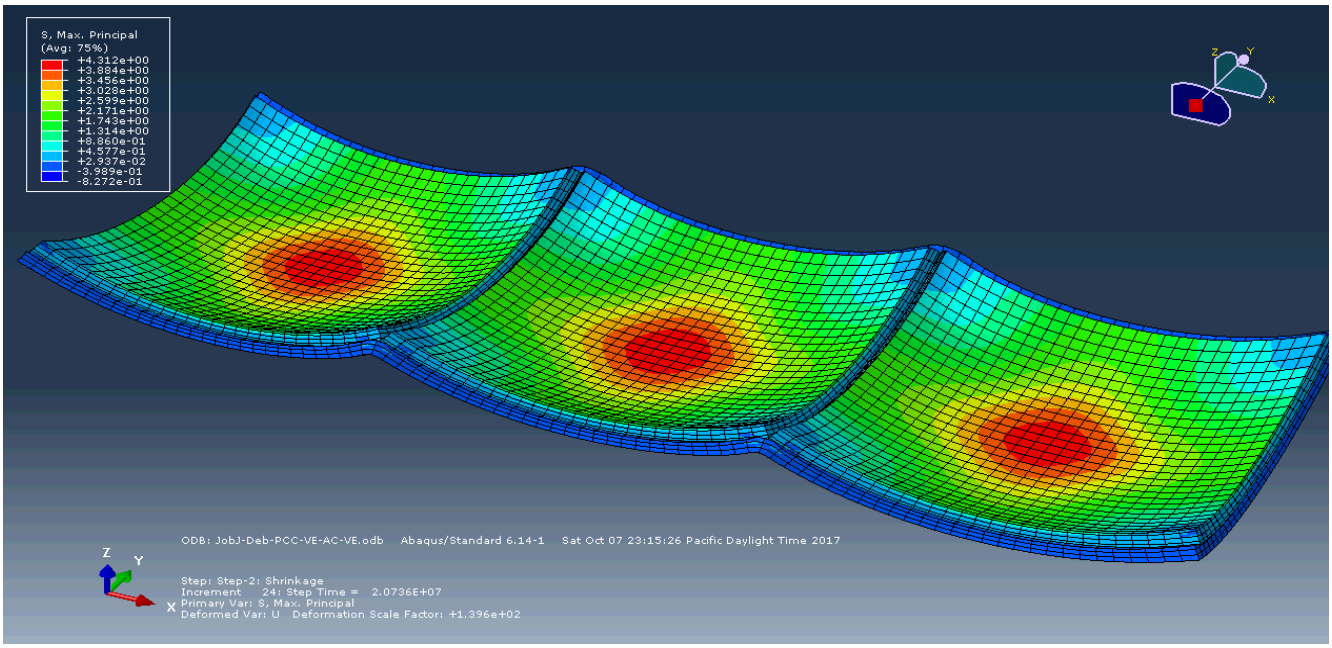

Figure 7.10: *Abaqus* modeling of 12×12 COA section for Scenario 1.

7.4 Modeling Results

The tensile stress calculated with *Abaqus* at the center of the slabs, at the top in the longitudinal direction, is shown in Figure 7.11, Figure 7.12, and Figure 7.13 for Section L, Section J, and Section K, respectively. In each of these figures, the results of the four modeling scenarios previously discussed are presented. The flexural strength of the corresponding mix is also shown in each of the figures. The strength values are based on laboratory testing conducted at OT, 4×OT, and 45 days. The lab results were fitted with a second-order polynomial function of the logarithm of time. The fitted function assumed a long-term versus 28-day ratio of 1.20 (the default value in the *MEPDG).*

The two first modeling scenarios that did not consider viscoelasticity in either the asphalt or the concrete, the same assumptions used in current concrete pavement ME design practice, resulted in very high tensile stresses at the top of the slabs of the three sections. Such high values would have resulted in concrete top-down cracking, which did not occur in either the 6×6 Section L or the 12×12 Section J, both of which include the P2 mix. It is evident that one or several stress-release mechanisms must exist. One such mechanism is the creep/relaxation of the asphalt, and another is the creep/relaxation of the concrete. In the third scenario, where viscoelastic creep/relaxation in the asphalt was considered, tensile stress was reduced by 45% in the 6×6 section and by 35% in the 12×12 sections (modeling Scenario 2 versus Scenario 3). When the creep/relaxation capacity of both the asphalt and the concrete was added in the fourth scenario, the tensile stresses were reduced by 55% in the 6×6 section and by 40% in the 12×12 sections (modeling Scenario 3 versus Scenario 4). The role that asphalt

creep/relaxation played was different from the role of concrete creep/relaxation. The former reduced the stresses created by the linear component of moisture-related shrinkage, while the later reduced the stresses created by the nonlinear component of the shrinkage.

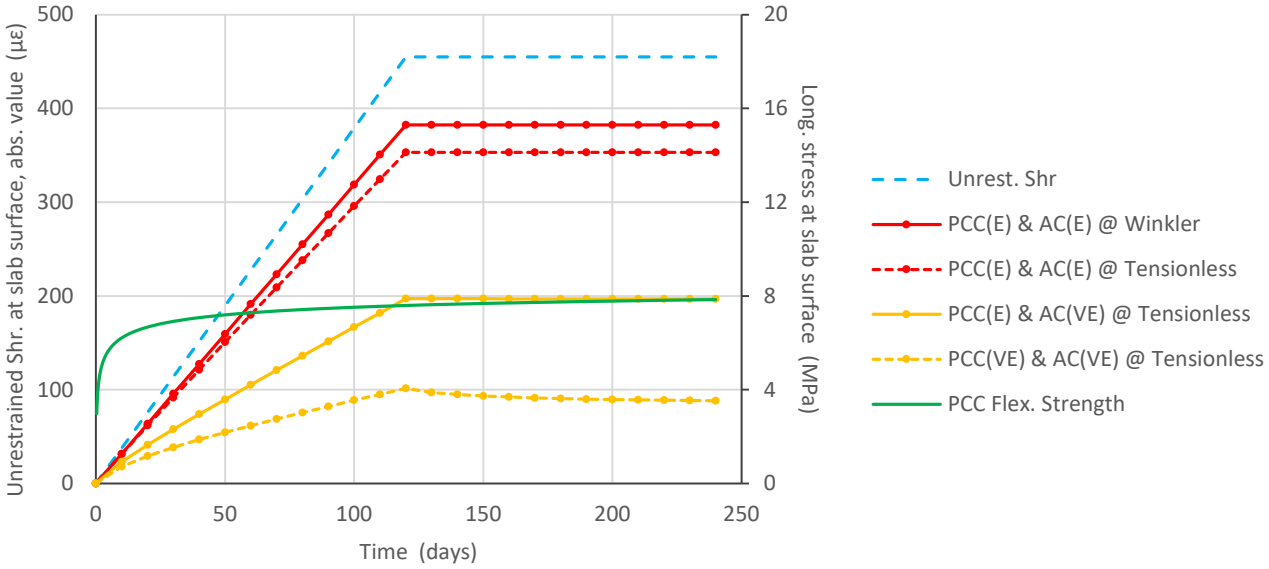

Figure 7.11: Results of *Abaqus* modeling of Section L (6×6, mix P2).

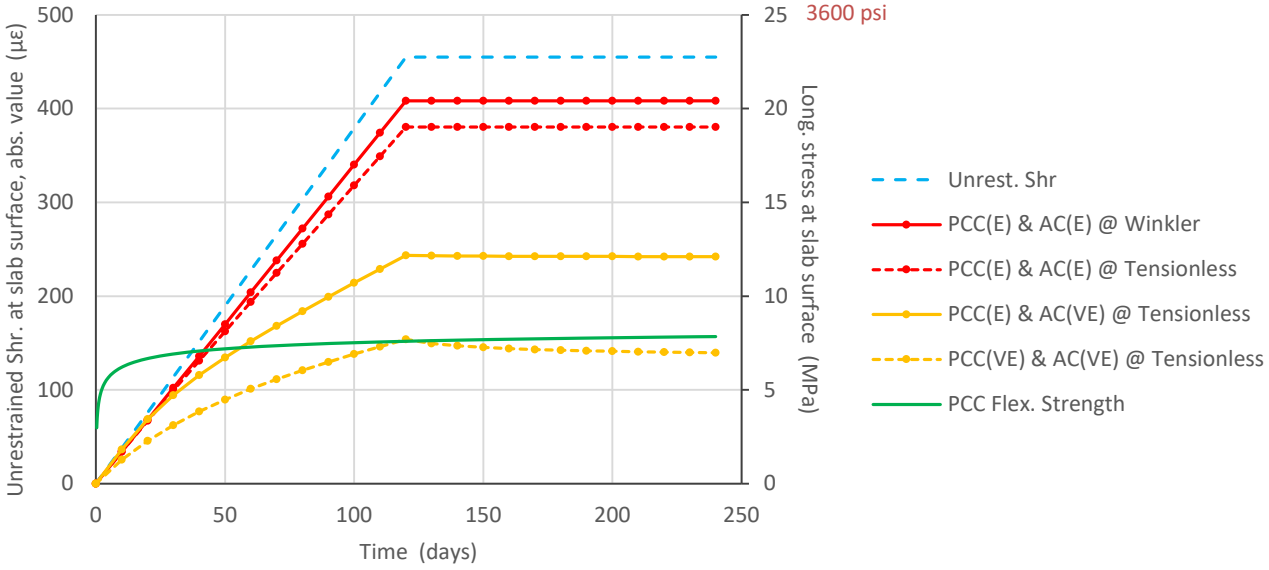

Figure 7.12: Results of *Abaqus* modeling of Section J (12×12, mix P2).

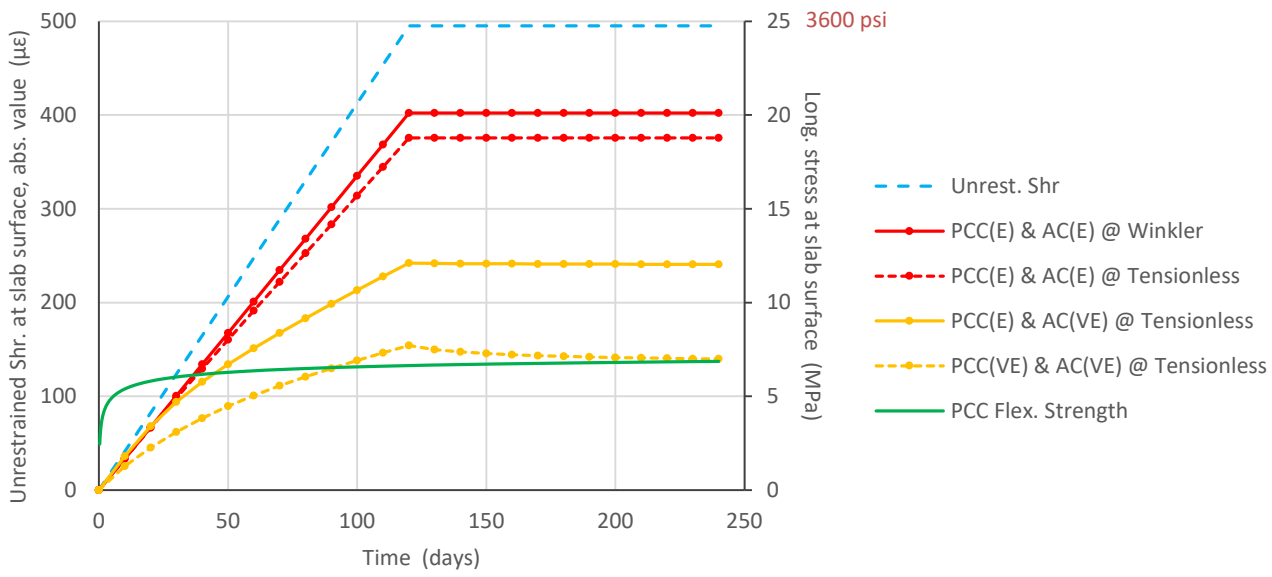

Figure 7.13: Results of *Abaqus* modeling of Section K (12×12, mix P2-ICC).

As shown in Figure 7.11 to Figure 7.13, the tensile stresses at the top of the slabs were lowered on the order of 40% because of the asphalt creep/relaxation capacity. This impact is easy to understand by observing the dynamic modulus master curves in Figure 7.5. Under traffic loading, with a frequency on the order of a few hertz, asphalt shear stiffness was on the order of 1,000 MPa (0.15 million psi). For a four-month loading period due to drying shrinkage contraction of the concrete, with a frequency on the order of 10^{-7} Hz, the shear stiffness of the asphalt mixes was on the order of 10 MPa (1,500 psi), a stiffness around 100 times smaller than under traffic loading and close to the stiffness of a soft soil.

The tensile stresses predicted in Section J (Figure 7.12) after the inclusion of concrete and asphalt viscoelasticity were still relatively high, since they reached the flexural strength of the mix after 120 days. It should be noted that thermal stresses are not included in the modeling results. If they had been included, the tensile stresses predicted in Section J would be greater than the flexural strength of the mix. Considering that no surface microcracking was observed in this section, it is likely that either other stress-release mechanisms exist or the effects of the asphalt and/or concrete creep/relaxation capacity have been underestimated. It is important to bear in mind that the creep coefficient prediction formulas of the ACI 209R-92 model are based on creep tests conducted in compression. It is likely that the concrete creep-relaxation capacity in tension is higher. Also, the role of drying creep has been ignored. An alternative hypothesis is that the visual examination of the Section J surface was not accurate enough to detect surface microcracking. Whether this last hypothesis is true or false, it is evident that visual examination is not the most precise option to detect surface microcracking and that other detection methods should be explored in the future.

Comparison of the modeling results in Figure 7.12 and Figure 7.13 indicates that surface microcracking was more likely to occur in Section K, with the P2-ICC mix, than in Section J, with the P2 mix. Furthermore, the results presented in the figures are based on the testing of mixes prepared in the laboratory. As explained in Section 6.5, the flexural strength was smaller in the P2-ICC field mix than in the same mix prepared in the laboratory (the hypothesis was that this field mix was produced with a relatively high water content). This fact, together with modeling results in Figure 7.13, agree with the generalized surface microcracking that was observed in this section.

It should be mentioned that Section K, despite its surface microcracking, did not show any discrete cracks or other signs of concrete damage. Further, the section supported HVS testing, where loads up to 80 kN (18 kip) on a single wheel were applied, without cracking.

An additional exercise was conducted to understand the role of surface microcracking as a stress-release mechanism. The drying shrinkage component of the vertical movement of the slab corners, measured with JDMDs, was plotted versus the differential drying shrinkage (slab bending, $\varepsilon_{DIFF,Sh,T0}$) in each of the sections (Figure 7.14). It was believed corner displacement in the section with surface microcracking (Section K) would be smaller for the same slab bending than in the sections where no surface microcracking was observed. The issue was that the JDMD sensors were only installed in the 6×6 sections (apart from Section K), so there was no other 12×12 section against which to compare the data from Section K. For this reason, the measured (backcalculated) data were compared with the *Abaqus* model predictions. The *Abaqus* predictions corresponding to modeling Scenario 4 (concrete and asphalt viscoelasticity included) are shown in Figure 7.14. In the 6×6 sections, the model's predictions were very close to the measured data. In these sections, the ratio between corner vertical displacement and slab bending was close to the maximum possible value—that is, the ratio that would exist if the slab were free to bend with no restriction from the asphalt base or its own weight. This outcome gives an idea of the creep capacity of the asphalt base. In Section K, the measured deflections were somewhat below the FEM model predictions. That difference corresponds with the presence of surface microcracking in this section, which is not accounted for in the FEM modeling. Nonetheless, the results are not conclusive since other explanations could explain that difference.

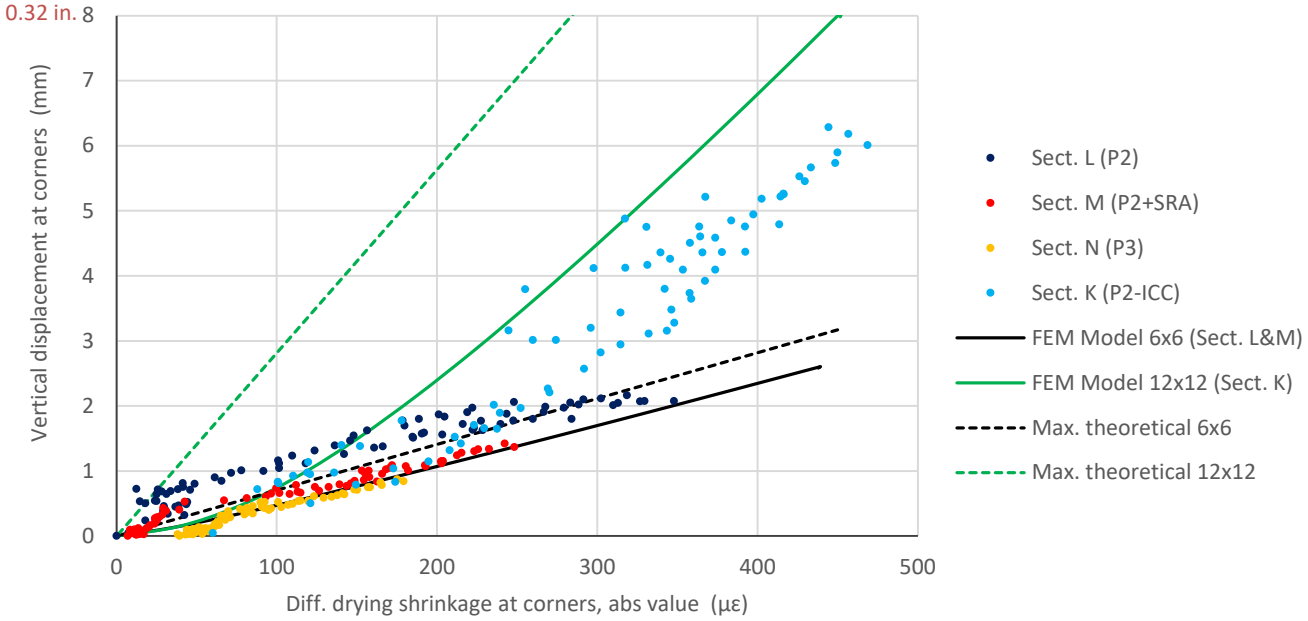

Notes: Each point in the graph corresponds to one day. The FEM model considers concrete and asphalt viscoelasticity and a tensionless subgrade (modeling Scenario 4). "Max. theoretical" represents the maximum possible corner vertical displacement, as if the slab was not subjected to any restriction (as if it was floating in outer space). Its determination is based on geometry rather than mechanics.

Figure 7.14: Comparison between the slab bending ($\varepsilon_{DIFF,Sh}$) and vertical displacement of slab corners.

8 SUMMARY, CONCLUSIONS, AND RECOMMENDATIONS

8.1 Summary

Fifteen COA sections were built at the UCPRC facility in Davis, California, on February 23 and 25, 2016. Six of the fifteen sections were instrumented with a total of 245 sensors to measure the response of the concrete slabs to environmental actions and cement hydration. The structural response of the slabs was measured with vibrating wire strain gauges (VWSGs) and joint displacement measuring devices (JDMDs). Concrete temperature, internal moisture, and internal relative humidity (RH) were measured as well. Based on the analysis of the data collected over 15 months and modeling with the finite element method (FEM), a series of conclusions were reached about how moisture-related shrinkage builds up in concrete pavements and the structural response of the COA slabs to the shrinkage action.

8.2 Conclusions

The conclusions are summarized in the following discussion, and they have been grouped to address the four main questions this research intended to answer.

8.2.1 What Moisture-Related Shrinkage Takes Place in the Concrete Overlay on Asphalt (COA) Slabs?

The data collected with the VWSGs were analyzed with incremental models that included two components, one that accounts for moisture-related shrinkage at constant temperature and another that accounts for thermal deformations. The parameters of the models were backcalculated by fitting measured strain with the model predictions. For the purposes of this study, the backcalculated parameters in the COA slabs were the daily values of the mean (average of the strains at the top and bottom of the slabs) and the differential (difference between the strains at the top and bottom of the slabs) moisture-related shrinkage.

The following are conclusions related to moisture-related shrinkage in the COA slabs:

- Very high levels of differential shrinkage were backcalculated in all sections with portland cement mixes treated with curing compound. Values were as high as 450 to 550 με, depending on the mix.
- Around 200 to 250 με of autogenous shrinkage was backcalculated in the mixes with Type II/V (P2) with a water/cement ratio of 0.33 and Type III (P3) portland cement with a water/cement ratio of 0.31. No autogenous shrinkage was measured in the internally cured mix (P2-ICC) or in the mix with CSA cement.
- The total moisture-related shrinkage values at the top of the COA slabs with portland cement mixes treated with curing compound reached as high as 600 to 750 με, depending on the mix.
- Rainfall events produced almost immediate decreases in the magnitude of the differential drying shrinkage in the COA slabs, except when the concrete was already saturated. The immediate response to rainfall occurred with both the portland cement and CSA mixes.

- The evolution of mean and differential shrinkage in the COA slabs showed that drying considerably affected the bottom half of the slabs during summer. This conclusion is supported by moisture content measurements near the middle of the slabs at a depth of 50 mm (2 in.) in the concrete. The slabs were 115 mm (4.5 in.) thick.

8.2.2 Do Shrinkage Prediction Models Work for Rapid-Strength Concrete (RSC) Mixes?

Shrinkage was measured in the laboratory following ASTM C157, at 50% constant air RH. Predictions made by the B3, B4, and ACI 209R-92 shrinkage models were compared with shrinkage data measured in the laboratory.

The following are conclusions related to use of the shrinkage prediction models for RSC mixes:

- The B3 and B4 models underestimated laboratory shrinkage considerably in the mixes with Type II/V (P2) and Type III (P3) portland cement.
- The B4 model did not improve on the predictions of the B3 model, even though the B4 model is more recent and is applicable to concrete mixes with admixtures, such as the P2 and P3 mixes. The B4 model predictions were particularly inaccurate in terms of autogenous shrinkage.
- Overall, the shrinkage predictions made by the ACI 209R-92 model were not far off from the shrinkage measured in the laboratory, even though this model was not developed for mixes with admixtures.
- None of B3, B4, and ACI 209R-92 shrinkage prediction models are applicable to mixes with CSA cement or to the internally cured mix (P2-ICC).

8.2.3 What Is the Relationship Between Laboratory and Field Shrinkage?

The parameters of the B4 model were backcalculated for each of the mixes based on lab shrinkage data (instead of using model equations). Then, a new prediction model was formulated based on (1) the B4 lab-calibrated model, (2) the *CalME* time-hardening incremental-recursive approach, and (3) a simplified procedure to account for shrinkage reversals due to relatively high air RH. The new model, referred to as "B4-IR" (B4 incremental-recursive), was used to predict shrinkage in the field.

The following are conclusions related to the relationship between laboratory and field shrinkage:

- The B4-IR model's predictions almost exactly reproduced the moisture-related shrinkage measured in a set of outdoors unrestrained shrinkage prisms with portland cement (P2, P3, and P2-ICC mixes).
- The B4-IR model's predictions almost exactly reproduced the differential shrinkage measured in the COA slabs with portland cement (P2, P3, and P2-ICC mixes). Although, in the case of this model, a slight modification of the B4 parameters was required.

- The B4-IR model failed to reproduce the shrinkage measured in the outdoors unrestrained shrinkage prisms made with CSA cement and in the COA slabs made with the same material.
- The good agreement between the B4-IR model's predictions and measured shrinkage—for the mixes with portland cement—indicates that a direct link between lab and field shrinkage can be established as soon as several factors are taken into account: (1) the age difference between the concrete in the lab and the concrete in the field when drying begins, (2) the shape and volume/surface ratio differences between the lab specimens and the field slabs, (3) the constant temperature and air RH in the lab versus the variable conditions in the field, and (4) the monotonic drying in the lab versus the alternating drying/wetting periods in the field, due to rainfalls and changing air RH.
- In B4-IR modeling, the unrestrained shrinkage profile in the slabs was assumed to be constant at the surface while the depth of shrinkage penetration was assumed to change as the slab concrete dried. The B4-IR model failed to reproduce the shrinkage measured in the COA slabs when the *MEPDG* unrestrained shrinkage profile assumption was followed (depth of drying is constant while the unrestrained shrinkage at slab top is the one that changes as slab concrete dries).
- Shrinkage reversals due to rainfall events were not modeled in this study. This topic should be investigated in the future since experimental data show shrinkage in the concrete slabs cannot be predicted based on air RH exclusively.

8.2.4 What Is the Stress Due to Moisture-Related Shrinkage?

The structural response of the COA slabs to the shrinkage action was modeled with *Abaqus* FEM software. Different modeling scenarios were considered. In two of these scenarios, the current standard practice for concrete pavement ME design was followed where the creep/relaxation capacity of concrete and asphalt are ignored. The rest of the modeling scenarios accounted for the creep/relaxation capacity of either asphalt or concrete and asphalt. The creep/relaxation capacity was accounted for by modeling the materials as linear viscoelastic using the generalized Maxwell model; model parameters were determined based on laboratory testing (asphalt) or ACI 209R-92 creep model (concrete).

The following are conclusions related to the stress due to moisture-related shrinkage:

- The FEM modeling following the standard ME design practice for concrete pavements assuming elastic properties for both the concrete and the asphalt base resulted in very high and unrealistic tensile stresses at the top of the slabs.

- Asphalt creep/relaxation reduced the concrete slabs stresses created by the linear component of moisture-related shrinkage. Because of this property of asphalt, the total tensile stresses at the top of the concrete slabs were reduced by 55% in the 6×6 sections and 40% in the 12×12 sections.
- Concrete creep/relaxation mainly reduced the stresses created at the top of the concrete slabs by the nonlinear component of the moisture-related shrinkage.
- The FEM model resulted in much smaller stresses at the top of the slabs when the model accounted for the creep/relaxation capacity of both the concrete and asphalt.
- In addition to the creep/relaxation capacity of concrete and asphalt, surface microcracking acted as a concrete stress-release mechanism in at least one the 12×12 sections, the one with the internally cured mix (P2-ICC). Surface microcracking was observed in this section approximately 15 months after construction. No discrete cracking was observed in the section, which also supported HVS testing, with loads up to 80 kN (18 kip) on a single wheel, without cracking.

8.3 Recommendations

The following are recommendations based on the findings and conclusions of this study:

- The use of short-sized slabs (6×6) rather than full-lane width slabs (12×12) contributes to reduced drying shrinkage stresses in COA, so their use is recommended in dry climates like California.
- The adoption of bases made of materials with creep capacity, including asphaltic materials, contributes to reduced drying shrinkage stresses in JPCP. Alternatively, similar benefits may be achieved with the use of an interlayer ("bond breaker") with creep capacity between the JPCP slabs and a rigid base. The interlayer is an alternative that requires further research.
- The drying shrinkage of portland cement concrete in the field was successfully predicted by using the model developed in this study, referred to as the B4 incremental-recursive model. Further research is recommended to extrapolate this model to different concrete materials and slab configurations.
- Modeling the structural response of concrete pavements under the drying shrinkage action requires consideration of tensile stress-release mechanisms in the concrete, including tensile creep and microcracking. This topic has received little attention in the past, so further research is recommended.

REFERENCES

1. American Association of State Highway and Transportation Officials. 2004. *Mechanistic-Empirical Pavement Design Guide* (National Cooperative Highway Research Program Project 1-37a). Washington, DC: American Association of State Highway and Transportation Officials.
2. Rao, S., and Roesler, J.R. 2004. *Analysis and Estimation of Effective Built-in Temperature Difference for North Tangent Slabs* (UCPRC-RR-2004-03). Davis and Berkeley, CA: University of California Pavement Research Center.
3. Ruiz, J.M., Garber, S., and Dick, J.C. 2015. *Computer-Based Guidelines for Concrete Pavements, HIPERPAV III®, Version 3.3 User's Manual* (Publication No. FHWA-HRT-14-087). Washington, DC: Federal Highway Administration.
4. Mateos, A., Harvey, J.T., Wu, R., Paniagua, F., and Paniagua, J. 2020. *Development of Improved Guidelines and Designs for Thin Whitetopping: Environmental Response of Full-Scale BCOA Sections* (Research Report: UCPRC-RR-2017-03) Davis and Berkeley, CA: University of California Pavement Research Center. escholarship.org/uc/item/5hx556j4.
5. Federation Internationale du Beton. *Structural Concrete: Textbook on Behaviour, Design and Performance. Updated Knowledge of the CEB/FIP Model Code 1990, Volume 2*. 1999. Lausanne, Switzerland: Federation Internationale du Beton.
6. American Concrete Institute. 1997. *Prediction of Creep, Shrinkage, and Temperature Effects in Concrete Structures* (ACI 209R-92). Farmington Hills, MI: American Concrete Institute.
7. Bazant, Z.P., and Baweja, L. 1995. "Creep and Shrinkage Prediction Model for Analysis and Design of Concrete Structures—Model B3." *Materials and Structures* 28: 357–365.
8. American Association of State Highway and Transportation Officials. 2015. *Mechanistic-Empirical Pavement Design Guide*, Second Edition. Washington, DC: American Association of State Highway and Transportation Officials.
9. Bazant, Z.P. 2015. "RILEM Draft Recommendation: TC-242-MDC Multi-Decade Creep and Shrinkage of Concrete: Material Model and Structural Analysis." *Materials and Structures* 48: 753–770.
10. Mateos, A., Harvey, T.J., Paniagua, F., Paniagua, J., and Wu, R. 2018. *Development of Improved Guidelines and Designs for Thin Whitetopping: Construction and Initial Environmental Response of Full-Scale BCOA Sections* (Research Report: UCPRC-RR-2017-02). Davis and Berkeley, CA: University of California Pavement Research Center. escholarship.org/uc/item/14t4f662.
11. Wu, R., and Harvey, J. 2012. "Calibration of Asphalt Concrete Cracking Models for California Mechanistic-Empirical Design (CalME)." In *7th RILEM International Conference on Cracking in Pavements:*

Mechanisms, Modeling, Testing, Detection and Prevention Case Histories, edited by Scarpas, A., Kringos, N., Al-Qadi, I., and Loizos, A., 537–547. Berlin, Germany: Springer Dordrecht.

12. Armaghani, J.M., Larsen, T.J., and Smith, L.L. 1987. "Temperature Response of Concrete Pavements." *Transportation Research Record* 1121: 23–33.
13. Chang, G., Rasmussen, R., Merritt, D., Garber, S., and Karamihas, S. 2010. *Impact of Temperature Curling and Moisture Warping on Jointed Concrete Pavement Performance* (Publication No. FHWA-HIF-10-010). Washington, DC: Federal Highway Administration.
14. Chang, G., Karamihas, S., Rasmussen, O., Merritt, D., and Swanlund, M. 2008. "Quantifying the Impact of Jointed Concrete Pavement Curling and Warping on Pavement Unevenness." Presented at 6th Symposium on Pavement Surface Characteristics: SURF 2008, Portoroz, Slovenia, October 20–23, 2008.
15. Karamihas, S.M., and Senn, K. 2012. *Curl and Warp Analysis of the LTPP SPS-2 Site in Arizona* (Publication No. FHWA-HRT-12-068). Washington, DC: Federal Highway Administration.
16. Lederle, R. Lothschutz, R.W., and Hiller, J.E. 2011. *Field Evaluation of Built-in Curling Levels in Rigid Pavements* (Final Report 2011-16). St. Paul, MN: Minnesota Department of Transportation.
17. Heath, A.C., and Roesler, J.R. 1999. *Shrinkage and Thermal Cracking of Fast-Setting Hydraulic Cement Concrete Pavements in Palmdale, California* (UCPRC-RR-1999-07). Davis and Berkeley, CA: University of California Pavement Research Center.
18. Hiller, J. E., and Roesler, J.R. 2005. "Determination of Critical Concrete Pavement Fatigue Damage Locations Using Influence Lines." *Journal of Transportation Engineering* 131, no. 8: 599–607.
19. Yu, H., Khazanovich, L., Darter, M., and Ardani, A. 1998. "Analysis of Concrete Pavement Responses to Temperature and Wheel Loads Measured from Instrumented Slabs." *Transportation Research Record* 1639, no. 1: 94–101.
20. Beckemeyer, C., Khazanovich, L., and Yu, H. 2002. "Determining Amount of Built-in Curling in Jointed Plain Concrete Pavement: Case Study of Pennsylvania I-80." *Transportation Research Record* 1809, no. 1: 85–92.
21. Yu, H., and Khazanovich, L. 2001. "Effects of Construction Curling on Concrete Pavement Behavior." In *Seventh International Conference on Concrete Pavements: The Use of Concrete in Developing Long-Lasting Pavement Solutions for the 21st Century, Volume 1*. Orlando, FL, September 9–13, 2001.
22. Wells, S., Phillips, B., and Vandenbossche, J. 2006. "Characterizing Strain Induced by Environmental Loads in Jointed Plain Concrete Pavements: Immediately After Paving and Throughout First 10 Months." *Transportation Research Record* 1947, no. 1: 36–48.
23. Jeong, J.H., and Zollinger, D. 2004. "Early-Age Curling and Warping Behavior: Insights from a Fully Instrumented Test-Slab System." Transportation Research Record 1896, no. 1: 66–74.

24. Rao, C., Barenberg, E.J., Snyder, M.B., and Schmidt, S. 2001. “Effects of Temperature and Moisture on the Response of Jointed Concrete Pavements.” In *Seventh International Conference on Concrete Pavements: The Use of Concrete in Developing Long-Lasting Pavement Solutions for the 21st Century, Volume 1*. Orlando, FL, September 9–13, 2001.
25. McCullough, B. F., and Rasmussen, R.O. 1999. *Fast-Track Paving: Concrete Temperature Control and Traffic Opening Criteria for Bonded Concrete Overlays, Volume 1, Final Report* (FHWA-RD-98-167). Washington, DC: Federal Highway Administration.
26. Bazant, Z.P., and Panula, L. 1978. “Practical Prediction of Time-Dependent Deformations of Concrete.” *Matériaux et Construction* 11, no. 5: 307–316.
27. Ruiz, J. M., Rasmussen, R.O., Chang, G.K., Dick, J.C., Nelson, P.K., and Ferragut, T.R. 2005. *Computer-Based Guidelines for Concrete Pavements, Volume I: Project Summary* (Publication No. FHWA-HRT-04-121). Washington DC: Federal Highway Administration.
28. Bazant, Z.P. 2015. “RILEM Draft Recommendation: TC-242-MDC Multi-Decade Creep and Shrinkage of Concrete: Material Model and Structural Analysis Model.” *Materials and Structures* 48, no. 4: 753–770.
29. Ruiz, J.M., Rasmussen, R.O., Chang, G.K., Dick, J.C., Nelson, P.K., Schindler, A.K., and Wilde, W.J. 2006. *Computer-Based Guidelines for Concrete Pavements, Volume III: Technical Appendices* (Publication No. FHWA-HRT-04-127). Washington, DC: Federal Highway Administration.
30. Jonasson, J. E., and Hedlund, H. 2000. “An Engineering Model for Creep and Shrinkage in High Performance Concrete.” In *International RILEM Workshop on Shrinkage of Concrete (Shrinkage 2000)*, edited by Baroghel-Bouny, V., and Aïtcin, P.C., 507–529. Paris: Réunion Internationale des Laboratoires et Experts des Matériaux.
31. Umehara, H., Uehara, T., Iisaka, T., and Sugiyama, A. 1995. “Effect of Creep in Concrete at Early Ages on Thermal Stress.” In *Thermal Cracking in Concrete at Early Ages: Proceedings of the International RILEM Symposium*, edited by Springenschmid. R., 79–86. London: Chapman & Hall..
32. Westman, G. 1999. “Concrete Creep and Thermal Stresses.” Doctoral thesis, Luleå University of Technology.
33. Jeong, J.H., Lim, J.S., Sun, R.J., and Zollinger, D.G. 2011. “Modelling of Differential Shrinkage of Pavement Slabs.” *ICE Proceedings—Transport* 165, no. 1: 3–14.
34. Kim, S.M., Won, M. , and McCullough, B. 1998. “Numerical Modeling of Continuously Reinforced Concrete Pavement Subjected to Environmental Loads.” *Transportation Research Record* 1629, no. 1: 76–89.
35. Weiss, W.J., Yang, W., and Shah, S.P. 1998. “Shrinkage Cracking of Restrained Concrete Slabs.” *Journal of Engineering Mechanics* 124, no. 7: 765–774.
36. Altoubat, S.A., and Lange, D.A. 2001. “Creep, Shrinkage, and Cracking of Restrained Concrete at Early Age.” *ACI Materials Journal* 98, no. 4: 323–331.

37. Lea, J.D., and Harvey. J. 2012. “The Simplified Thermal Modeling Approach Used in CalME.” Presented at Transportation Research Board Annual Meeting, Washington, DC, January 22–26, 2012.
38. California Department of Transportation, n.d. “Caltrans Pavement Climate Regions Map.” Climate. Accessed April 1, 2023. dot.ca.gov/programs/maintenance/pavement/concrete-pavement-and-pavement-foundations/climate.
39. Sun, R.J., Ge, Z., Li, W., Zhou, H.F., and Huang, D.W. 2013. “Experimental Research of the Rapid Set Cement Concrete for Rapid Repair of Concrete Pavements.” *Advanced Materials Research* 634-638: 2697–2701).
40. Mateos, A., Harvey, T.J., Wu, R., Paniagua, F., and Paniagua, J. Forthcoming. *Development of Improved Guidelines and Designs for Thin Whitetopping: HVS Testing of Full-Scale BCOA Sections* (UCPRC-RR-2017-06). Davis and Berkeley, CA: University of California Pavement Research Center.
41. Mateos, A. 2003. “Modeling the Structural Response of Flexible Pavements from Full Scale Test Track Experimental Data.” PhD Thesis, Technical University of Madrid (publication in Spanish).